IFFT-Based Techniques for Peak Power Reduction in OFDM Communication Systems

by

Abolfazl Ghassemi
B.Sc., University of Tehran, 1993
M.A.Sc., University of Victoria , 2003

A Dissertation Submitted in Partial Fulfillment of the Requirements
for the Degree of

DOCTOR OF PHILOSOPHY

in the Department of Electrical and Computer Engineering

© Abolfazl Ghassemi, 2008

University of Victoria

All rights reserved. This dissertation may not be reproduced in whole or in part by photocopy or other means, without the permission of the author.

IFFT-Based Techniques for Peak Power Reduction in OFDM Communication Systems

by

Abolfazl Ghassemi

Ph.D, University of Victoria, 2008

Supervisory Committee

Dr. T. A. Gulliver, Supervisor (Dept. of Electrical and Computer Engineering)

Dr. K. F. Li, Department Member (Dept. of Electrical and Computer Engineering)

Dr. M. Sima, Department Member (Dept. of Electrical and Computer Engineering)

Dr. A. Rowe, Outside Member (Dept. of Mechanical Engineering)

Supervisory Committee

Dr. T. A. Gulliver, Supervisor (Dept. of Electrical and Computer Engineering)
Dr. K. F. Li , Department Member (Dept. of Electrical and Computer Engineering)
Dr. M. Sima, Department Member (Dept. of Electrical and Computer Engineering)
Dr. A. Rowe, Outside Member (Dept. of Mechanical Engineering)

ABSTRACT

Orthogonal frequency division multiplexing (OFDM) is a multicarrier transmission technique which provides efficient bandwidth utilization and robustness against time dispersive channels. A major problem in the RF portion of a multicarrier transmitter is Gaussian-like time-domain signals with relatively high peak-to-average power ratios (PAPRs). These peaks can lead to saturation in the power amplifier (PA) which in turn distorts the signal and reduces the PA efficiency. To address this problem, numerous techniques have appeared in the literature based on signal and/or data modification.

In the class of distortionless techniques, partial transmit sequences (PTS), selective mapping (SLM), and tone reservation (TR) have received a great deal of attention as they are proven techniques that achieve significant PAPR reduction. However, high computational complexity is a problem in practical systems. In PTS and SLM, this complexity arises from the computation of multiple inverse fast Fourier transforms (IFFTs), resulting in a complexity proportional to the number of PTS subblocks or SLM sequences. TR has also a high computational complexity related to the computation of the IFFT as it must search for the optimal subsets of reserved subcarriers and generate the peak reduction signal. In addition, most research in the direction of analyzing and improving the above techniques has employed direct computation of the inverse discrete Fourier transform (IDFT), which is not practical for implementation.

This thesis focuses on the development and performance analysis of the major distortionless techniques in conjunction with the common IFFT algorithms to reduce the peak-to-power average (PAPR) of the original OFDM signal at the transmitter side. The structure of the IFFT common algorithms is used to propose a class of IFFT-based PAPR reduction techniques to reduce the computational complexity and improve PAPR performance.

For IFFT-based PTS , two techniques are proposed. A low complexity scheme based on decimation in frequency (DIF) and high radix IFFT algorithm is proposed. Then, a new PTS subblocking technique is proposed to improve PAPR performance. The periodic auto-correlation function (ACF) of time-domain IFFT-based PTS subblocks is derived. To improve the PAPR, we use error-correcting codes (ECCs) in the subblocking. Our approach significantly decreases the computational complexity while providing comparable PAPR reduction to ordinary PTS (O-PTS).

With IFFT-based SLM, a technique for reducing computational complexity is proposed. This technique is based on multiplying the phase sequences with a subset of the inputs to identical inverse discrete Fourier transform (IDFTs). These subsets generate the partial SLM sequences using repetition codes. It is also shown how the partial time-domain subsets can be combined to generate new SLM sequences. These sequences do not requires any IFFT operations. The proposed scheme outperforms the existing techniques while providing comparable PAPR reduction to original SLM (O-SLM).

Finally, a gradient-based algorithm is proposed for IFFT-based TR. Unlike previous work, non-static channels are considered where the peak reduction tones (PRTs) locations and consequently the peak reduction kernels should be adjusted dynamically for best performance. Two low complexity algorithms with different degrees of computational complexity and PAPR performance are proposed. To generate the peak reduction kernels, the transform matrices of identical IFFTs are used. This provides low complexity solutions to determining the PRTs and computing the peak reduction kernels.

Table of Contents

Supervisory Committee ii

Abstract iii

Table of Contents v

List of Tables viii

List of Figures x

List of Abbreviations xv

Acknowledgement xxi

Dedication xxii

1 Introduction 1

1.1 PAPR Reduction Schemes 2

1.2 Contributions and Organization of the Thesis 4

2 OFDM Overview 7

2.1 Historical Notes on OFDM Systems 7

2.2 The Fundamentals of OFDM Systems 8

2.2.1 Filter-bank OFDM 10

2.2.2 OFDM with IFFT/FFT implementation 11

2.2.3 OFDM system model 13

2.3 OFDM Major Drawbacks 16
2.3.1 Peak power and its effects 16
2.3.2 Peak-to-average power ratio (PAPR) 22

3 Techniques for PAPR Reduction **25**
3.1 Distortion PAPR Techniques 26
3.1.1 Clipping 26
3.1.2 Companding 28
3.2 Distortionless PAPR Techniques 28
3.2.1 Coding 30
3.2.2 Tone injection 31
3.2.3 Partial transmit sequence (PTS) 32
3.2.4 Selective mapping (SLM) 37
3.2.5 Tone reservation 38
3.2.5.1 QCQP method for passband transmission 41
3.2.5.2 LP-based technique for real-baseband transmission . . . 42
3.2.5.3 The suboptimal iterative algorithms 43

4 Fast Fourier Transforms: Theory and Algorithms **49**
4.1 The Fast Fourier Transform (FFT) 50
4.2 The Common FFT Algorithms 52
4.2.1 Radix-r FFT algorithms 55
4.2.1.1 Radix-r DIT and DIF algorithms 56
4.2.1.2 General FFT terms 58
4.2.1.3 High radix FFT algorithms 58
4.2.2 Other FFT algorithms 60
4.2.3 Radix-r FFT algorithms based on stages 61
4.2.3.1 The identical DFTs 61
4.2.4 Radix-r FFT computational complexity 68

5 IFFT-Based PAPR Reduction Techniques **70**

5.1 PTS and the Common FFT Algorithms 70

5.1.1 IFFT-based PTS 72

5.1.1.1 Computational complexity 75

5.1.1.2 DIF versus DIT algorithms 75

5.1.1.3 High radix versus low radix algorithms 78

5.1.1.4 Auto-correlation of the IFFT-based PTS subblocks . . . 82

5.1.1.5 Error-correcting code subblocking 83

5.2 SLM and the Common FFT Algorithms 100

5.2.1 IFFT-based SLM 101

5.2.1.1 DIF-SLM versus DIT-SLM 102

5.2.1.2 Varying r 102

5.2.1.3 Partial selective mapping 102

5.3 TR and the Common FFT Algorithms 111

5.3.1 IFFT-based TR 112

5.3.1.1 The efficient suboptimal approach 116

6 Conclusion **128**

6.1 Summary 128

6.2 Future work 130

Bibliography **133**

Appendix A The normalized periodic autocorrelation of IFFT-based PTS subblocks **141**

List of Tables

Table 5.1 Multiplicative complexity for the radix-2 DIF and DIT FFTs with $N = 256, 2048, 8192$ and $2 \leq m - v \leq 6$. 76

Table 5.2 Multiplicative complexity reduction for DIF-PTS over DIT-PTS and O-PTS, with $P = 8$, $N = 256, 2048, 8192$, and $2 \leq m - v \leq 6$. 78

Table 5.3 Multiplicative complexity reduction for radix-4 over radix-2 DIF-PTS with $N = 256, 2048$, $P = 8$ and similar CCDF. 81

Table 5.4 The number of subblocks for various numbers of repeated twiddle factors and FFT sizes with $r = 2, 4$ and $m - v = 2, 3$. 90

Table 5.5 Comparison of PTS-ECC, O-PTS [27] and PTS-MS in terms of PAPR improvement for $256 \leq N \leq 2048$, CCDF=10^{-4}, and $m - v = 2, 3$. 94

Table 5.6 Multiplicative and additive complexity reduction for P-SLM over DIF-SLM ($\nu = 2^0$) and O-SLM [27] with $N = 2048$, $\Omega = 8$, and $\nu = 2^1$ . . 109

Table 5.7 Normal and digit-reversed inputs and outputs for a 32-point IFFT with 8-point identical IDFTs at stage $v = 3$. 115

Table 5.8 The number of iterations $\bar{I}_{DPRT}$ for the DPRT algorithm and $\bar{I}_T$ for algorithm in [42] as a function of the cumulative distribution function of the absolute value of the second peak CDF(γ). 121

Table 5.9 Computational complexity comparison between DPRT and algorithm in [42] for computing peak reduction kernels. 121

Table 5.10 The number of iterations $\bar{I}_{SPRT}$ for the DPRT algorithm and $\bar{I}_T$ for algorithm in [42] as a function of the cumulative distribution function of the absolute value of the second peak CDF(γ). 123

Table 5.11 Computational complexity comparison between DPRT and algorithm in [42] for computing peak reduction kernels. 123

List of Figures

Figure 2.1 Amplitude spectrum of an OFDM symbol. 9
Figure 2.2 Filter bank OFDM transceiver. 10
Figure 2.3 Amplitude spectrum of an IDFT output with sampling factor $J = 1$. 13
Figure 2.4 Amplitude spectrum of an IDFT output with sampling factor $J > 1$. 14
Figure 2.5 The OFDM system model. 14
Figure 2.6 Time representation of an OFDM symbol with CP. 15
Figure 2.7 A typical power amplifier (PA) transfer function. 17
Figure 2.8 Time representation of an OFDM symbol with 4 subcarriers. 18
Figure 2.9 Effect of clipping noise on the received OFDM signal for 1000 OFDM symbols with a 16-QAM constellation, N=256, IBO=5 dB. 19
Figure 2.10 Power spectral density of an OFDM signal for different IBO values where $N = 256$, $J = 4$, $G = 1$, $A = 1$, and $\epsilon = 10$. 21
Figure 2.11 CCDF of PAPR for different oversampling factors J with $N = 256$ and 16QAM subcarrier modulation. 23
Figure 2.12 Theoretical and numerical CCDF of the PAPR for different values of N with $J = 4$. 24

Figure 3.1 Symbol error rate of clipped OFDM symbols for $N = 256$ and QPSK constellation mapping. The unclipped signal, $A_0 = \infty$, is shown along with clipping levels $A_0 = 6, 8$ dB. 27
Figure 3.2 Waveforms for an OFDM signal and the same signal companded for $N = 64$, $J = 4$. (a) original signal. (b) μ-law companded signal with $\mu = 255$. 29

Figure 3.3 Block diagram for the tone injection PAPR reduction technique. . . 31
Figure 3.4 Example of mapping a 4-QAM symbol into a 32-QAM symbol in the tone injection method. 33
Figure 3.5 Block diagram for the partial transmit sequence PAPR reduction technique. 33
Figure 3.6 Example of subblock partitioning for PAPR reduction in an OFDM system with $N = 16$ subcarriers and $P = 4$: (a) adjacent (b) equally spaced (c) random. 35
Figure 3.7 CCDF of the OFDM signal for various P and W with $N = 256$ and pseudo random subblocking. 36
Figure 3.8 Block diagram for the selective mapping PAPR reduction technique. 37
Figure 3.9 PAPR CCDF of SLM for various Ω with $N = 256$ and $J = 4$. 39
Figure 3.10 Block diagram for the tone reservation PAPR reduction technique. . 40
Figure 3.11 Tone reservation performance comparison using the algorithm in [42] with randomly and consecutively selected Λ, $N = 512$, and $L/N = 6.3\%, 12.5\%$ for a passband multicarrier system. 44
Figure 3.12 PAPR performance using the using a gradient-based algorithm in [42] with randomly chosen subcarriers, $L/N = 6.3\%$, $\beta = 40$, $A = 6dB$, and $\bar{I} = 10$. 48

Figure 4.1 Signal flow graph of a 16-point FFT using $N/2$-point DFTs. 53
Figure 4.2 Radix-2 DIT FFT butterfly diagram. 54
Figure 4.3 Signal flow graph of a 16-point FFT using radix-2 DIF algorithm. . . 57
Figure 4.4 Radix-2 DIF FFT butterfly diagram. 57
Figure 4.5 Signal flow graph of a 16-point FFT using a radix-4 DIF algorithm. . 59
Figure 4.6 Recursive reduction of $\frac{N}{r^{v-1}}$-point DFTs with DIF radix-r at stage v. 63
Figure 4.7 Recursive reduction of $\frac{N}{r^{m-v}}$-point DFTs with DIT radix-r at stage v. 65

Figure 5.1 Block diagram of FFT/IFFT computation. 73

Figure 5.2 Number of nontrivial multiplications versus the number of remaining stages $m - v$ for DIF radix-2 compared with DIT radix-2 and $N = 256, 2048, 8192$. 77

Figure 5.3 CCDF of DIF-PTS compared with DIT-PTS for $r = 2$ at stage $m - v = 5$ and O-PTS with $N = 256, 2048$. 79

Figure 5.4 CCDF of DIF-PTS radix-2 compared with DIF-PTS radix-4 for various numbers of remaining stages $m - v$ with $N = 256$. 80

Figure 5.5 CCDF of DIF-PTS radix-2 compared with DIF-PTS mixed-radix for various numbers of remaining stages $m - v$ with $N = 2048$. 81

Figure 5.6 The auto-correlation of PTS sequences in a PTS radix FFT for $N = 32$, $v = 3$, $P = 4$ and $r = 2$ with repeated subcarriers within each subblock. 84

Figure 5.7 The auto-correlation of PTS sequences in an IFFT-based PTS for $N = 32$, $v = 3$, $P = 4$, $r = 2$, $b = 0$, M-sequence and ECC subblocks, p_0 and p_1. 87

Figure 5.8 The auto-correlation of PTS sequences in an IFFT-based PTS FFT for $N = 32$, $v = 3$, $P = 4$, $r = 2$, $b = 0$, M-sequence and ECC subblocks, p_2 and p_3. 88

Figure 5.9 The auto-correlation of PTS sequences in an IFFT-based PTS for $N = 32$, $v = 4$, $P = 4$, $r = 2$, $b = 1$, and ECC subblocks, p_0, p_1, p_2, and p_3. 91

Figure 5.10 CCDF of PTS-ECC in comparison with PTS-MS and O-PTS with $m - v = 2$ and $m - v = 3$ for N=256. 95

Figure 5.11 CCDF of PTS-ECC in comparison with PTS-MS and O-PTS, with $m - v = 2$ and $m - v = 3$ for N=512. 96

Figure 5.12 CCDF of PTS-ECC in comparison with PTS-MS and O-PTS, with $m - v = 2$ and $m - v = 3$ for N=1024. 97

Figure 5.13 CCDF of PTS-ECC in comparison with PTS-MS and O-PTS, with $m - v = 2$ and $m - v = 3$ for N=2048. 98

Figure 5.14 BER versus E_b/N_0 for OFDM systems using O-PTS and PTS-RC with $m - v = 3$, $N = 256$, and $P = 16$ in the presence of an HPA nonlinearity with OBO = 5 dB. 99

Figure 5.15 CCDF of DIF-SLM radix-2 compared with DIT-SLM radix-2 at stage $m - v = 5$ and O-SLM with $N = 2048$ and $\Omega = 8$. 103

Figure 5.16 CCDF of DIF-SLM radix-2 compared with DIF-SLM mixed-radix for various numbers of remaining stages $m - v = 5$ with $N = 2048$ and $\Omega = 8$. 104

Figure 5.17 CCDF of P-SLM compared with DIF-SLM ($\nu = 2^0$) and O-SLM for various numbers of remaining stages $m - v$, partial number of DFTs, ν, and 8 SLM sequences ($\Omega = 8$) with $r = 2$ and $N = 2048$. 110

Figure 5.18 32-point DFT with reserved tone vector C corresponding to intermediate signals $\widehat{C}$ at stage $v = 3$. 114

Figure 5.19 Cumulative distribution function of the absolute value of the second peak versus the number of iterations $\bar{I}$ using the DPRT algorithm for $L = 32$ and $8 \leq r^{v-1} \leq 32$ in comparison with Tellado's algorithm [42]. 120

Figure 5.20 Cumulative distribution function of the absolute value of the second peak versus the number of iterations $\bar{I}$ using the SPRT algorithm for $L = 32$ and $8 \leq r^{v-1} \leq 32$ in comparison with Tellado's algorithm [42]. 124

Figure 5.21 PAPR Performance comparison of DPRT and Tellado's algorithm [42] for various of γ values, with $A = 6$ dB, $L = 32$, $\beta = 40$, and $r^{v-1} = 8$. 126

Figure 5.22 PAPR Performance comparison of SPRT and Tellado's algorithm [42] for various of γ values, with $A = 6$ dB, $L = 32$, $\beta = 40$, and $r^{v-1} = 8$. 127

List of Abbreviations

ACF	auto-correlation function
ADSL	asymmetric digital subscriber line
AWGN	additive white Gaussian noise
ASIC	application specific integrated circuits
BER	bit error rate
BWA	broadband wireless access
CDF	cumulative distribution function
CCDF	complementary cumulative distribution function
DAB	digital audio broadcasting
DAC	digital to analog converter
DFT	discrete Fourier transform
DIF	decimation in frequency
DIT	decimation in time
DSP	digital signal processing
DPRT	different random peak reduction tones
DVB	digital video broadcasting
ECC	Error-correcting code
FDM	frequency division multiplexing
FFT	fast Fourier transform
FPGA	field programmable gate array
HDSL	high-bit-rate digital subscriber lines
HDTV	digital television and high-definition television
HF	high frequency
IFFT	inverse fast Fourier transform
LP	linear programming
IBI	inter block interference

IBO	input back-off
ICI	intercarrier interference
IDFT	inverse discrete Fourier transform
OBO	output back-off
OFDM	orthogonal frequency-division multiplexing
QAM	quadrature-amplitude modulation
QCQP	quadratically constrained quadratic program
QPSK	quadrature phase-shift keying
MIMO	multiple-input multiple-output
MMDS	multicarrier multipoint distribution service
MS	M-sequence
MSE	mean square error
SLM	selective mapping
SNDR	signal-to-noise-and-distortion-ratio
SNR	signal-to-noise ratio
SSPA	solid state power amplifier
SPRT	same random peak reduction tones
PA	power amplifier
PAPR	peak-to-average power ratio
PICR	peak interference-to-carrier ratio
PRT	peak reduction tones
PTS	partial transmit sequence
RC	repetition codes
TI	tone injection
TR	tone reservation
VHDSL	very high-speed digital subscriber line

Symbols

A	predefined threshold for peak power of soft limiter
A_0	threshold level for clipping
A'	Normalized constant for companding function
B	computational complexity
b	number of repeated subcarriers
C	frequency-domain peak reduction scalar
$\mathbf{C}$	frequency-domain peak reduction vector
c	time-domain peak reduction scalar
$\mathbf{c}$	time-domain peak reduction vector
$\widehat{C}$	reserved subcarriers for passband signal
$\bar{C}$	reserved subcarriers for baseband signal
C'	frequency-domain extended signal
c'	time-domain extended signal
E	frequency-domain peak reduction kernel
e	time-domain peak reduction kernel
$\mathbf{e}$	vector of peak reduction kernels
f	frequency
F_p	periodic auto-correlation function
g	amplifier distortion function
G	amplifier small gain
H	channel frequency response
h	channel impulse response
I	all ones matrix
$\bar{I}$	number of randomly chosen peak reduction tones
J	oversampling rate
k	OFDM subcarrier index
$\widetilde{k}$	output index for identical DIF algorithm
$\widehat{k}$	output index for identical DIT algorithm

L number of reserved tones

$\bar{M}$ active numbers of subcarriers

m number of FFT stage

N FFT point

n OFDM symbol index

$\widetilde{n}$ input index for identical DIF FFT

$\widehat{n}$ input index for identical DIT FFT

P number of PTS subblocks

Q IDFT matrix

$\check{Q}$ DFT matrix

q row vector of DFT matrix

$\mathbf{s}$ vector of elements over ring

$\widehat{\mathbf{s}}$ matrix of elements over ring

r radix

R reduction ratio

$\mathcal{R}$ subblock matrix

T_N twiddle factor

U frequency-domain SLM sequence

$\mathbf{U}$ frequency-domain SLM vector

u time-domain SLM sequence

$\mathbf{u}$ time-domain SLM vector

$\bar{U}$ frequency-domain partial SLM sequence

$\bar{u}$ time-domain partial SLM sequence

$\hat{u}$ time-domain combined SLM sequence

v FFT stage

W size of PTS phase vector

X frequency-domain scalar

$\mathbf{X}$ frequency-domain vector

$\widetilde{X}$ frequency-domain intermediate scalar for DIF algorithm

$\widetilde{\mathbf{X}}$ frequency-domain intermediate vector for DIF algorithm

$\widehat{X}$	frequency-domain intermediate scalar for DIT algorithm
$\widehat{\mathbf{X}}$	frequency-domain intermediate vector for DIT algorithm
$\widetilde{x}$	time-domain intermediate scalar for DIF algorithm
$\widetilde{\mathbf{x}}$	time-domain intermediate vector for DIF algorithm
$\widehat{x}$	time-domain intermediate scalar for DIT algorithm
$\widehat{\mathbf{x}}$	time-domain intermediate vector for DIT algorithm
$\bar{x}$	peak reduced scaler by gradient algorithm
$\bar{\mathbf{x}}$	peak reduced vector by gradient algorithm
$\breve{x}$	peak reduced scalar by controlled clipper algorithm
$\breve{\mathbf{x}}$	peak reduced vector by controlled clipper algorithm
$\check{x}$	amplified signal
X'	frequency-domain PTS sequences
x'	time-domain PTS sequences
y	intermediate scalar of corresponding FFT
$\mathbf{y}$	intermediate vector of corresponding FFT
$\mathbf{z}$	received signal vector
$\mathbf{Z}$	detected signal vector
α	number of identical DIT DFTs
β	the number of iterations for suboptimal algorithms
χ	controlled clipper pulse
Δ	impulse function
δ	PAPR threshold
ϵ	power amplifier control factor
ϕ_ω	SLM phase factor
Γ	second peak
γ	second peak threshold
η	number of identical DIF DFTs
λ	peak reduction location
Λ	vector of peak reduction locations
ν	number of subsets for partial SLM

θ_p PTS phase factor

ϑ commpanding function

ψ element of pseudo-random sequence

Ψ pseudo-random sequence

σ^2 variance

Ω number of SLM sequences

ξ auto-correlation lag

Acknowledgement

First and foremost I wish to express my sincere gratitude to my supervisor, Professor T. A. Gulliver and thank for his excellent academic advice and support during the course of this research. Discussion and collaboration with him have always been inspiring and fruitful.

I would like to thank Prof. K. F. Li, Prof. M. Sima, Prof. A. Row, for serving on my supervising committee, persuing my thesis manuscript, and giving their insightful advice. I would also like to thank all the present and past members of the Telecommunications Research Group who have provided a pleasant working environment.

Lastly, my deepest thanks go to family. My parents, Sorror Alibabae and Ghanbar Ghassemi, who have supported me by their unwavering love and encouragement. My wife, Nasrin Hatami, has offered me her immense love, understanding, help and has greatly contributed to my happiness throughout our many years. My daughter, Nika Fatima Ghassemi, has been a constant source of inspiration and motivation in the final years of this research.

Dedication

Dedicated to the greatest Parents, who taught me the Value of Study and Perseverance Ethic

To my Wife, Nasrin; and my Daughter, Nika for the Support of Spirit and the Patient.

Chapter 1

Introduction

Multicarrier modulation is a data transmission technique which provides efficient bandwidth utilization and robustness against time dispersive channels. Examples of multicarrier modulation systems are digital audio broadcasting (DAB), digital video broadcasting (DVB), and wireless local and metropolitan area networks using orthogonal frequency-division multiplexing (OFDM), and digital subscriber lines (DSLs) using discrete multitone (DMT) systems.

OFDM is an effective multicarrier transmission technique for wireless communications over frequency-selective channels. It provides immunity to multipath fading and uses a fast Fourier transform (FFT) for the baseband modulation and demodulation. An FFT simplifies the design of the transceiver and eliminates the need for high speed equalizers, resulting in an efficient hardware implementation. However, the time-domain OFDM signal can exhibit a large peak-to-average power ratio (PAPR). This reduces the efficiency of the power amplifier as it causes nonlinear distortion which introduces spectral spreading, intermodulation, and changes in the signal constellation. One solution to this problem is to employ an expensive power amplifier with a large linear range. Other techniques are based on signal/data modification.

1.1 PAPR Reduction Schemes

Numerous techniques have appeared in the literature to reduce the PAPR [1]-[56]. They can largely be classified as distortion or distortionless techniques. Distortion techniques are introduced in [1]-[14]. They create in-band distortion [1], peak regrowth [2], or out-of-band radiation [3]-[13]. In [14], a linear nonsymmetrical transform is given that achieves a reasonable tradeoff between PAPR reduction and bit error rate (BER) performance. Many distortionless techniques have been proposed [15]-[32]. Coding schemes [15]-[23] sacrifice the data rate. They require memory to store the codewords, and introduce delay due to the time required to find a low PAPR codeword, particularly when the number of subcarriers is large. Another class of distortionless techniques employ constellation mapping [24], [25], [42] . The constellation expansion in [42] requires a complex optimization process, particularly with a large number of subcarriers. Simpler and practical constellation mapping techniques are active constellation extension [24] and tone reservation [25].

As distortionless phase optimization techniques [27]-[32], partial transmit sequence (PTS) [26]-[32] and selective mapping (SLM) [26]-[37] offer significant PAPR reduction with a small amount of redundancy. With SLM, multiple sequences are generated by phase rotating the original data block and the sequence with the lowest PAPR is selected for transmission. Randomly chosen phase sequences lead to lower PAPR compared to other schemes such as adjacent and equally spaced. In the PTS approach [27], disjoint subblocks of OFDM subcarriers are phase shifted separately after the IFFT is computed. If the subblocks are optimally phase shifted, they exhibit minimum PAPR and consequently reduce the PAPR of the merged signal. The number of subblocks and their partitioning scheme determine the PAPR reduction. The search for optimum subblock phase factors is computationally complex, but this can be reduced with adaptive PTS [28] or sphere decoding [32]. Pseudo-random PTS and M-sequence subblock partitioning have been found to have better PAPR reduction compared to contiguous and non-contiguous subblocking schemes. Typically, the receiver requires side information corresponding to the optimal phases in PTS

and the transmitted sequences in SLM. Techniques for avoiding explicit side information transmission are presented in [38],[26]. SLM and PTS are known as average power preserving techniques as they do not increase the average signal power. The main drawback of PTS and SLM arises from the computation of multiple IFFTs, resulting in a complexity proportional to the number of PTS subblocks or SLM sequences.

Another class of distortionless techniques are those that increase the average power. In tone reservation (TR) [42]-[47], a predefined set of disjoint subcarriers in an OFDM system is reserved to generate peak reduction signals. The transmitter does not send data on this set of subcarriers and they are orthogonal to the data subcarriers. Consequently, these added signals do not distort the data carrying subcarriers and recovering the data at the receiver is trivial. These peak reduction signals are used to compensate for high peaks in the data bearing subcarriers. TR is particularly appropriate when there is a large number of subcarriers. The optimal adjustment of the values of the reserved tones can be formulated as a quadratically constrained quadratic program (QCQP) for complex multicarrier signals (passband), and a linear program (LP) for real multicarrier signals (baseband) [42]-[47]. Suboptimal iterative algorithms such as gradient and controlled clipping [42]-[46], [48], have been proposed which have less complexity but slightly inferior PAPR performance compared to the exact solution. Hence, they provide a tradeoff between computational complexity and PAPR reduction. However, these algorithms suffer from slow convergence after several iterations.

In [48], the controlled clipper algorithm was considered. A better tradeoff was obtained by using filtered clipping noise as the peak-reduction signal, and adaptively scaling it to reduce the PAPR. However, the resulting complexity is still high since a number of FFT and IFFT operations may be required during the iterative process.

In the suboptimal iterative algorithms, the PAPR reduction capability strongly depends on the locations and number of peak reduction tones (PRTs). These locations also affect the convergence rate of the solution. As indicated in [42]-[46], the optimal peak reduction kernels can be computed off-line or during the initialization process if the channel is static.

However when the channel is not static, the PRT locations and consequently the peak reduction kernels should be updated as the channel varies [42]-[46]. This creates significant computational complexity. Side information must also be transmitted in order to identify the reserved tones at the receiver.

Most research on analyzing and improving the above techniques employs direct computation of the inverse discrete Fourier transform (IDFT), which is not practical for implementation. This thesis is concerned with the development and performance analysis of distortionless techniques in conjunction with radix inverse fast Fourier transform (IFFT) algorithms which are capable of reducing the peak-to-power average (PAPR) of the original OFDM signal at the transmitter side.

1.2 Contributions and Organization of the Thesis

Following this introductory chapter, a general overview of OFDM is presented in Chapter 2. We first review early filter-bank based and the present fast Fourier transform (FFT) based implementations of an OFDM transceiver. Subsequently, the major elements of an OFDM transceiver are described. The capability of OFDM system to combat the effects of time dispersive wireless channels is reviewed. This chapter focuses on the major drawback of OFDM i.e., the high peak-to-average power ratio (PAPR), its statistical description and its effects are reviewed.

In Chapter 3, we provide an overview of different PAPR reduction techniques. A survey of PAPR reduction techniques proposed in the literature is presented, and their main features are described and analyzed. We demonstrate that PTS, SLM, and TR are particularly promising reduction techniques. This is followed by a detailed analysis of the performance and computational complexity with regards to the implementation of these techniques.

Chapter 4 presents the first contribution of this dissertation. A recursive expression for IFFT algorithms is derived using a divide-and-conquer algorithm. We develop this expression in terms of the submatrices of the identical inverse discrete Fourier transforms

(IDFTs). This enables us to introduce the concept of intermediate stages of the IFFT algorithm. These submatrices are used to formulate the time-domain OFDM symbols based on the input signals to the identical IDFTs and for the analysis of computational complexity. We employ the PAPR reduction techniques using the intermediate stages of IFFT algorithms. This leads to a new class of IFFT-based PAPR reduction techniques.

The second contribution, presented in Chapter 5, is on the computational complexity of phase optimization techniques. For IFFT-based PTS, we first use two well-known IFFT algorithms, decimation in time (DIT) and decimation in frequency (DIF), for subblock partitioning. It is shown that DIF achieves low multiplicative complexity in generating time-domain PTS sequences compared to that with DIT and the same PAPR reduction. Moreover, high radix IFFT algorithms provide better PAPR reduction performance per stage with less multiplicative complexity compared with low radix algorithms. Second, the periodic auto-correlation function (ACF) of IFFT-based PTS is derived. The ACF provides a design criterion for PTS subblocking to reduce the PAPR. It is also shown that pseudo-random and M-sequence subblocking are not optimal as they introduce superfluous subcarriers in the subblocks. As a consequence, a new PTS subblocking technique is proposed based on error-correcting codes (ECCs). This minimizes the number of repeated subcarriers and consequently provides better PAPR reduction than pseudo-random or M-sequence subblocking.

The third contribution of this thesis is on IFFT-based SLM, which is defined similar to IFFT-based PTS. As the inputs to identical IDFTs are used for generating the SLM sequences, we show that DIF results in less multiplicative complexity than DIT. In addition, IFFT-based SLM has better PAPR reduction using higher radix algorithms. To further reduce the computational complexity and achieve a better PAPR versus complexity tradeoff, we introduce partial selective mapping which is based on multiplying the phase sequences with a randomly selected subset of the identical IDFTs. This technique significantly reduce the multiplicative complexity, while providing similar PAPR performance to original SLM (O-SLM). The additive complexity is also reduced.

Finally, in Chapter 5, the last contribution of this thesis is an efficient, low complexity approach to determine the PRT locations and compute the peak reduction kernels. We show that this new algorithm can significantly reduce the computational complexity in creating these kernels. Thus they can be updated efficiently when the channel is not static. All the analysis was done with the aid of extensive simulations using MATLAB environment.

Chapter 6 concludes this thesis, summarizing the main contributions and suggesting future works and extensions. The thesis also includes Appendix A which provides the derivation of the normalized ACF for IFFT-based PTS subblocks.

Chapter 2

OFDM Overview

Orthogonal frequency division multiplexing (OFDM) is a promising technique for the next generation of wireless communication systems. By dividing a wideband fading channel into flat narrowband channels, OFDM alleviates the effect of multipath fading using a simple one-tap equalizer. In addition, OFDM is bandwidth efficient and can be efficiently generated/detected using digital signal processing (DSP) techniques.

This chapter presents the fundamentals which will be used throughout this thesis. In Section 2.2, we introduce the main concepts of OFDM such as filter-banked and FFT based implementations, and immunity to intersymbol interference over multipath fading channel using a cyclic prefix. In Section 2.3, we present the OFDM system model and major OFDM drawbacks. Section 2.4 discusses the effect of high peaks on the OFDM signal envelope.

2.1 Historical Notes on OFDM Systems

Early research and development on OFDM systems can be traced back to the 1950s and 1960s when it had been employed in a voice band modem and in several high frequency (HF) military radios [57]-[59]. The idea was to exploit parallel data streams and frequency division multiplexing (FDM) with overlapping subcarriers to eliminate the need for high-speed equalization and to resist impulsive noise and multipath distortion along with efficiently utilizing the available bandwidth. In the early 1970s, the idea of using the discrete Fourier transform was introduced in OFDM systems [60]. Prior to this invention, OFDM

system was relatively complex since it was required the implementation an array of sinusoidal generators and coherent demodulators. This led to implementing the entire OFDM system digitally using special purpose fast Fourier transform (FFT) chips. Since then, OFDM has been used for high-speed modems [61]-[63], digital mobile communications [64] and high density recording in the 1980s. Research in the late 1980s and 1990s considered OFDM for high-bit-rate digital subscriber lines (HDSL) [65], asymmetric digital subscriber lines (ADSL) [66], very high-speed digital subscriber line (VHDSL) [66], digital audio broadcasting (DAB) [67], digital video broadcasting DVB [68], and digital television and high-definition television (HDTV) [69] . The outcome was to employ OFDM in ADSL [70], DAB [71], DVB [72] and wireless LANs (IEEE 802.11a/g) [73]-[75]. OFDM in conjunction with multi-antenna techniques is also a promising technique to extend the capacity of mobile communication systems. Multi-antenna OFDM systems are contained in evolving standards such as IEEE802.11n and IEEE802.16, e.g. broadband wireless access (BWA) [76] and its predecessor multicarrier multipoint distribution service (MMDS). In the following sections, the fundamentals of OFDM are illustrated.

2.2 The Fundamentals of OFDM Systems

In a single-carrier modulation technique, data is serially transmitted on a single carrier. However, in multicarrier modulation techniques, a high-rate data stream is converted into a number of low-rate parallel data streams which are simultaneously transmitted over a large number of subcarriers. Each carrier can be modulated individually and the group is transmitted simultaneously with appropriate frequency spacing. This multicarrier transmission brings the following benefits to communication systems:

- It generates a signal which has a large period compared to single carrier modulation techniques. This helps to combat the time dispersive effects of multipath fading channels resulting in simpler time domain equalization schemes being required.
- As each sub-stream has a low data rate, the symbol has a large duration in time. Thus,

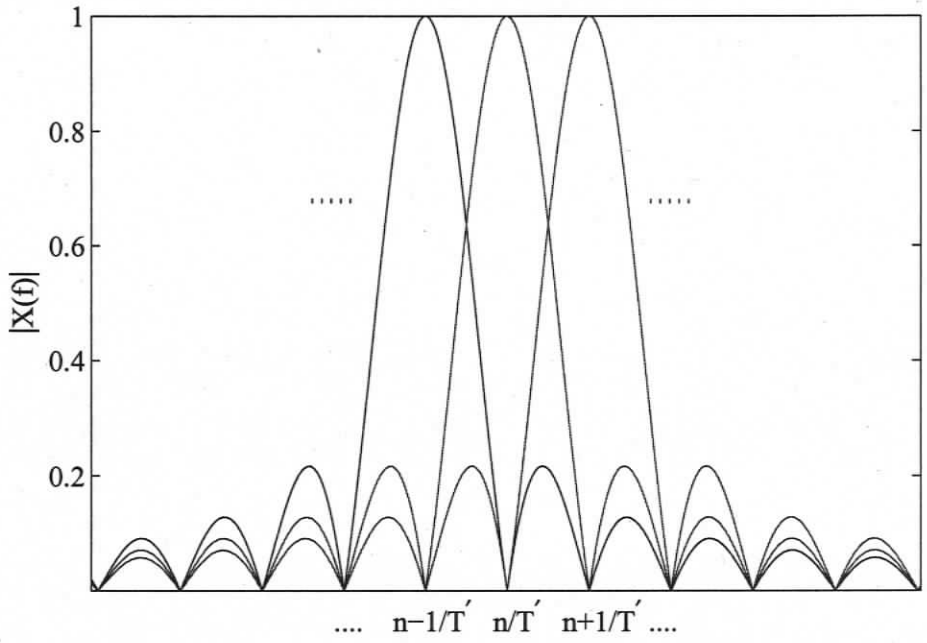

Figure 2.1. *Amplitude spectrum of an OFDM symbol.*

it is less sensitive to impulse-like noise or interference.

Multicarrier modulation techniques were originally based on frequency division multiplexing (FDM) to transmit data on multiple carriers. Non-overlaping frequency slots were allocated to different subcarriers at the transmitter and the data was recovered using filters at the receiver. However, as shown in Figure 2.1, a proper choice of the carrier spacing can allow overlapping frequency slots in such a way that each subcarrier is orthogonal to the other subcarriers. This orthogonality is defined as the integral of the product of two signals over a symbol duration being zero. This increases the bandwidth utilization and eliminates the interference between subcarriers. This is called orthogonal frequency division multiplexing (OFDM). Next, the structure of the baseband OFDM transmitter and receiver is discussed.

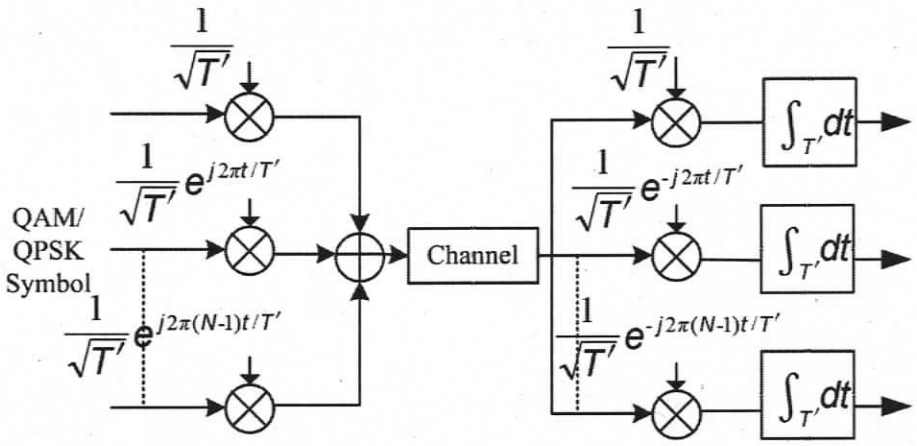

Figure 2.2. *Filter bank OFDM transceiver.*

2.2.1 Filter-bank OFDM

OFDM signals were originally constructed as a number of modulated carriers while demodulation was performed by a bank of matched filters, as depicted in Figure 2.2. This is called filter based implementation. At the transmitter, N complex data symbols are modulated on N complex orthogonal subcarriers. Then they are added for transmission. To have orthogonality between two adjacent subcarriers, they are spaced at a distance which is proportional to the inverse of the signaling interval T' (symbol period) [77]. The representation of an OFDM symbol is given by

$$x(t) = \frac{1}{\sqrt{T'}} \sum_{k=0}^{N-1} X(k) e^{j2\pi kt/T'}, \; t \in [0, T'] \tag{2.1}$$

where $\{X(k)\}_{k=0}^{N-1}$ denotes the frequency-domain signal, or a vector of quadrature-amplitude modulation (QAM) or phase-shift keying (PSK) complex symbols. At the receiver, the k-th received symbol is recovered by a corresponding matched filter. This is equivalent to multiply the OFDM symbol by the complex conjugate of the k-th subcarrier and integrating over the signaling interval. Thus, we have

$$X(k) = \frac{1}{\sqrt{T'}} \int_0^t x(t) e^{-j2\pi kt/T'} dt. \tag{2.2}$$

This performs the correlation operation to find the $X(k)$ corresponding to the k-th subcarrier in the incoming OFDM symbol. This implies that the correlation between any two different complex subcarriers is zero, i.e., they are orthogonal. Thus, there is no intercarrier interference between subcarriers. The Fourier transform of $x(t)$ is defined by

$$X(f) = \frac{1}{\sqrt{T'}} \int_{-\infty}^{\infty} x(t) e^{-j2\pi tf} dt. \tag{2.3}$$

From (2.2) and (2.3), we obtain

$$X(f) = \sqrt{T'} \sum_{k=0}^{N-1} X(k) \frac{\sin\left[\pi\left(f - \frac{n}{T'}\right)T'\right]}{\pi\left(f - \frac{n}{T'}\right)T'} e^{-j\pi(f-n/T')T'}. \tag{2.4}$$

This spectrum is depicted in Figure 2.1 which is a series of sinc functions

$$\text{sinc}\left[\left(f - \frac{n}{T'}\right)T'\right] = \frac{\sin\left[\pi\left(f - \frac{n}{T'}\right)T'\right]}{\pi\left(f - \frac{n}{T'}\right)T'} \tag{2.5}$$

and the maximum value of (2.5) corresponds to a null at the center frequency of all other subcarriers. This shows mathematically that there is no interference between the subcarriers if the spacing is $1/T'$. Implementation with a bank of matched filters and oscillators at the receiver and transmitter, respectively, is complex. However, it was shown in [60] that this complexity can be significantly reduced by using an inverse discrete Fourier transform (IDFT) at the transmitter and a discrete Fourier transform (DFT) at the receiver.

2.2.2 OFDM with IFFT/FFT implementation

As shown in [60], an OFDM signal can be generated and detected using an inverse discrete Fourier transform (IDFT) and a discrete Fourier transform (DFT) at the transmitter and the receiver, respectively. The vector $X(k)$ is transmitted using one OFDM symbol $\{x(n)\}_{n=0}^{N-1}$. The discrete time samples of $x(n)$ are computed by taking an N-point IDFT of $X(k)$

$$x(n) = \frac{1}{N} \sum_{k=0}^{N-1} X(k) T_N^{-nk} \quad 0 \le n \le N-1, \;\; 0 \le k \le N-1 \tag{2.6}$$

where n is the discrete-time index and $T_N = e^{-j2\pi/N}$ (known as the twiddle factor). In matrix notation, (2.6) is

$$\mathbf{x} = Q\mathbf{X} \tag{2.7}$$

where Q_N is the $N \times N$ IDFT matrix with elements T_N^{-k}, i.e.

$$Q = \frac{1}{N}\begin{bmatrix} 1 & \cdots & 1 & \cdots & 1 \\ \vdots & \ddots & \vdots & \ddots & \vdots \\ 1 & \cdots & T_N^{-nk} & \cdots & T_N^{-n(N-1)} \\ \vdots & \ddots & \vdots & \ddots & \vdots \\ 1 & \cdots & T_N^{-k(N-1)} & \cdots & T_N^{-(N-1)^2} \end{bmatrix}. \tag{2.8}$$

After detection at the receiver, $X(k)$ is given by [1]

$$X(k) = \sum_{n=0}^{N-1} x(n) T_N^{nk} \quad 0 \le n \le N-1, \;\; 0 \le k \le N-1 \tag{2.9}$$

To obtain the continuous-time signal $x(t)$ given in (2.1) from the discrete-time signal $x(n)$, oversampling is used where $x(t)$ is [42]

$$x(t) = \frac{1}{\sqrt{N}} \sum_{k=0}^{N-1} X(k) e^{j2\pi\Delta f t/T'}, \; t \in [0, T'] \tag{2.10}$$

and N subcarriers span a bandwidth of BW Hz and are separated by a spacing of $\Delta f = BW/N$. The symbol period is $1/T'$. The OFDM symbol bandwidth or IDFT output symbol rate is N/T'. If this sampling rate is used, the amplitude spectrum of the IDFT output is similar to Figure 2.3. In this case, a filter cannot be realized with the sharp transitions to recover the continuous-time OFDM symbol from its samples. Thus, as shown in [42], oversampling is employed. This is done by adding $JN - N$ zeros in the end of the input to the N-point IDFT at the transmitter and removing the last $JN - N$ DFT output values at the receiver where J is the oversampling factor. In other words, a JN-point IFFT is used. Hence, (2.6) is given by

$$x(n) = \frac{1}{JN} \sum_{k=0}^{N-1} X(k) T_{JN}^{-nk} \quad 0 \le n \le JN-1, \;\; 0 \le k \le N-1 \tag{2.11}$$

[1] Note that we ignore channel noise and interference in this analysis

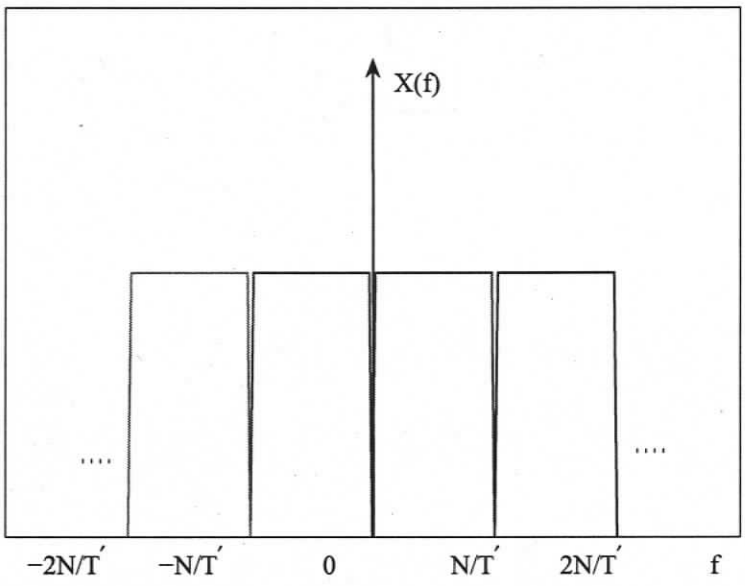

Figure 2.3. *Amplitude spectrum of an IDFT output with sampling factor* $J = 1$.

The amplitude spectrum of the IFFT output with oversampling is depicted in Figure 2.4.

An IDFT/DFT can be efficiently implemented using an inverse fast Fourier transform (IFFT)/ fast Fourier transform (FFT). This reduces the complexity from $O(N^2)$ to $O(N\log N)$. Such an implementation makes the OFDM modulator/demodulator comparable to the equivalent single-carrier modulator/demodulator in terms of complexity and silicon area [60].

2.2.3 OFDM system model

A block diagram of an OFDM system is illustrated in Figure 2.5. The serial input bit stream is sent to a QAM/QPSK constellation mapper which outputs N parallel constellation points representing the data. The OFDM discrete time symbols are obtained by performing the IFFT of these N samples. The parallel time-domain samples x are then converted to a serial stream. To avoid ISI and inter block interference (IBI), a cyclic prefix (CP) is appended before an OFDM symbol with a duration longer than the maximum delay t_0 due to different

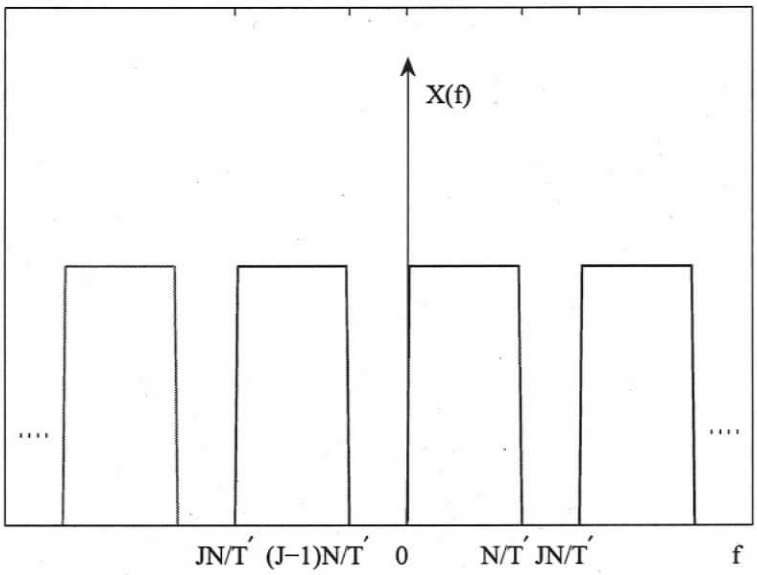

Figure 2.4. *Amplitude spectrum of an IDFT output with sampling factor* $J > 1$.

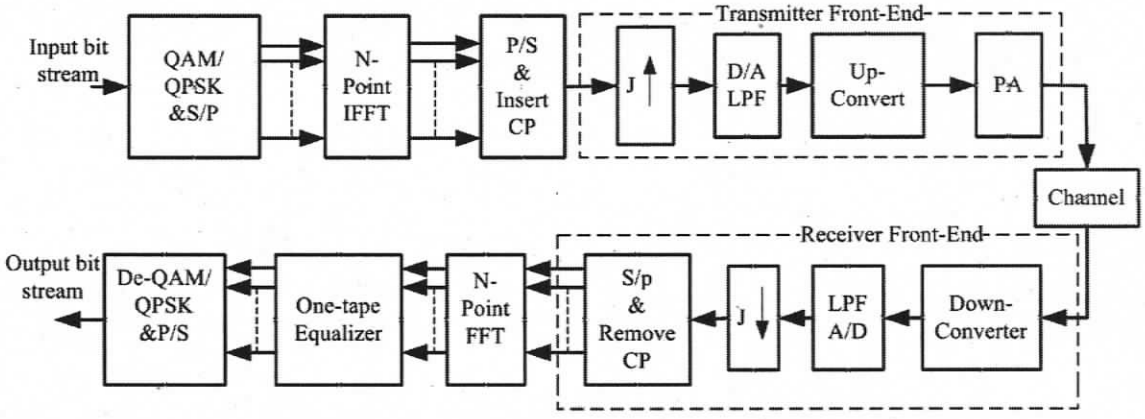

Figure 2.5. *The OFDM system model.*

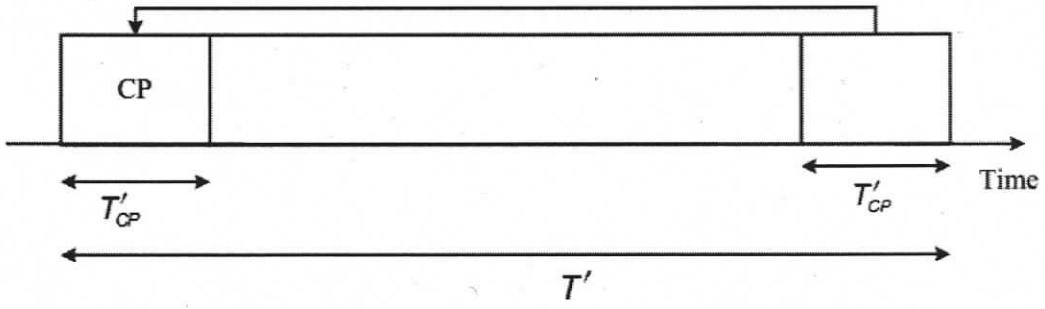

Figure 2.6. *Time representation of an OFDM symbol with CP.*

propagation paths [42]. This is formed by coping the last T'_{CP} samples of the IDFT output to the beginning of the OFDM symbol, as shown in Figure 2.6. Hence, the transmitted OFDM symbol can be expressed as $\mathbf{x}_{cp} = [x(N-t_0), \ldots, x(N-1), x(0), \ldots, x(N-1)]$. The sequence is oversampled, converted to an analog signal, up converted to the carrier frequency, amplified, and finally transmitted through the multipath channel which is assumed to be time-invariant within one OFDM symbol duration T'. Hence, the channel impulse response is $\mathbf{h} = [h(0), h(1), \ldots, h(t_0-1)]$. At the receiver, the received signal can be expressed as [42]

$$\mathbf{z}_{CP} = \mathbf{x}_{CP} * \mathbf{h}$$

$$\mathbf{z}_{CP} = [x(-t_0), \ldots, x(N+t_0-2)] * [h(-t_0), \ldots, h(N+t_0-2)]\,. \tag{2.12}$$

The received signal without the CP is

$$\mathbf{z} = x * \mathbf{h} \tag{2.13}$$

where $(*)$ denotes N circular convolution by N. Finally, the discrete Fourier transform (DFT) operation is performed on each of these symbols and the frequency-domain received signal is obtained

$$X = DFT\,[\mathbf{z}]\,H^{-1} \tag{2.14}$$

where the channel response H is known. Based on (2.14), the frequency-domain X is equalized. Hence, with a CP OFDM symbols can be equalized one symbol at a time which greatly simplifies receiver equalization.

2.3 OFDM Major Drawbacks

The RF front-end of the OFDM transceiver (see Figure 2.5) causes several major impairments which impact on system performance. First, a power amplifier with a nonlinear transfer function can generate in-band and out-of-band distortion which introduces interference on adjacent channels. Second, random phase noise in the local oscillators causes constellation rotation and intercarrier interference (ICI). Finally, frequency offset occurs when there is a difference between the transmitter and receiver local oscillators due to oscillator errors and/or doppler spread. Frequency offset introduces ICI. Next, we focus on the first impairment which is caused by large variations in the OFDM signal envelope.

2.3.1 Peak power and its effects

Consider a typical transfer function of a nonlinear power amplifier (PA) which is illustrated in Figure 2.7 where $P_{in,ave}$ and $P_{o,ave}$ are the average input and output powers, respectively. The saturation power input and output is defined as $P_{in,sat}$ and $P_{o,sat}$. This figure shows three PA operation regions: a linear region , $P_{in} < P_{in,ave}$, a nonlinear region, $P_{in,ave} < P_{in} < P_{in,sat}$, and a saturation region, $P_{in} > P_{in,sat}$. Within the linear region, the output power is a scaled version of the input power. The PA gain reduces in the nonlinear region and the output power has the maximum value in the saturation region.

If the modulated QAM/QPSK complex symbols $X(k)$ add constructively, they can generate a time domain signal with a large amplitude. Thus, the output signal $x(n)$ can have high peak values. As an example, Figure 2.8 shows the signal envelope from 4 modulated subcarriers. Signal peaks with a power much higher than the average can exceed the amplifier's linear range (powers that exceed $P_{in,sat}$), causing clipping of the OFDM signal. This clipping has an impact on the received signal constellation similar to additive noise if the clipping occurs frequently [42]. The effect of such a phenomenon is illustrated in Figure 2.9 with a 16-QAM constellation and $N = 256$. This introduces in-band distortion similar to the additive Gaussian noise and increases the bit error rate (BER) at the receiver.

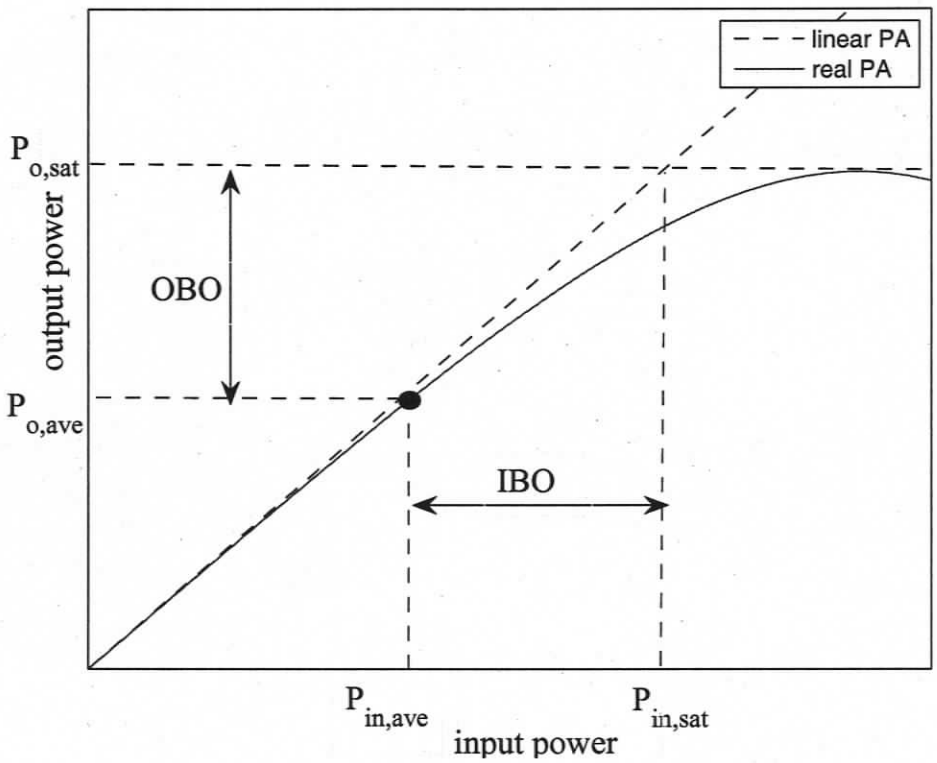

Figure 2.7. *A typical power amplifier (PA) transfer function.*

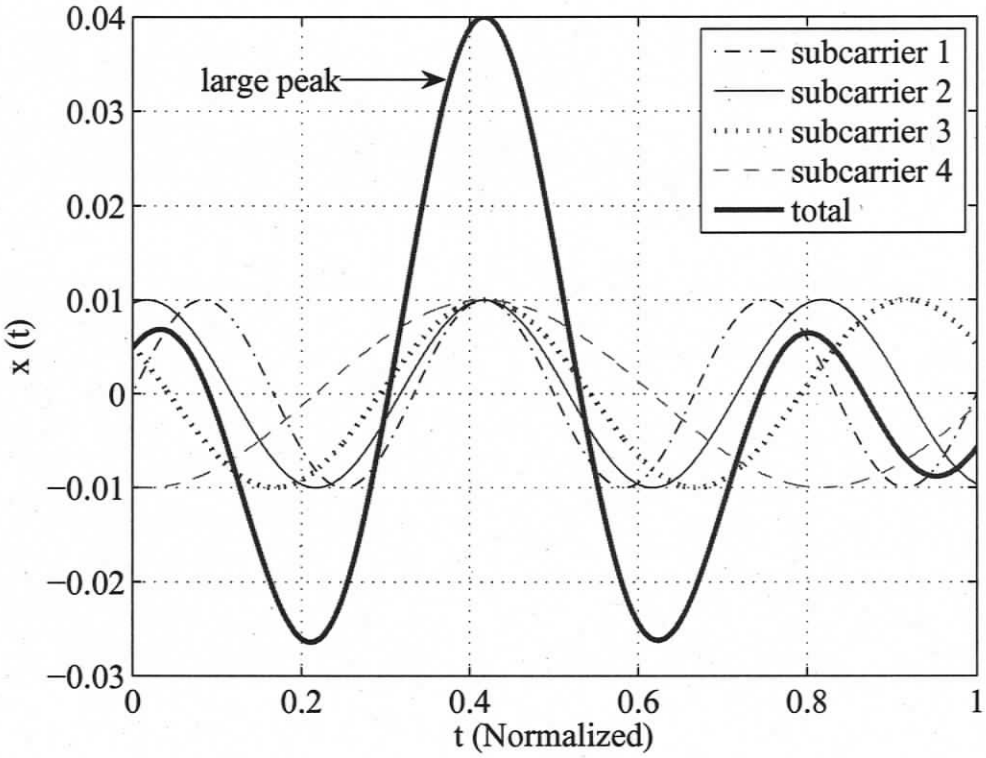

Figure 2.8. *Time representation of an OFDM symbol with 4 subcarriers.*

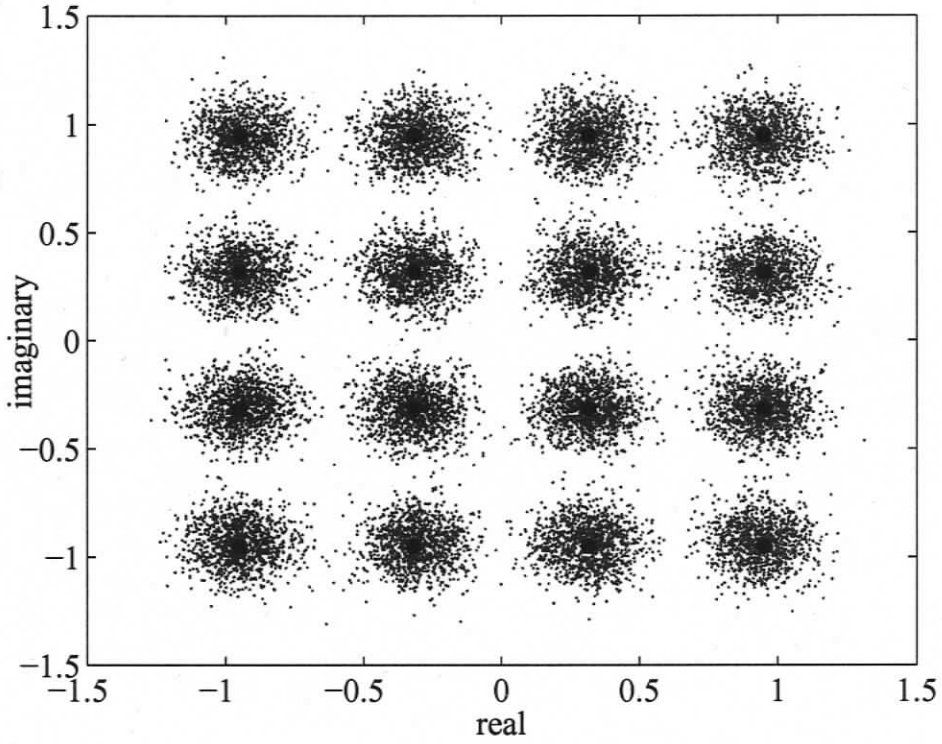

Figure 2.9. *Effect of clipping noise on the received OFDM signal for 1000 OFDM symbols with a 16-QAM constellation, N=256, IBO=5 dB.*

It also presents out-of-band radiation outside the spectrum of OFDM signal (see Figure 2.10), which introduces interference in adjacent channels.

Nonlinear distortions depend on the input back-off (IBO) or output back-off (OBO) defined (see Figure 2.7) as

$$\text{IBO}_{dB} = 10log_{10}\frac{[max\,(x(t))]^2}{E[|x(t)|^2]} = 10log_{10}\frac{P_{in,sat}}{P_{in,ave}} \tag{2.15}$$

and

$$\text{OBO}_{dB} = 10\log_{10}\frac{P_{o,sat}}{E\,[|\hat{x}(t)|^2]} = 10log_{10}\frac{P_{o,sat}}{P_{o,ave}} \tag{2.16}$$

, respectively [80] where $\hat{x}(t)$ is the amplified OFDM signal. The amplifier saturation power is defined as $P_{o,sat} = A^2$ where A is the output saturation level. Figure 2.10 shows the power spectral density of an OFDM signal with $N = 256$ subcarriers for different values of IBO. The spectral spreading is generated by the nonlinear distortion. In the following, we will consider Rapp's solid state power amplifier (SSPA) model [80] with AM/AM and AM/PM characteristics given by

$$[\breve{x}(t)]_{AM} = \frac{x(t)}{(1+|\frac{Gx(t)}{A}|^{2\epsilon})^{1/2\epsilon}}$$

and

$$[\breve{x}(t)]_{PM} = 0 \tag{2.17}$$

, repectively. The parameter ϵ controls the smoothness of the characteristics and G is the amplifier small signal gain. We will assume that the SSPA has typical parameters $G = 1$ and $\epsilon = 10$ for a soft limiter [80].

To control the effect of nonlinear distortion, one can force (scale) the operation of the PA into the linear region or increase the IBO. However, PAs are more power efficient when operating close to the saturation region [80]. In addition, for the same transmitted power, this increases power consumption and the cost of hardware devices.

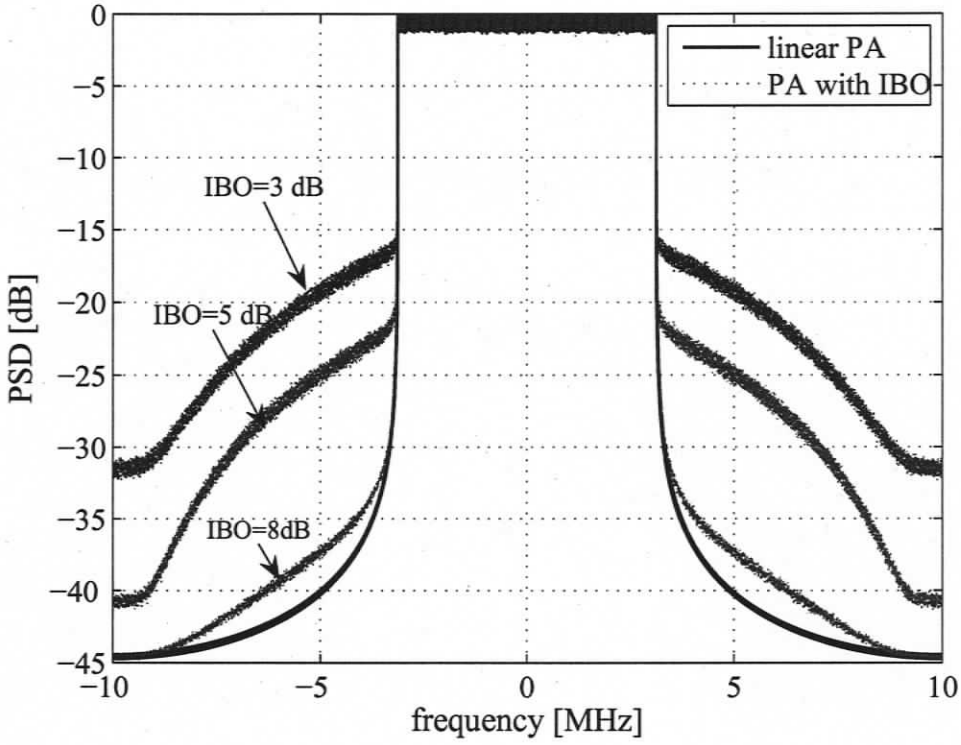

Figure 2.10. *Power spectral density of an OFDM signal for different IBO values where* $N = 256$, $J = 4$, $G = 1$, $A = 1$, *and* $\epsilon = 10$.

2.3.2 Peak-to-average power ratio (PAPR)

To evaluate the variation in the time domain samples, the most popular metric is the peak-to-power average ratio (PAPR). For the OFDM systems shown in 2.5, the PAPR of $\mathbf{x}$ is defined as

$$\text{PAPR}(\mathbf{x}) = \frac{\|\mathbf{x}\|_\infty^2}{E\left[\|\mathbf{x}\|_2^2\right]/N} \tag{2.18}$$

where $\|\mathbf{x}\|_\infty$, $\|\mathbf{x}\|_2$, and $E[.]$, denote the ∞-norm and 2-norm of $\mathbf{x}$, and expectation, respectively. $X(k)$ is assumed to be statistically independent and identically distributed (i.i.d.). Hence, for large N, the central limit theorem implies that the imaginary and real parts of $x(n)$ are asymptotically i.i.d. Gaussian random variables with zero mean and variance $\sigma^2_{\text{imag}[x]} = \sigma^2_{\text{real}[x]} = \sigma_x^2/2$ where $\sigma_x^2 = E[|X(k)|]^2$. It then follows that the instantaneous power of the discrete-time samples $x(n)$ becomes central chi-square distributed with two degrees of freedom and zero mean. The cumulative distribution function (CDF) for a particular value $n = n_0$ is

$$P_r\left[|x(n_o)|^2 < \delta\right] = 1 - e^{-\sigma_x^2 \delta} \tag{2.19}$$

where δ is threshold level. Since $x(n)$ is generated using an IFFT, the discrete time samples $x(n)$ can be assumed mutually independent [42]. Thus, the the probability that the power of a least one $x(n)$ out of N samples exceeds the threshold level δ is

$$P_r\left[\max_{0\le n<N-1} |x(n)|^2 < \delta\right] = (1 - e^{-\sigma_x^2\delta})^N. \tag{2.20}$$

If σ_x^2 is normalized to unity, the complementary cumulative distribution function (CCDF) of the PAPR is

$$P_r\left[\text{PAPR}(x(n)) > \delta\right] = 1 - (1 - e^{-\delta})^N. \tag{2.21}$$

For oversampled OFDM signals, the CCDF of JN oversampled OFDM signal is

$$P_r\left[\text{PAPR}(x(n)) > \delta\right] = 1 - (1 - e^{-\delta})^{JN}. \tag{2.22}$$

In Figure 2.11, the theoretical CCDF of the PAPR using (2.22) is plotted for various values of J with $N = 256$. The PAPR for $J = 4$ is almost identical to the case with $J = 8$, which

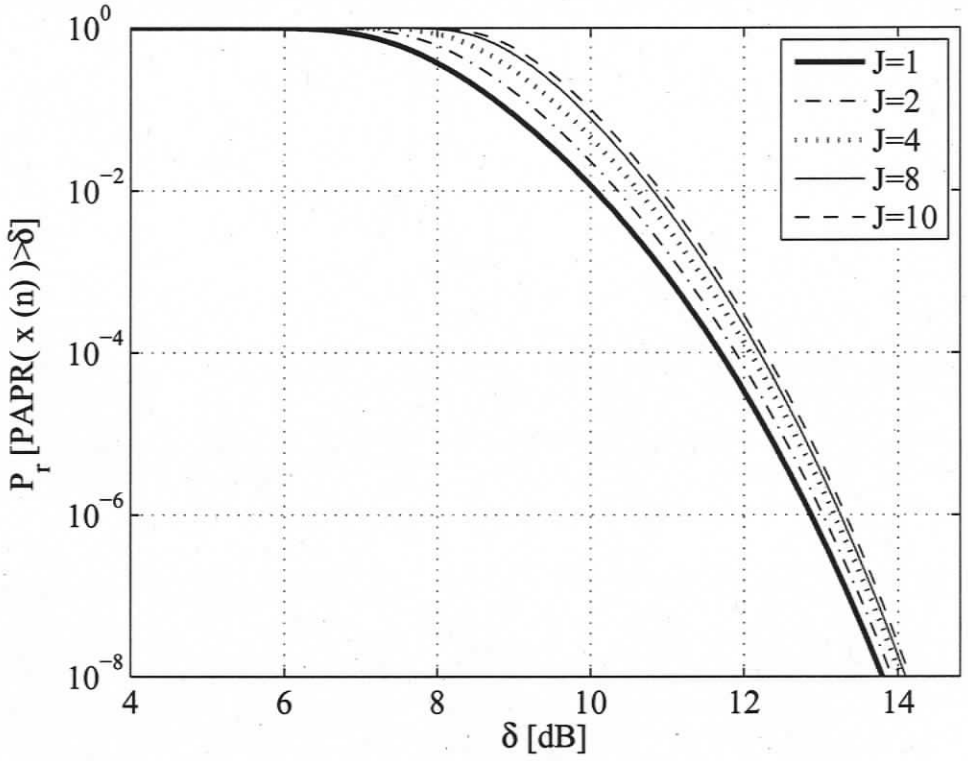

Figure 2.11. *CCDF of PAPR for different oversampling factors J with $N = 256$ and 16QAM subcarrier modulation.*

is indistinguishable from larger J values. Consequently, we set $J = 4$ for the remainder of this thesis. Figure 2.12 is a plot of the PAPR of $x(n)$ for different values of N with $J = 4$. It is obvious that the PAPR increases with N. The simulated values of CCDF are plotted in the same figure using dashed curves. The simulation consisted of 10^6 OFDM symbols with 16-QAM modulated subcarriers. From the plot we can see that the numerical CCDF is very close to the CCDF derived in (2.20).

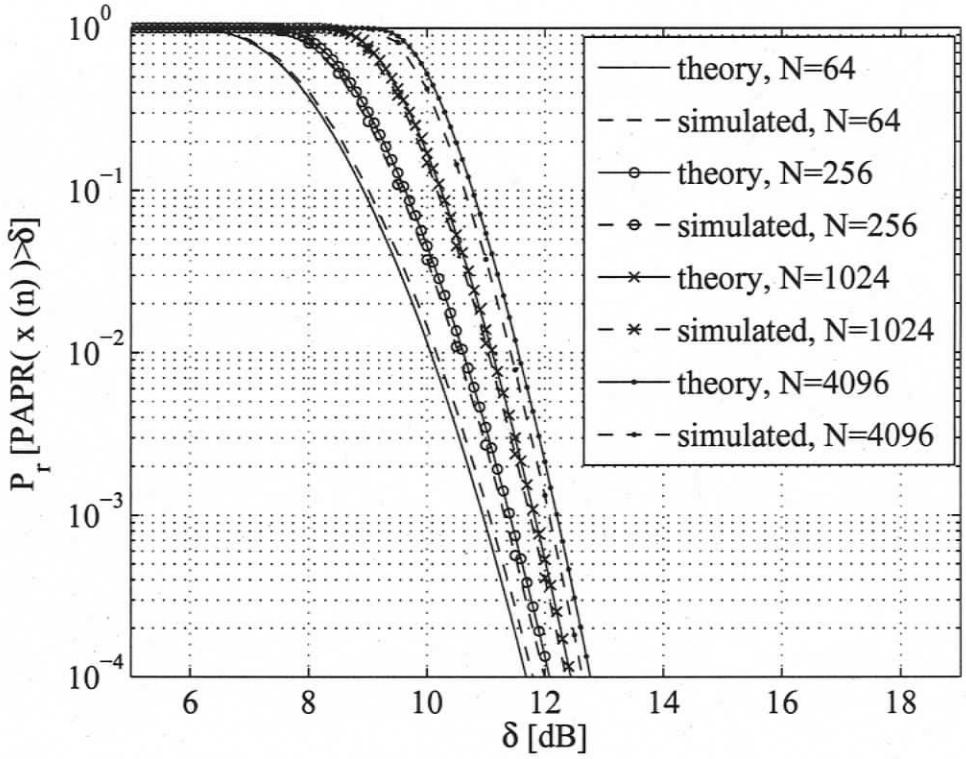

Figure 2.12. *Theoretical and numerical CCDF of the PAPR for different values of N with $J = 4$.*

Chapter 3

Techniques for PAPR Reduction

The previous chapter inroduced OFDM modulation and its main features, along with the major disadvantage of OFDM, i.e., a high Peak-to-Average power Ratio (PAPR). This chapter gives an overview of the most well known techniques that reduce nonlinear distortion at the transmitter. These techniques decrease the PAPR of the transmitted signal with some modification of the OFDM signal prior to the power amplifier.

The most straightforward PAPR reduction techniques such as clipping and companding are distortion techniques which distort the original signal, increasing the out-of-band radiation and the bit error rate. Approaches proposed in the literature that reduce the PAPR without generating distortion (out-of-band radiation) are called distortionless techniques. Among them, the most well known techniques are tone reservation (TR), tone injection (TI), coding, selective mapping, and partial transmit sequence (PTS). The major indicators for the effectiveness of these PAPR reduction techniques can be summarized as: the PAPR reduction capability, implementation complexity, and data rate loss. In the following, these factors are considered to describe and analyze the techniques above. Those distortionless techniques which are the most promising will be thoroughly analyzed. The next chapter introduces IFFT-based distortionless techniques. They will be compared in detail with existing distortionless techniques in Chapter 5.

3.1 Distortion PAPR Techniques

Distortion techniques are PAPR reduction schemes which introduce spectral regrowth. They have low computational complexity and do not require any side information to be sent to the receiver. These techniques distort the spectrum. This can be corrected by filtering, but at the cost of reproducing the peaks that were initially reduced.

3.1.1 Clipping

The simplest distortion technique is to clip the high amplitude peaks which exceed a specific threshold A_0 without modifying the phase information, i.e.

$$x_{\text{clip}}(n) = \begin{cases} x(n) & |x(n)| \leq A_0 \\ A_0 & |x(n)| \geq A_0 \end{cases} . \tag{3.1}$$

Clipping the time domain signal affects the received signal and creates out-of band radiation (spectral regrowth) and in-band distortion. The value A_0 determines the amount of out-of band radiation. If the value A_0 is too small, the out-of band radiation can be large [8]. To reduce the out-of band distortion, filtering can be applied, but this causes the peak regrowth [1], [10]. Iterative clipping and filtering techniques [9]-[11] have been proposed to alleviate the drawbacks of filtering. The proposed iterative techniques in [9], [10] require a number of iterations to decrease the peak regrowth. Two IFFT/FFT operations are required for each iteration, hence they are computationally intensive. To improve the computational complexity, in [11] it was shown that the clipping noise after several iterations is approximately proportional to that generated in the first iteration. Hence, the number of FFT/IFFT operations can be reduced to as low as three FFT/IFFT operations. Although the proposed iterative clipping and filtering technique in [11] reduces the number of FFT/IFFT operations to the equivalent of 6 FFT operations this is still high for real-time implementation, in particular when the number of subcarriers is very large.

The in-band distortion generates clipping noise which increases the error rate. This phenomenon was modeled in [2], [7] as approximately independent additive white Gaus-

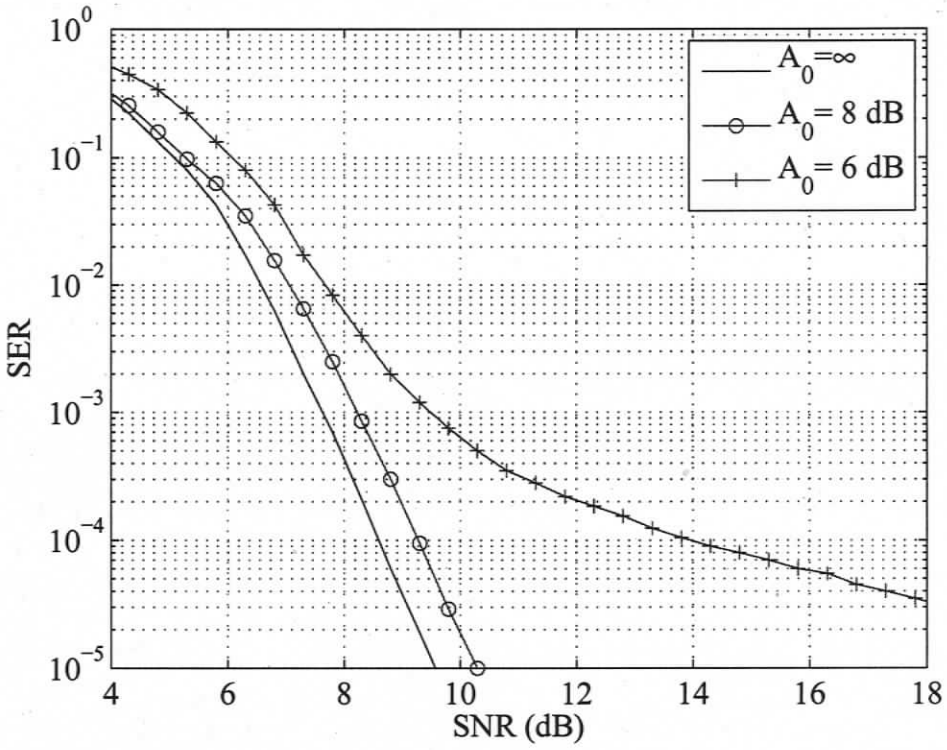

Figure 3.1. *Symbol error rate of clipped OFDM symbols for* $N = 256$ *and QPSK constellation mapping. The unclipped signal,* $A_0 = \infty$ *, is shown along with clipping levels* $A_0 = 6, 8$ *dB.*

sian noise. Figure 3.1 shows the symbol error rate (SER) with QPSK for various clipping levels. As can be seen, clipping results in an increasing error rate which grows significantly as A_0 is decreased. In order to maximize the signal-to-noise-and-distortion ratio (SNDR) , an optimal function based on a soft clipper was proposed in [6].

Intuitively, the PAPR of an OFDM signal and the amount of PA IBO determines the probability of clipping. This is because signals with a low PAPR are less often clipped than signals with a high PAPR. For a given clipping probability, the effect of PA IBO on the clipping probability was analyzed in [95].

3.1.2 Companding

As discussed in Chapter 2, from the central limit theorem it follows that for large values of N, the samples of an OFDM signal becomes Gaussian distributed [12]. Hence, an OFDM signal is a similar to a speech signal. In speech signal processing, companding is used to expand the dynamic range of digital to analog converters (DACs). This similarity was exploited in [12] to reduce the PAPR of an OFDM signal. In this technique, the OFDM samples $x(n)$ are companded by a compression function $\vartheta(.)$ at the transmitter. The compressor output $x_{\text{com}}(n)$ is given by

$$x_{\text{com}}(n) = \frac{A' \operatorname{sgn}[x(n)] \ln\left[1 + \mu \frac{x_n}{A'}\right]}{\ln(1+\mu)} \tag{3.2}$$

where sgn[.] denotes the sign function, A' is a normalization constant such that $0 \leq \left|\frac{x(n)}{A'}\right| \leq 1$ and $\vartheta(.)$ is the μ-law companding function. In the receiver, the expanding function $\vartheta^{-1}(.)$. is used to the received signal $\mathbf{Z}$. μ-Law companding enlarges small signals and consequently increases the average power of the signal thus reducing the PAPR. This is illustrated in Figure 3.2 where the waveform of a 16-QAM OFDM signal with $N = 64$ is compared with μ-Law companded of the same signal using $\mu = 255$. Other companding schemes adjust both small and large signals and offer better performance in terms of PAPR reduction and error rate [13]. However, the drawback to companding is that when the received symbol is expanded, any noise from the channel is amplified, degrading system performance. In terms of spectral regrow, companding affects the rectangular-like power spectrum of OFDM signal. Similar to clipping, companding has slower spectrum roll-off, resulting in more side-lobes compared to the spectrum of the original OFDM signal.

3.2 Distortionless PAPR Techniques

Distortionless PAPR reduction techniques do not introduce any spectral regrowth in the OFDM spectrum. However, some of them add noise to the system, increasing the error rate. Some require side information to be sent to the receiver in order to recover the original data.

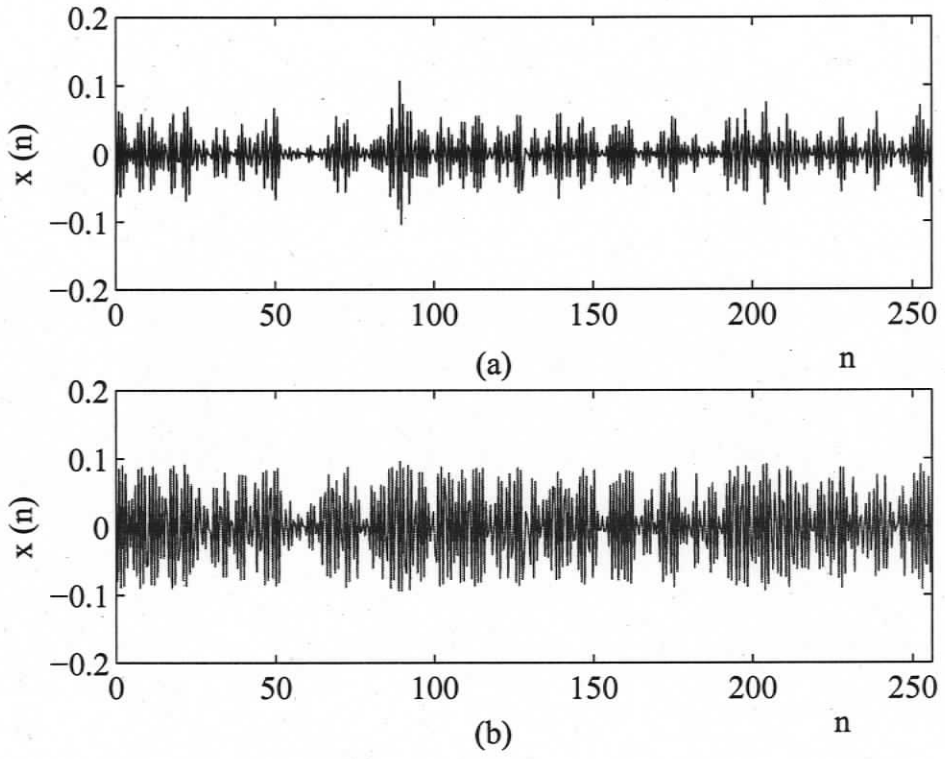

Figure 3.2. *Waveforms for an OFDM signal and the same signal companded for* $N = 64$, $J = 4$. *(a) original signal. (b)* μ*-law companded signal with* $\mu = 255$.

The need for side information reduces bandwidth efficiency and increases the amount of processing at the receiver. The major distortionless techniques which significantly reduce the PAPR have high computational complexity.

3.2.1 Coding

The idea of coding techniques is to use an appropriate form of channel coding which prevents transmitting symbols that possess a large PAPR. The first class of coding technique is based on systematic coding. Amongst all possible OFDM symbols, symbols are chosen for transmission that exhibit a low PAPR. In another words, high PAPR data sequences are coded into a finite number of low PAPR data sequences. It is obvious this approach results in a data rate reduction. Examples of this technique are binary Golay codes suggested in [16] and [17]. Another approach based on systematic coding using block coding and cyclic coding has been proposed in [20] and [19], respectively. The idea is to obtain all possible codewords and compute their resulting PAPR, then, eliminate those codewords that exceed a predefined threshold. Further, the similarity between the PAPR and peak interference-to-carrier ratio (PICR) was exploited in [21] to propose a Golay complementary repetition code to simultaneously reduce the PAPR and PICR.

The systematic coding techniques require an exhaustive search to locate the low PAPR code words for transmission and large lookup tables for coding and decoding. Hence, they are appropriate only for OFDM systems with a small number of subcarriers.

The second class of coding schemes randomly generate symbol mappings and determine which generate low-PAPR symbols. Examples are [37] and [38]. In [37], interleaving in conjunction with a feedback shift register was used to generate independent mappings. In order to detect the transmitted sequence at the receiver, a number of prefix labels is inserted before mapping at the transmitter. The idea of using a feedback shift register was used in [38] to create a repeat accumulate code in order to reduce the PAPR and BER.

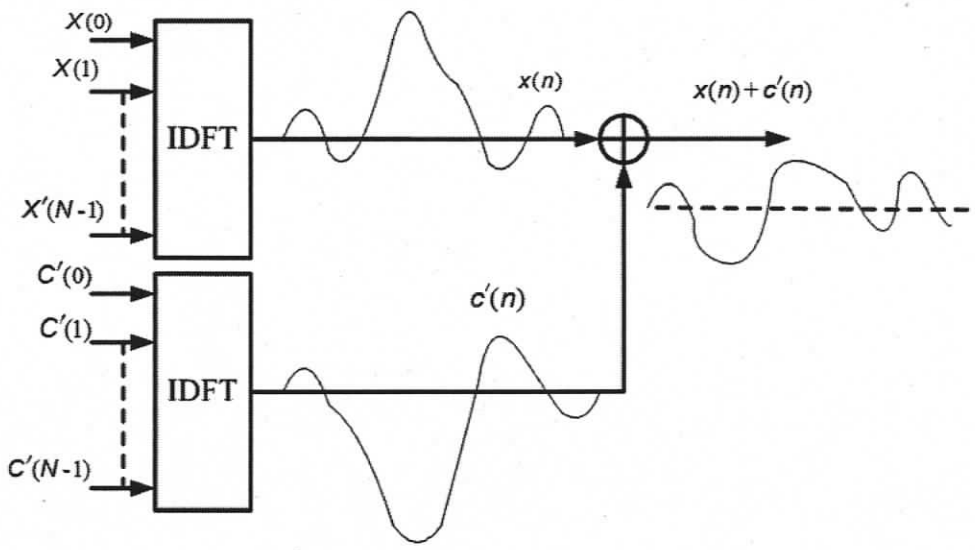

Figure 3.3. *Block diagram for the tone injection PAPR reduction technique.*

3.2.2 Tone injection

Tone injection (TI) was introduced by Tellado in [42]. This technique is based on enlarging the original constellation size. Therefore the expanded constellation consists of several equivalent points corresponding to the original constellation. The extra constellation points are exploited for PAPR reduction by shifting copies of the original constellation.

As shown in Figure 3.3 [42], the mapping of the original points within the primary constellation by the alternative points located in the extended constellation is similar to injecting tones in the OFDM symbol. These tones should be designed based on an appropriate amplitude and phase to reduce PAPR. Consider an M_{QAM} array QAM constellation with a minimum distance between constellation points of $d(k)$. Then, the real part of $X(k)$, $X_{\text{real}}(k)$ and the imaginary part, $X_{\text{imag}}(k)$, can take values $\left\{\pm d(k)/2, \pm 3d(k)/2, \ldots, \pm\left(\sqrt{M_{\text{QAM}}(k)}-1\right) d(k)/2\right\}$, where $\sqrt{M_{\text{QAM}}(k)}$ is the number of levels per dimension [42]. The original constellation points $X(k) = X_{\text{real}}(k) + X_{\text{imag}}(k)$ are mapped into

$$\ddot{X}(k) = X(k) + C'(k) = [X_{\text{real}}(k) + \rho(k)D(k)] + j\,[X_{\text{imag}}(k) + \zeta(k)D(k)] \qquad (3.3)$$

where $D(k) \geq \sqrt{M_{\text{QAM}}(k)}$ and the integers $\rho(k)$ and $\zeta(k)$ are selected such that they reduce the PAPR. As an example, Figure 3.4 illustrates the TI technique for a 4-QAM constellation where there are 8 possible positions for each symbol. The filled and unfilled shapes represent points in the original constellation and the equivalent points in the expanded constellation, respectively. At the receiver, the components $\rho(k)$ and $\zeta(k)$ in (3.3) are removed after equalization by taking the modulo D of the real and imaginary components of the received signal.

Since the expanded symbols $\ddot{X}(k)$ in (3.3) are obtained with $\rho(k) \neq 0$, $\zeta(k) \neq 0$, and $D(k) \geq \sqrt{M_{\text{QAM}}(k)}$, they may have more power than the original symbol $X(k)$. This can create secondary peaks, resulting in performance degradation. Another drawback of TI is the high complexity associated with the optimization problem to find optimal expanded constellation.

3.2.3 Partial transmit sequence (PTS)

Partial Transmit Sequence (PTS) generates different versions of the same symbol by phase-rotating the time domain OFDM signal. This was introduced in [27] as a PAPR reduction scheme. With PTS (see Figure 3.5), the frequency domain vector $X(k)$ is partitioned into P disjoint subblocks $X_p(k) = [X_p(0), \ldots, X_p(N-1)]^T, 0 \leq p \leq P-1$ that are zero-padded to be of length N so that

$$X(k) = \sum_{p=0}^{P-1} X_p(k). \tag{3.4}$$

An example of $N = 16$ subcarriers is illustrated in Figure 3.6 where the symbol vector $X(k)$ is divided into $P = 4$ vectors and each vector $X_p(k)$ is assigned to a subblock of N/P adjacent, equally spaced, random subcarriers. The combination of these subblocks with rotated phase factors $e^{j\theta_p}$ yields the alternative frequency domain vectors with

$$X'(k) = \sum_{p=0}^{P-1} e^{j\theta_p} X_p(k). \tag{3.5}$$

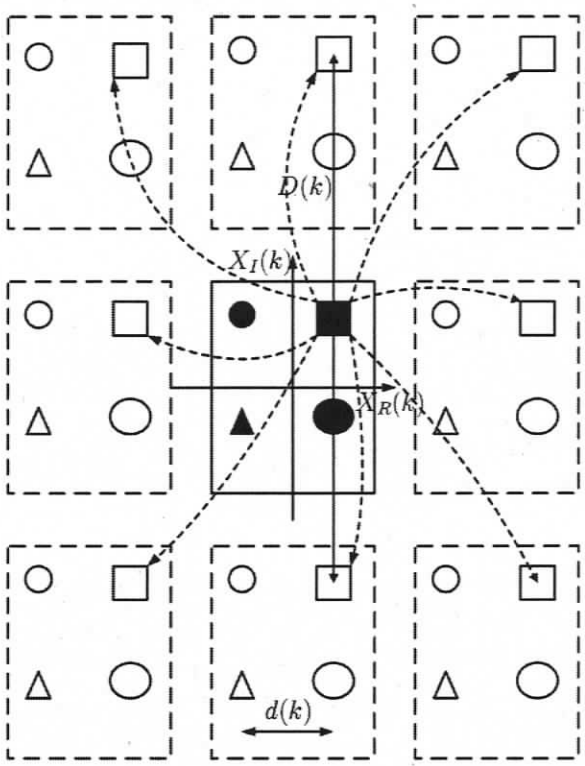

Figure 3.4. *Example of mapping a 4-QAM symbol into a 32-QAM symbol in the tone injection method.*

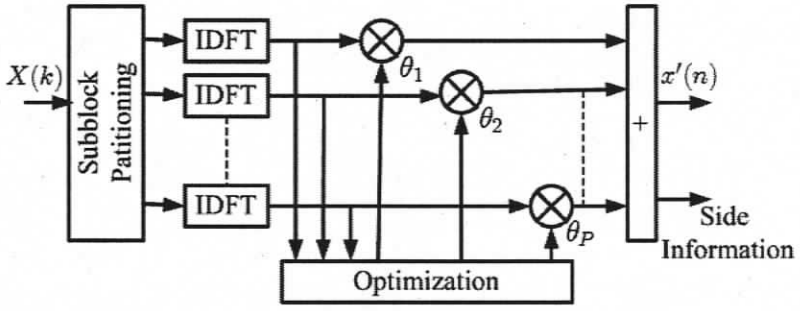

Figure 3.5. *Block diagram for the partial transmit sequence PAPR reduction technique.*

These subblocks are optimally phase rotated to achieve a reduced PAPR signal $x(n)$. Since each subblock is independently rotated by a phase factor θ_p, the phase factor multiplication can be performed after the IDFT computation. This is an advantage as the PAPR can be computed without having to go back and forth between the time and frequency domains. Hence, we can take the IDFT of (3.5), and exploit the linearity of the IDFT to obtain

$$x'(n) = \sum_{p=0}^{P-1} e^{j\,\theta_p} \text{IDFT}_{N\times N}(X_p(k)) = \sum_{p=0}^{P-1} e^{j\,\theta_p} x_p(n) \tag{3.6}$$

where $x_p(n) = \text{IDFT}_{N\times N}(X_p(k))$ are the P time-domain partial transmit sequences. $\text{IDFT}_{N\times N}(X_p(k))$ is the IDFT of the N dimensional vector $X_p(k)$ and results in an N dimensional vector $x_p(n)$. The sequence $x'(n)$ with the smallest PAPR is chosen for transmission based on the following criterion

$$[\acute{\theta}_1, \ldots, \acute{\theta}_{P-1}] = \underset{\theta_1,\ldots,\theta_{P-1}}{\text{argmin}} \left\{ \max_{0\le n<N} |x'(n)|^2 \right\}. \tag{3.7}$$

Assuming W is the number of phase values and $\theta_0 = 0$, the search complexity to find the lowest PAPR sequence is W^{P-1}. To have an efficient implementation, the phase factors can be restricted to values in the set $\theta_p \in \{0, \pi/2, \pi, 3\pi/2\}$. The search for the optimum subblock phase factors is computationally intensive, but this complexity can be reduced with adaptive PTS [28] or sphere decoding [32]. In addition, PTS requires to transmit $(P-1)\log_2 W$ bits per OFDM symbol as explicit side information, which can be used to recover the original data at the receiver. Techniques to avoid side information are proposed in [26], [29], and [31].

As shown in [27], pseudo-random subblock partitioning was found to have the best PAPR reduction compared to contiguous and other non-contiguous subblocking schemes. It improves the auto-correlation function (ACF) properties of the PTS subblocks as it provides less correlated adjacent time samples compared with other partitioning schemes. PTS is quite effective at reducing the PAPR however the PAPR performance depends on W, the number of subblocks, P, and the method of subblock partitioning. If the number of subblocks, P, and/or the number of phase values, W, are increased, the PAPR capability is

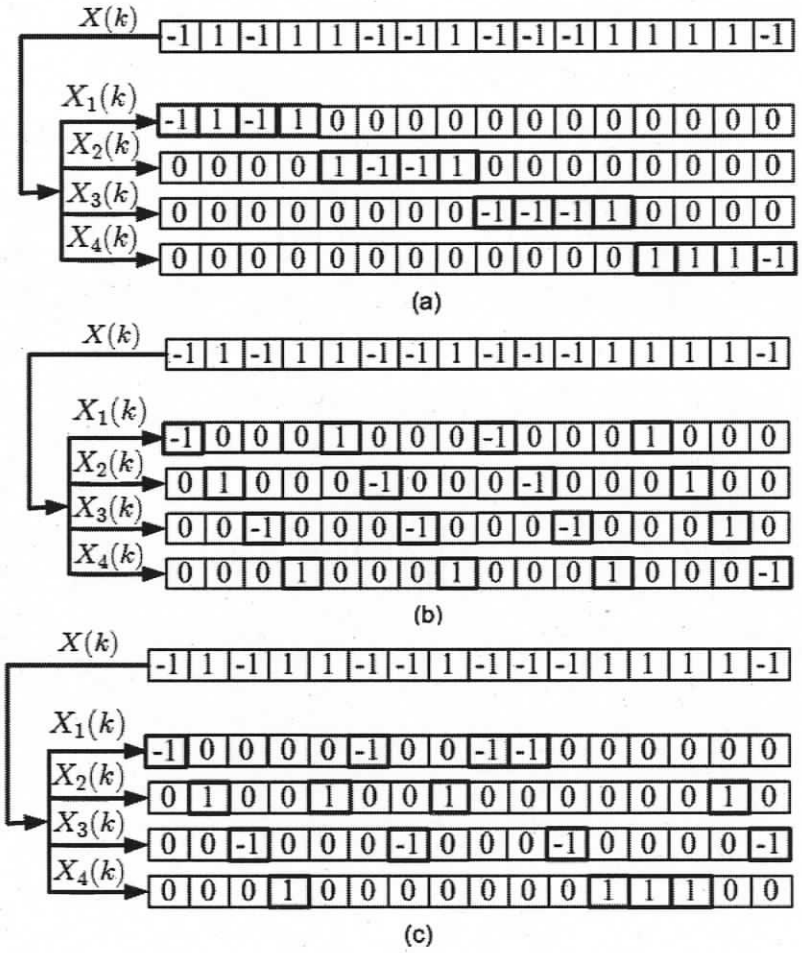

Figure 3.6. *Example of subblock partitioning for PAPR reduction in an OFDM system with* $N = 16$ *subcarriers and* $P = 4$*: (a) adjacent (b) equally spaced (c) random.*

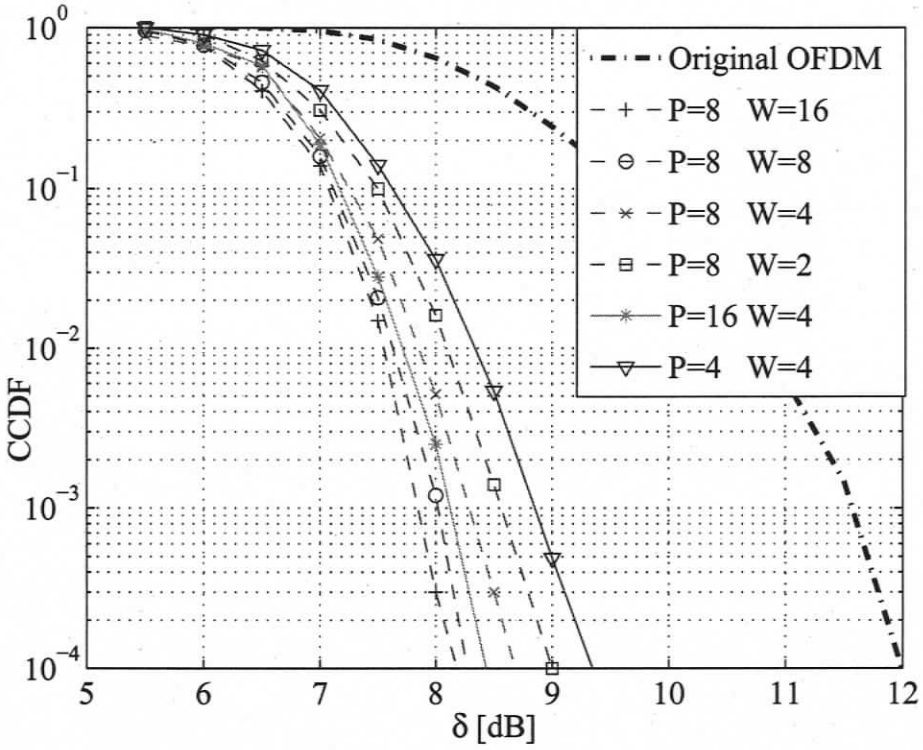

Figure 3.7. *CCDF of the OFDM signal for various P and W with $N = 256$ and pseudo random subblocking.*

improved. This is shown in Figure 3.7 for $N = 256$. The values $P = 8$ and $W = 4$ provide the best tradeoff in terms of search complexity and PAPR reduction. The phase values were randomly chosen from the set $\theta_p \in \{0, \pi/2, \pi, 3\pi/2\}$.

According to (3.6), the number of IDFT$_{N\times N}$ transforms which have to be computed is P, which is typically in the range 2 to 16. Thus the resulting computational complexity can be high, particularly when N is large. One of contributions focuses on the computational complexity of the multiple IFFTs. This will be discussed in Chapter 5.

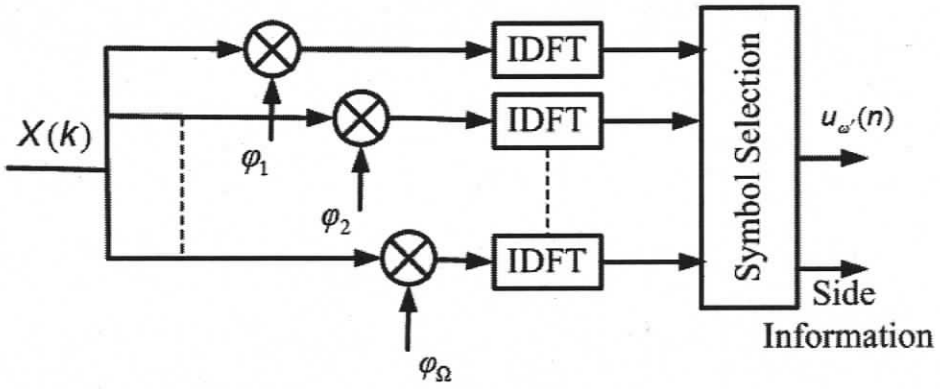

Figure 3.8. *Block diagram for the selective mapping PAPR reduction technique.*

3.2.4 Selective mapping (SLM)

A simple approach to generate different mappings for the same OFDM symbol is to phase rotating the frequency domain signal. This technique was proposed in [33] and [34] where it is called selective/selected mapping (SLM). Similar ideas can be also found in [35] and [36]. In fact, the idea of SLM is similar to PTS, but SLM phase rotates each subcarrier individually, while blocks of subcarriers are rotated in PTS. With SLM, multiple sequences are generated by multiplying independent phase sequences with the original data and the sequence with the lowest PAPR is chosen for transmission (see Figure 3.8). Consider a phase rotated version of $X(k)$ given by

$$U_\omega(k) = X(k) \bullet e^{j\phi_\omega(k)} \tag{3.8}$$

where $\bullet$ represents element-wise multiplication and $\phi_\omega(k)$ represents the kth of the phase sequence ϕ_ω . The time-domain OFDM signal $u_\omega(n)$ is obtained using the IDFT of $U_\omega(k)$ according to (2.6). Hence, all of the candidate symbols carry the same information $X(k)$. In SLM, the lowest PAPR signal $u_{\omega'}(n)$ is chosen for transmission from the Ω candidate OFDM signals, including the original $x(n)$, i.e.

$$\omega' = \arg \min_{1 \le \omega \le \Omega} PAPR[u_\omega(n)] . \tag{3.9}$$

To determine the selected sequence ω' at the receiver, $\log_2 \Omega$ bits of side information must be sent along with the data where Ω is the number of SLM sequences. Techniques to eliminate the side information are considered in [26] and [38]. $X(k)$ is recovered at the receiver using the DFT of the transmitted signal $u_{\omega'}(n)$

$$\begin{aligned} X(k) &= DFT\,[u_{\omega'}(n)] \bullet e^{-j\phi_{\omega'}(k)} \\ &= U_{\omega'}(k) \bullet e^{-j\phi_{\omega'}(k)} \\ &= X(k) \bullet e^{j\phi_{\omega'}(k)} \bullet e^{-j\phi_{\omega'}(k)} \\ &= X(k). \end{aligned} \tag{3.10}$$

To have a good PAPR reduction, the SLM technique should generate independent phase mappings. Intuitively, the mapped samples cannot be completely independent as they are generated using the same original data $X(k)$. It was shown in [40] that the phase mappings of a discrete-time domain sample $x(n)$ can be approximately independent. Further, different phase sequences for SLM were compared in [41] to determine the best type of phase sequences which minimizes PAPR. It was determined that using the randomly chosen phase sequences provides better PAPR reduction than other sequences such as complementary Golay, and Walsh-Hadamard sequences.

Figure 3.9 is a plot of the CCDF versus PAPR for SLM with various numbers of randomly chosen phase sequences $\phi_\omega(k)$ from the set $\{0, \pi\}$ with $N = 256$ and $J = 4$. From this plot, we can see that larger PAPR reductions are achieved as the number of SLM sequences Ω is increased. In addition, similar to PTS, SLM requires Ω IDFTs to obtain the sequences $u_\omega(n)$. As consequence, significant computational complexity is required for typical values of Ω, between 2 and 16. Complexity reductions can be made by implementing the proposed IFFT-based SLM technique that will be described in Chapter 5.

3.2.5 Tone reservation

The basic idea of tone reservation (TR) [42]-[47] is to reserve a set of subcarriers specially designed for peak-reduction. Among the distortionless methods for PAPR reduction, TR

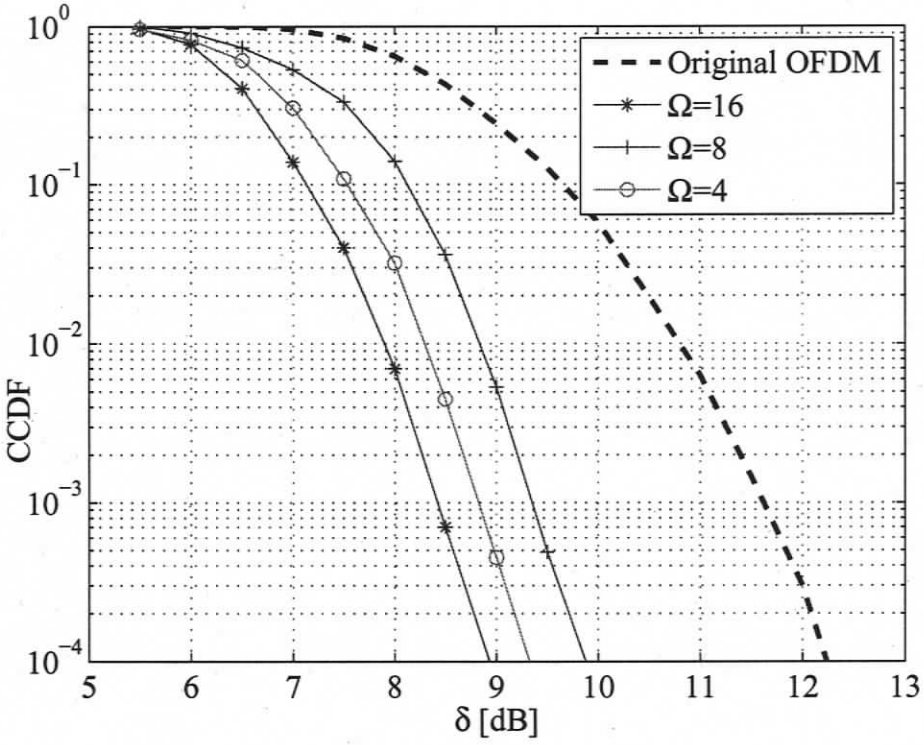

Figure 3.9. *PAPR CCDF of SLM for various* Ω *with* $N = 256$ *and* $J = 4$.

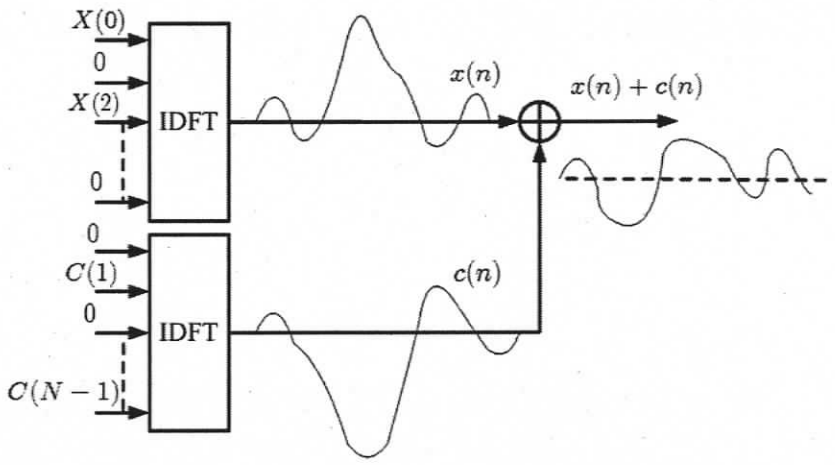

Figure 3.10. *Block diagram for the tone reservation PAPR reduction technique.*

can provide a large reduction in PAPR without requiring the transmission of side information. It is particularly appropriate when there is a large number of subcarriers.

To generate the time-domain peak reduction signal $\mathbf{c}$, a small subset of subcarriers are used. Then, this signal is added to the symbol $\mathbf{x}$ so that the PAPR for $\mathbf{x}+\mathbf{c}$ is defined as

$$\text{PAPR}(\mathbf{x}+\mathbf{c}) = \frac{\|\mathbf{x}+\mathbf{c}\|_\infty^2}{E\left[\|\mathbf{x}\|_2^2\right]/N}. \tag{3.11}$$

$\|\mathbf{x}+\mathbf{c}\|$ denotes the ∞-norm of the vector $\mathbf{x}+\mathbf{c}$ which is the maximum of the absolute values of its components and $\|\mathbf{x}\|$ denotes the 2-norm of the vector $\mathbf{x}$. The goal is to minimize the peak power of the signal $\mathbf{x}+\mathbf{c}$. A block diagram of the implementation of TR is illustrated in Figure 3.10. The optimal TR peak reduction signal $\mathbf{c}$ is formulated as the optimization problem [42]

$$\min_{\mathbf{c}} \|\mathbf{x}+\mathbf{c}\|_\infty = \min_{\mathbf{C}} \|\mathbf{x}+Q\mathbf{C}\|_\infty . \tag{3.12}$$

Where $\mathbf{C} = \text{DFT}(\mathbf{c})$.

In the case of real-baseband systems, the input signal to the IDFT $\mathbf{X}$ is required to be conjugate symmetric [42] to generate the real-valued OFDM signal $\mathbf{x}$. If the symbol $\mathbf{x}$ is complex valued, then the multicarrier system is a passband systems. The optimal

adjustment of the reserved tone values can be formulated as a quadratically constrained quadratic program (QCQP) for complex multicarrier signals, and a linear program (LP) for real multicarrier signals [42].

3.2.5.1 QCQP method for passband transmission

Let $\Lambda = [\lambda_1, \lambda_2, \ldots, \lambda_L]$ denote the subset of peak reduction tones (PRTs) used to generate $\mathbf{c}$ where the index set has the structure $0 \leq \lambda_1 < \ldots < \lambda_l \ldots < \lambda_L$, and $L << N$ is the number of PRTs. Then, the components $X(k)$ for $k \in \Lambda$ are set to zero and the components $C(k)$ are nonzero only if $k \in \Lambda$. Let $\widehat{C}$ be the nonzero values of C, i.e., $\widehat{\mathbf{C}} = [C(\lambda_1), C(\lambda_2), \ldots, C(\lambda_l), \ldots, C(\lambda_L)]^T$ and $\widehat{Q} = [q(\lambda_1), q(\lambda_2), \ldots, q(\lambda_l), \ldots, q(\lambda_L)]$ represents the reduced IDFT matrix Q (submatrices) containing only the columns which correspond to the reserved tones $\Lambda = [\lambda_1, \lambda_2, \ldots, \lambda_l, \ldots, \lambda_L]$. From (2.8), we then have that $\mathbf{c} = Q\mathbf{C} = \widehat{Q}\widehat{\mathbf{C}}$. Therefore, the optimization problem in (3.12) turns into

$$\min_{\widehat{\mathbf{C}}} \left\| \mathbf{x} + \widehat{Q}\widehat{\mathbf{C}} \right\|_{\infty}. \tag{3.13}$$

Let $\widehat{q}^{row}(n)$ denote the $n-th$ row of $\widehat{Q}$. Then, (3.13) can be written as

$$\min_{\widehat{\mathbf{C}}} \tau \tag{3.14}$$

$$\text{subject to :} \quad \begin{aligned} &\left| x(0) + \widehat{q}^{row}(0)\widehat{\mathbf{C}} \right|^2 \leq \tau \\ &\left| x(1) + \widehat{q}^{row}(1)\widehat{\mathbf{C}} \right|^2 \leq \tau \\ &\quad \vdots \\ &\left| x(n) + \widehat{q}^{row}(n)\widehat{\mathbf{C}} \right|^2 \leq \tau \\ &\quad \vdots \\ &\left| x(N-1) + \widehat{q}^{row}(N-1)\widehat{\mathbf{C}} \right|^2 \leq \tau \end{aligned}.$$

As shown in [42], this is a convex problem with linear constraints, while minimizing the constraints over an intersection of quadratic constraints on the variables $\widehat{\mathbf{C}}$, i.e. this is a QCQP problem.

3.2.5.2 LP-based technique for real-baseband transmission

For a real valued time-domain signal $\mathbf{x}+\mathbf{c}$, the conjugate symmetry conditions necessitates that the elements of $\mathbf{C}$ should have $C(k) = [C(N-k)]^*$ with $C(0)$ and $C(N/2)$ real valued. This requires that $\lambda_l \in \Lambda$ and $N - \lambda_l \in \Lambda$, i.e. $\mathbf{c}$ is real valued if the PRT index set has the structure

$$\Lambda = \left[\lambda_1, \ldots, \lambda_l, \ldots, \lambda_{L/2}, N-\lambda_{L/2}, \ldots, N-\lambda_l, \ldots, N-\lambda_1\right]. \tag{3.15}$$

To simplify the notation, the cases where k is equal to 0 and $N/2$ will be excluded [42]. We also have $\mathbf{c} = Q\mathbf{C} = \bar{Q}\bar{\mathbf{C}}$ using (2.8)

$$\bar{\mathbf{C}} = \left[C_R(\lambda_1), C_R(\lambda_2), \ldots, C_R(\lambda_{L/2}), C_I(\lambda_1), C_I(\lambda_2), \ldots, C_I(\lambda_{L/2})\right]^T \tag{3.16}$$

where $C_R(k) = \text{real}[C(k)]$ and $C_I(k) = \text{imag}[C(k)]$. The matrix is defined as $\bar{Q} = [\bar{q}(0)^{row}, \bar{q}(1)^{row}, \ldots, \bar{q}(N-1)^{row}]^T$ where

$$\bar{q}(k)^{row} = \left[\cos\left(\frac{2\pi\lambda_1 k}{N}\right), \cos\left(\frac{2\pi\lambda_2 k}{N}\right), \ldots, \cos\left(\frac{2\pi\lambda_{L/2} k}{N}\right), -\sin\left(\frac{2\pi\lambda_1 k}{N}\right), -\sin\left(\frac{2\pi\lambda_2 k}{N}\right), \ldots, -\sin\left(\frac{2\pi\lambda_{L/2} k}{N}\right)\right]^T \tag{3.17}$$

Considering (3.13), for the real-baseband case, the optimization problem is

$$\min_{\bar{\mathbf{C}}} \left\|\mathbf{x} + \bar{Q}\bar{\mathbf{C}}\right\|_\infty \tag{3.18}$$

or

$$\begin{aligned} &\min_{\bar{\mathbf{C}}} \tau \\ &\text{subject to : } \left|x(n) + \bar{q}^{row}(k)\bar{\mathbf{C}}\right| \le \tau. \end{aligned} \tag{3.19}$$

Equation (3.19) can be written in vector form as

$$\begin{aligned} &\min_{\bar{\mathbf{C}}} \tau \\ &\text{subject to : } \quad \mathbf{x} + \bar{Q}\bar{\mathbf{C}} \le \tau e, \\ &\qquad\qquad\quad \mathbf{x} + \bar{Q}\bar{\mathbf{C}} \ge -\tau e, \end{aligned} \tag{3.20}$$

where $I = [1\ 1 \ldots 1]^T \in \kappa^N$ is the all ones vector. Finally, the QCQP is reduced to the LP [42] as

$$\min_{\bar{\mathbf{C}}} \tau \tag{3.21}$$

$$\text{subject to : } \begin{bmatrix} \bar{Q} & I \\ -\bar{Q} & -I \end{bmatrix} \begin{bmatrix} \bar{\mathbf{C}} \\ \tau \end{bmatrix} \leq \begin{bmatrix} -\mathbf{x} \\ \mathbf{x} \end{bmatrix}.$$

This LP has $2L + 1$ unknowns $\{\text{real}(\bar{\mathbf{C}}), \text{imag}(\bar{\mathbf{C}}), t\}$ and $2N$ inequalities. Using an FFT algorithm, this LP can be solved with complexity $O(N \log N)$.

Figure 3.11 plots the PAPR performance of the TR technique when subcarriers are randomly and consecutively reserved. As shown in Figure 3.11, the optimal solution can approximately achieve a PAPR reduction of 6 to 8 dB when $L/N = 6.3\%$ to $L/N = 12.5\%$, respectively with randomly reserved subcarriers. The PAPR reduction is reduced to 3 and 5 dB with $L/N = 6.3\%$ and $L/N = 12.5\%$ conscutively chosen subcarriers. It has been also shown in [42] that randomly chosen reserved tones provide a better PAPR reduction than equally space and contiguous tones.

To reduce the computational complexity, suboptimal iterative algorithms such as gradient and controlled clipping have been proposed. They have less complexity and PAPR reduction compared to the optimal solution above for generating peak reduction signals.

3.2.5.3 The suboptimal iterative algorithms

As an approximate solution to (3.12), two suboptimal iterative algorithms were introduced in [42]. The first algorithm, called the gradient algorithm, uses a mean square error (MSE) criteria to obtain a low computational complexity algorithm. With similar computational complexity, the controlled clipper algorithm also provides an approximation to the optimal **c**.

Gradient Algorithm: The gradient algorithm proposed in [42]-[44] computes the signal **c** using the gradient of the mean square of the transmitter distortion function. If we consider large value ϵ in Equation (2.17), the SSPA model approximates the soft limiter (SL)

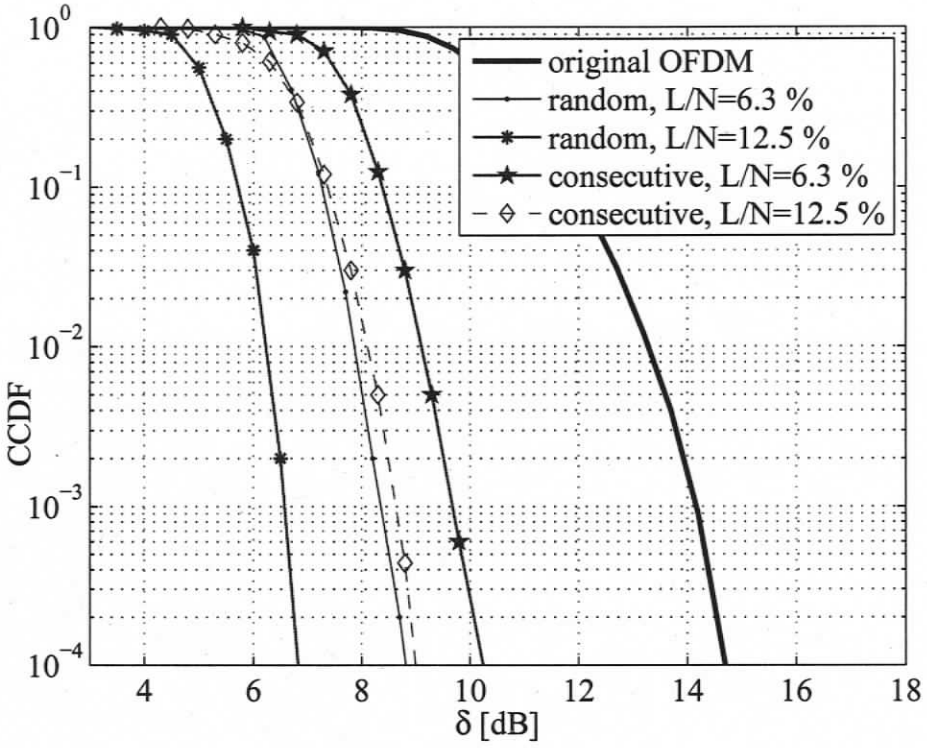

Figure 3.11. *Tone reservation performance comparison using the algorithm in [42] with randomly and consecutively selected* Λ, $N = 512$, *and* $L/N = 6.3\%, 12.5\%$ *for a passband multicarrier system.*

characteristics [42], i.e., the AM/AM nonlinear component can be written as

$$g(\mathbf{x}) = \begin{cases} \mathbf{x}, & |\mathbf{x}| \leq A \\ Ae^{j\angle \mathbf{x}}, & |\mathbf{x}| > A \end{cases}. \tag{3.22}$$

Similar to (2.17), the AM/PM component is zero. Hence, the transmitter distortion function is defined as $\mathbf{x} - g(\mathbf{x})$. To reduce PAPR, we need to minimizing the mean square of the transmitter distortion function [42]

$$\min_{\widehat{\mathbf{c}}} \left\| \mathbf{x} + \widehat{Q}\widehat{\mathbf{C}} - g(\mathbf{x} + \widehat{Q}\widehat{\mathbf{C}}) \right\|_2^2. \tag{3.23}$$

Using the gradient of (3.23) with respect to $\widehat{\mathbf{C}}$ in the iterative gradient algorithm, and taking the IDFT over the vectors with nonzero elements in Λ, the signal $\mathbf{c}$ at the βth iteration is given by [42]

$$\mathbf{c}^{(\beta+1)} = \mathbf{c}^{(\beta)} - \mu \sum_{|x(n)+c(n)^{(\beta)}|>A} \left(x(n) + c(n)^{(\beta)} - Ae^{\angle(x(n)+c(n)^{(\beta)})} \right) \widehat{Q}(\widehat{q}^{row}(n))^*. \tag{3.24}$$

where $\widehat{q}^{row}(n)$ denotes the n-th row of $\widehat{Q}$. With $\breve{\mathbf{x}} = \mathbf{x} + \mathbf{c}^{(\beta)}$, the iterative gradient algorithm in (3.24) can be expressed as

$$\breve{\mathbf{x}}^{(\beta+1)} = \breve{\mathbf{x}}^{(\beta)} - \mu \sum_{|\breve{x}(n)^{(\beta)}|>A} \left(\breve{x}(n)^{(\beta)} - Ae^{\angle(\breve{x}(n)^{(\beta)})} \right) \mathbf{e}_n^{\|2} \tag{3.25}$$

where $\mathbf{e}_n^{\|2} = \widehat{Q}(\breve{q}^{row}(n))^*$.

As stated in [42], only the largest value $|\breve{x}(n)^{(\beta)}|$ is considered to reduce the number of computations per iteration. The term $\mathbf{e}_n^{\|2}$, called the kernel, determines the convergence of the algorithm as it depends on the PRT locations (Λ). Because of the circular shift property of the DFT, the kernels $\mathbf{e}_n^{\|2}$, for $n = 0, 1, \ldots, N-1$, are

$$e_{n_\beta}^{\|2}[n] = e_{n_0}^{\|2}[(n - n_\beta)_N]. \tag{3.26}$$

Thus all kernels can be obtained using circular shifts of the kernel $e_0^{\|2}[n]$, denoted as $e^{\|2}[n]$ for simplicity.

Considering the mean square error (MSE) approach in [42], $e^{\|2}[n]$ must be optimized over all possible reserved tones Λ, which is an NP-hard problem. In another word, a random search over all the possible sets will largley increase the complexity of tone reservation. As an alternative solution, $\bar{I}$ randomly generated sets $\Lambda^1, \Lambda^2, \ldots, \Lambda^{\bar{I}}$ can be considered and the best one selected. For each set Λ, the MSE kernel computation consists of the following steps [42]:

1. Set $i = 0$
2. Generate L random locations $\Lambda_{i+1} = [\lambda_1, \lambda_2, \ldots, \lambda_L]$ over the interval $(1, \ldots, N)$.
3. Set the frequency-domain kernel $E[k] = 1$ for $k \in \Lambda$, and $E[k] = 0$ for $k \notin \Lambda$.
4. Calculate $e[n] = \text{IFFT}(E[k])$. The value $e[0]$ is the maximum and is used to normalize $e(n)$ giving $e^*[n] = e[n]/e[0]$.
5. Calculate the secondary peak of $e^*[n]$ which is $\max\{|e^*[n]|\}$ for $n > 0$.
6. Set $i = i + 1$. If $i > \bar{I}$ quit, otherwise jump to Step 2.

We will discuss the choice of $\bar{I}$ in Chapter 5. The computational complexity is essentially determined by the IFFT operation in Step 4. Hence, the computational complexity of this algorithm is approximately $\bar{I}$ times the IFFT complexity for each $e[n]$ update, where each IFFT has complexity $O(N \log_r N)$.

Controlled Clipper: Similar to the iterative gradient-based algorithm, the controlled clipper algorithm iteratively computes

$$\bar{\mathbf{x}}^{(\beta+1)} = \bar{\mathbf{x}}^{\beta} + \mathbf{c}^{clip} \tag{3.27}$$

where $\bar{\mathbf{x}}$ is the time-domain vector of the peak reduced OFDM signal at the β-th iteration and $\bar{\mathbf{x}}^{(0)} = [x(0), x(1), \ldots, x(N-1)]$. $\mathbf{c}^{clip}$ is ideally a sum of delayed impulses scaled appropriately to cancel the peak of $\bar{\mathbf{x}}$ and reduce the symbol dynamic range to the interval $(-A, A)$, i.e., $\mathbf{c}^{clip} = -\sum_{|\bar{x}(n_\beta)|>A} \chi_\beta \Delta(n - n_\beta)$ where the χ_β are the clipping pulses at iteration β. In order to have an ideal impulse $\Delta(n - n_\beta)$, the frequency-domain signal $\mathbf{C}^{clip} = DFT(\mathbf{c}^{clip})$ must be reserved over all tones [42]. This is impossible as the number

of reserved tones L would be equal to the number of subcarriers N. Hence, a limited number of reserved tones is considered to approximate $\Delta(n-n_\beta)$ by a kernel pulse $e(n-n_\beta)$ i.e.

$$\mathbf{c}^{clip} = -\sum_{|\bar{x}_{n_\beta}|>A} \alpha_\beta e(n-n_\beta) \approx -\sum_{|\bar{x}(n_\beta)|>A} \beta_\beta \Delta(n-n_\beta) \tag{3.28}$$

where $\mathbf{e} = e(n) = [e_0, e_1, \ldots, e_{N-1}]$ are time-domain peak-reduction kernels.

As stated in [42], the kernel pulse $\mathbf{e} = e(n) = [e(0), e(1), \ldots, e(N-1)]$ which is circularly shifted by n_β to obtain $e(n-n_\beta)$ should satisfy $e(0) = 1$ with $[e(1), e(2), \ldots, e(N-1)]$ as small as possible. Since the elements $[e(1), e(2), \ldots, e(N-1)]$ cannot be zero, secondary peaks are unavoidable. These peaks increase the number of iterations (slow the convergence rate).

Figure 3.12 shows the performance of the gradient-based technique where $L/N = 6.3\%$ subcarriers are randomly reserved for $\beta = 40$, $A = 6$ dB, and $\bar{I} = 10$. In this case, the gradient algorithm achieves a PAPR reduction of 3 dB.

The above suboptimal algorithms present a tradeoff between computational complexity and PAPR reduction as their convergence is slow after several iterations. For the controlled clipping algorithm, a better tradeoff has been made in [48] by using the filtered clipper noise as the kernel signal, and adaptively scaling it to reduce the PAPR. However, the resulting complexity is still high since a number of FFT/IFFT operations are required during the iterative process.

Further, If the channel is not static, periodic updating Λ and $\mathbf{e}_n^{\|2}$ $(\mathbf{e})$ are required according to the coherence time of the channel. This can lead to an extremely high computational complexity to compute the peak reduction kernels. Hence, we consider efficient computation of the peak reduction kernels in Chapter 5.

Another drawback of the TR technique is that the data rate is necessarily decreased because L subcarriers are allocated for peak-reduction tons. This data rate loss may be reduced in static channel if some subcarriers are known to have a low signal to noise ratio (SNR) for data transmission. When the channel is not static, this can turn into an unac-

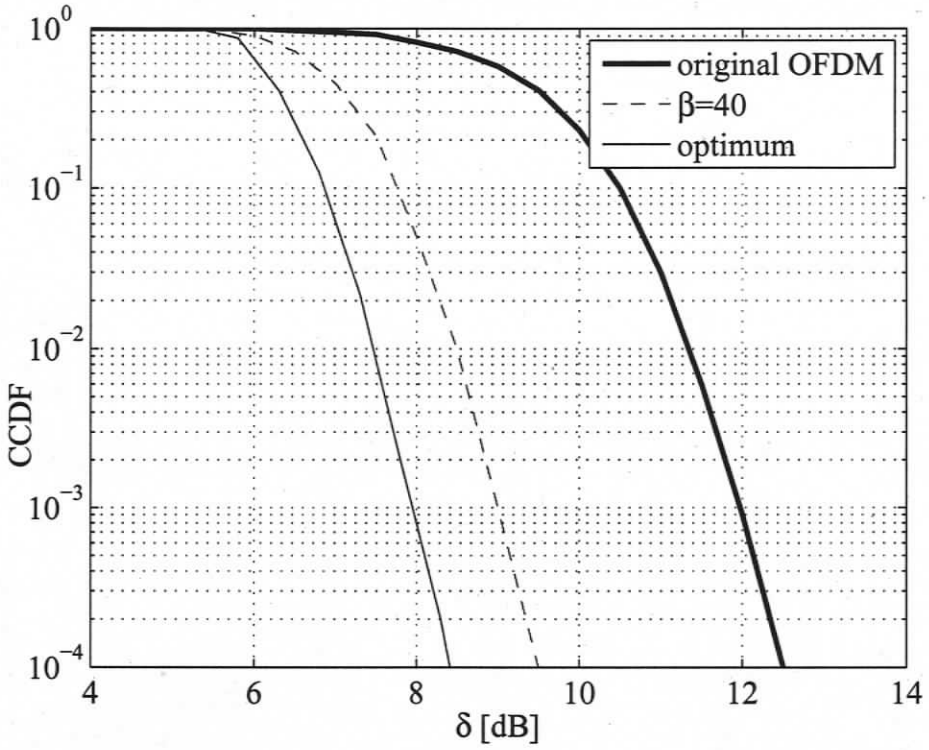

Figure 3.12. *PAPR performance using the using a gradient-based algorithm in [42] with randomly chosen subcarriers,* $L/N = 6.3\%$, $\beta = 40$, $A = 6dB$, *and* $\bar{I} = 10$.

ceptable amount of overhead, particularly for small values of N. However, if adaptive modulation is employed, the overhead can be reduced by employing peak-reduction symbols in tones where the SNR is too low for data transmission.

Chapter 4

Fast Fourier Transforms: Theory and Algorithms

This chapter provides the necessary theory and background of fast Fourier transform (FFT) or inverse fast Fourier transform (IFFTs) algorithms as they will be used as the basis for the IFFT-based PAPR reduction techniques in the next chapter. We focus on the FFT algorithm in detail, as the IFFT can be computed by taking the complex conjugate of the input and output sequences while using the same FFT parameters.

After an overview of the FFT algorithms, a new recursive expression is derived which describes the FFT algorithms in terms of stages. This leads to the new concept of using the identical discrete Fourier Transforms (DFTs) at the FFT stags. This approach has several benefits. The PAPR reduction techniques can be described and analyzed based on the actual implementations of FFT algorithms rather than using only a simple DFT transform matrix. The effects of the intermediate signals on the time domain OFDM signals can be analyzed in terms of PAPR reduction capabilities. Such a structure allows for the analysis of the computational complexity of each FFT stage.

Moreover, a new recursive expression for the FFT algorithms is developed as a alternative representation of the identical DFTs at each FFT stage. This form is quite useful for dealing with optimal and suboptimal solutions related to PAPR reduction techniques.

4.1 The Fast Fourier Transform (FFT)

The fast Fourier transform (FFT) is a class of efficient algorithms for computing the DFT. It provides the same results as the computation of the direct form of the DFT using (2.9). It is based on the fast DFT algorithm proposed by Cooley and Tukey [84]. Before then, every DFT was computed using a direct algorithm with complexity $O(N^2)$[1]. Since the Cooley and Tukey's algorithm was introduced, the applications of the DFT have increased enormously due to efficient implementations of new algorithms.

To derive a common form of the FFT, let first have the simplest derivation for the FFT. Consider (2.9) and (2.6) for the DFT and IDFT computations, respectively, as

$$X(k) = \sum_{n=0}^{N-1} x(n) T_N^{nk} \quad 0 \leq n \leq N-1, \;\; 0 \leq k \leq N-1, \tag{4.1}$$

and

$$x(n) = \frac{1}{N} \sum_{k=0}^{N-1} X(k) T_N^{-nk} \quad 0 \leq n \leq N-1, \;\; 0 \leq k \leq N-1, \tag{4.2}$$

where $T_N = e^{-j2\pi/N}$. Equation (4.1) gives the the N outputs of the DFT where each output is the summation over all N terms $x(n)T_N^k$. This requires $N(N-1)$ complex additions and N^2 complex multiplications with the precomputed constant T_N^k. As a consequence, DFT computation requires approximately $O(N^2)$ operations. Based on (4.2), the IDFT has the same number of operations as the DFT computation. This is because it differs only by a minus sign in the twiddle factors and a multiplication by the constant $1/N$.

The simplest FFT algorithm can be derived where $N = 2^m$ and m is a positive integer [81]. Thus, the sequence $x(n)$ in (4.1) can be divided into two sequences of length $N/2$ where one sequence has even index $2m$ and the other one has the odd index $2m + 1$.

[1] $O(N)$ represents on the order of N.

Equation (4.1) can then be written based on sequences $x(2m)$ and $x(2m+1)$ as

$$\begin{aligned} X(k) &= \sum_{m=0}^{N/2-1} x(2m) T_N^{2mk} + \sum_{m=0}^{N/2-1} x(2m+1) T_N^{(2m+1)k} \\ &= \sum_{m=0}^{N/2-1} x(2m) \left(T_N^2\right)^{mk} + \sum_{m=0}^{N/2-1} x(2m+1) \left(T_N^2\right)^{mk} T_N^k. \end{aligned} \tag{4.3}$$

Since

$$\begin{aligned} T_N^2 &= \left(e^{j2\pi/N}\right)^2 \\ &= e^{j2\pi 2/N} \\ &= e^{j2\pi/(N/2)} \\ &= T_{N/2} \end{aligned} \tag{4.4}$$

Equation (4.3) is the given by

$$X(k) = \underbrace{\sum_{m=0}^{N/2-1} x(2m) T_{N/2}^{mk}}_{X^{\text{even}}(k)} + T_N^k \underbrace{\sum_{m=0}^{N/2-1} x(2m+1) T_{N/2}^{mk}}_{X^{\text{odd}}(k)}. \tag{4.5}$$

If we call the two sums above $X^{\text{even}}(k)$ and $X^{\text{odd}}(k)$, respectively, then we have

$$X(k) = X^{\text{even}}(k) + T_N^k X^{\text{odd}}(k) \tag{4.6}$$

where $X^{\text{even}}(k)$ and $X^{\text{odd}}(k)$ for $k = 0, 1, \ldots, N/2$ are $N/2$-point DFTs. Since $X(k)$ is periodic in N, i.e., $X(k) = X(k + Nm^{prime})$ for any integer m and

$$\begin{aligned} T_N^{k+N/2} &= T_N^k T_N^{N/2} \\ &= T_N^k e^{j\pi} \\ &= -T_N^k, \end{aligned} \tag{4.7}$$

and

$$\begin{aligned} T_{N/2}^{k+N/2} &= T_{N/2}^k T_{N/2}^{N/2} \\ &= T_N^k e^{2j\pi} \\ &= T_N^k. \end{aligned} \tag{4.8}$$

We can also write

$$X(k+N/2) = X^{even}(k) - T_N^k X^{odd}(k). \tag{4.9}$$

Hence, we can compute an N-point DFT by dividing it into two parts. the $N/2$-point DFTs are calculated for $k = 0, 1, \ldots, N/2-1$ and then re-used for $k = N/2, N/2+1, \ldots, N-1$. To restate this key point in another way, the first half of $X(k)$ for $k = 0, 1, \ldots, N/2-1$ can be computed from (4.6), and the second half of $X(k)$ can be computed by reusing the same terms differently as shown in (4.9). The N terms of $X(k)$ can then be calculated with $O(N/2)^2 + O(N/2)^2 = O(N^2/2)$ operations.

As N is power of 2, $X^{\text{even}}(k)$ and $X^{\text{odd}}(k)$ for $N > 2$ can further be divided into even and odd sequences, and computed using $(N/2)/2 = N/4$-point DFTs. This recursive procedure can be used until 2-point DFTs are obtained as 2-point DFTs are trivial to compute. Figure 4.1 shows the dataflow diagram for $N = 16$. Note that $T_{N/2}^k = T_N^{2k}$, $T_{N/4}^k = T_N^{4k}$, and $T_{N/8}^k = T_N^{8k}$, This recursive procedure can be applied $\log_2(N-1)$ times, producing $\log_2 N$ stages i.e. $m = 1, 2, \ldots, \log_2 N$.

Before describing the types of FFTs, we introduce some terminology. This FFT belongs to the class of FFT algorithms called radix-2 FFT as each stage splits DFT into two smaller DFTs. This is a regular radix algorithm as each stage uses the same radix-2.

In order to show the computations in (4.6) and (4.9), a computational building block called a butterfly is used. This simplifies the FFT diagrams and make them easier to analyze. Figure 4.2 shows a signal flow representation of a radix-2 decimation in time (DIT) butterfly which is used throughout this thesis.

Next, we introduce the most common types of FFTs and their most important features, their flow graphs and butterfly structures, using example.

4.2 The Common FFT Algorithms

The most popular class of FFT algorithms is the Cooley-Tukey FFTs [84]. The idea behind these FFT algorithms is the divide and conquer approach, to break up recursively the orig-

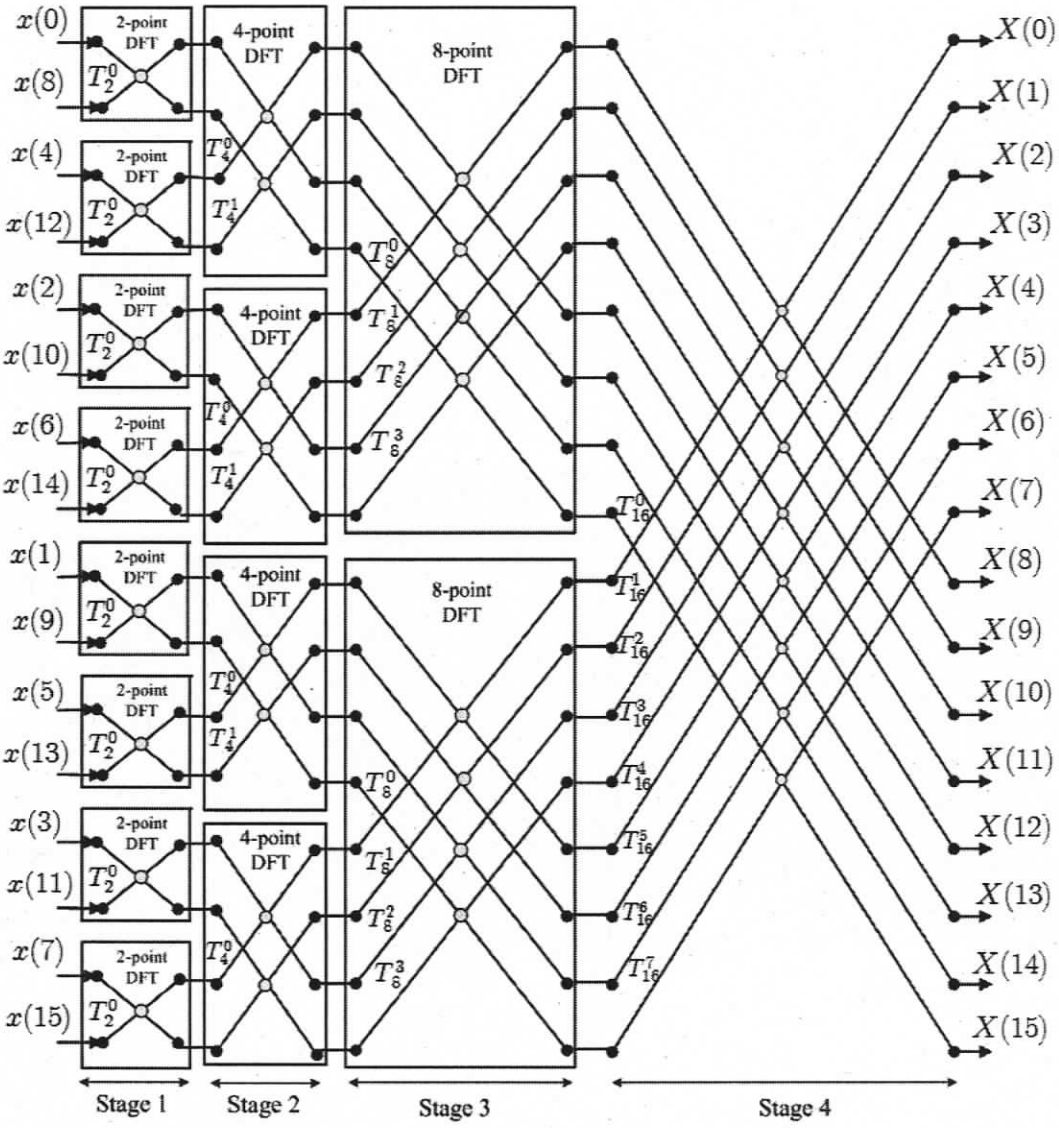

Figure 4.1. *Signal flow graph of a 16-point FFT using $N/2$-point DFTs.*

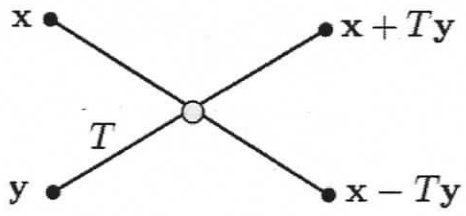

Figure 4.2. *Radix-2 DIT FFT butterfly diagram.*

inal N point sequence into smaller sequences N_1 and N_2 where $N = N_1 N_2$. In fact, they represent the DFT of size N in terms of smaller DFTs of sizes N_1 and N_2. They are also called common factor FFTs since N_1 and N_2 have a common factor, i.e., there is an integer other than unity which evenly divides N_1 and N_2.

These algorithms use

$$n = N_2 n_1 + n_2 \quad n_1 = 0, 1, \ldots, N_1 - 1 \quad n_2 = 0, 1, \ldots, N_2 - 1 \tag{4.10}$$

for the mapping of the one-dimensional inputs $x(n)$ into the two-dimensional array $x(n_1, n_2)$ and

$$k = k_1 + N_1 k_2 \tag{4.11}$$

for the mapping of the DFT outputs $X(k)$ into the array $X(k_1, k_2)$, where $X(k_1, k_2)$ is the two-dimensional map of $X(k)$. Equation (4.1) can then be written as

$$X(k_1 + N_1 k_2) = \sum_{n_1=0}^{N_1-1} \sum_{n_2=0}^{N_2-1} x(N_2 n_1 + n_2) T_N^{N_2 n_1 k_1} T_N^{N_2 n_1 N_1 k_2} T_N^{n_2 k_1} T_N^{n_2 N_1 k_2} \tag{4.12}$$

The term $T_N^{N_2 n_1 N_1 k_2}$=1 for any values of n_1 and k_2 since

$$\begin{aligned} T_N^{N_2 n_1 N_1 k_2} &= T_N^{N n_1 k_2} \\ &= \left(e^{-j2\pi}\right)^{n_1 k_2} \\ &= 1. \end{aligned} \tag{4.13}$$

Further, $T_N^{N_2 n_1 k_1}$ can be further simplified as

$$\begin{aligned} T_N^{N_2 n_1 k_1} &= e^{-j2\pi \frac{N_2 n_1 k_1}{N}} \\ &= e^{-j2\pi \frac{N_2 n_1 k_1}{N_1 N_2}} \\ &= T_{N_1}^{n_1 k_1} \end{aligned} \tag{4.14}$$

and similarly $T_N^{n_2 N_1 k_2} = T_{N_2}^{n_2 k_2}$. With these simplifications, (4.12) becomes

$$\begin{aligned} X(k_1 + N_1 k_2) &= \sum_{n_1=0}^{N_1-1} \sum_{n_2=0}^{N_2-1} x(N_2 n_1 + n_2) T_{N_1}^{n_1 k_1} T_N^{n_2 k_1} T_{N_2}^{n_2 k_2} \\ &= \sum_{n_1=0}^{N_1-1} \left(\sum_{n_2=0}^{N_2-1} \left[x(N_2 n_1 + n_2) T_{N_2}^{n_2 k_2} \right] T_N^{n_2 k_1} \right) T_{N_1}^{n_1 k_1} \end{aligned} \tag{4.15}$$

or

$$X(k_1 + N_1 k_2) = \underbrace{\sum_{n_1=0}^{N_1-1} \left(\underbrace{\sum_{n_2=0}^{N_2-1} \left[x(N_2 n_1 + n_2) T_{N_2}^{n_2 k_2} \right]}_{N_2-\text{point DFT}} \underbrace{T_N^{n_2 k_1}}_{\text{twiddle factor}} \right) T_{N_1}^{n_1 k_1}}_{N_1-\text{point DFT}} \tag{4.16}$$

The reformulation in (4.16) results in the following steps:

1. Perform N_1 DFTs of size N_2.
2. Multiply the $N = N_1 \times N_2$ intermediate values by the twiddle factors $T_N^{n_2 k_1}$.
3. Perform N_2 DFTs of size N_1.

4.2.1 Radix-r FFT algorithms

Consider the above common factor FFT algorithms where $N = r^m$ (m is a positive integer), and the butterfly has the same structure in each stage. These are called *radix-r* FFT algorithms. A radix-r FFT has a radix-r butterfly structure and $\log_r N$ stages. when $N \neq r^m$, the choice of N determines that the FFT should be *mixed-radix*. Typically, radix-r algorithms are simpler to implement over mixed-radix algorithms due to regular structure of the butterflies at all stages, which simplifies the design.

Next, the most widely used common factor FFT algorithms; radix-r decimation in time (DIT) and decimation in frequency (DIF), are discussed.

4.2.1.1 Radix-r DIT and DIF algorithms

If the values of N_1 and N_2 are set to N/r and r, respectively, then (4.10) and (4.11) give

$$\begin{aligned} n &= \cdot\ rn_1 + n_2 \\ k &= k_1 + \frac{N}{r}k_2. \end{aligned} \tag{4.17}$$

Substituting (4.17) into (4.15)

$$X(k_1 + k_2 N/r) = \sum_{n_1=0}^{\frac{N}{r}-1} \left(\sum_{n_2=0}^{r-1} \left[x(rn_1 + n_2) T_r^{n_2 k_2} \right] T_N^{n_2 k_1} \right) T_{N/r}^{n_1 k_1}. \tag{4.18}$$

or

$$X(k + k_0 N/r) = \sum_{n=0}^{\frac{N}{r}-1} \left(\sum_{i=0}^{r-1} x(rn + i) T_r^{ik_0} T_N^{ik} \right) T_{N/r}^{nk}. \tag{4.19}$$

where $k_0 = 0, 1, \ldots, r-1$, $k = 0, 1, \ldots, \frac{N}{r} - 1$, $n = 0, 1, \ldots, \frac{N}{r} - 1$, and $i = 0, 1, \ldots, r-1$. This is a recursive decomposition an N-point DFT into smaller N/r-point DFTs and converts the DFT computation to $r \times N/r$-point DFTs recurring through $m = \log_r N$ stages. This algorithm is known as radix-r *decimation in time (DIT)*. As an example, the flow diagram in Figure 4.1 shows the radix-2 DIT algorithm. The second class of common factor FFT algorithms is derived when $N_1 = r$ and $N_2 = N/r$. Similarly, inserting (4.10) and (4.11) with the new values N_1 and N_2 into (4.15) results in

$$X(k_1 + k_2 r) = \sum_{n_1=0}^{r-1} \sum_{n_2=0}^{\frac{N}{r}-1} x(\frac{N}{r} n_1 + n_2) T_{N/r}^{n_2 k_2} T_N^{n_2 k_1} T_r^{n_1 k_1} \tag{4.20}$$

or

$$X(rk + k_0) = \sum_{n=0}^{\frac{N}{r}-1} \left(\left(\sum_{i=0}^{r-1} x(n + i\frac{N}{r}) T_r^{ik_0} \right) T_N^{nk_0} \right) T_{N/r}^{nk}. \tag{4.21}$$

where $k_0 = 0, 1, \ldots, r-1$, $k = 0, 1, \ldots, \frac{N}{r} - 1$, $n = 0, 1, \ldots, \frac{N}{r} - 1$, and $i = 0, 1, \ldots, r-1$. This second radix-r FFT algorithm is known as *decimation in frequency (DIF)*. Figures 4.3

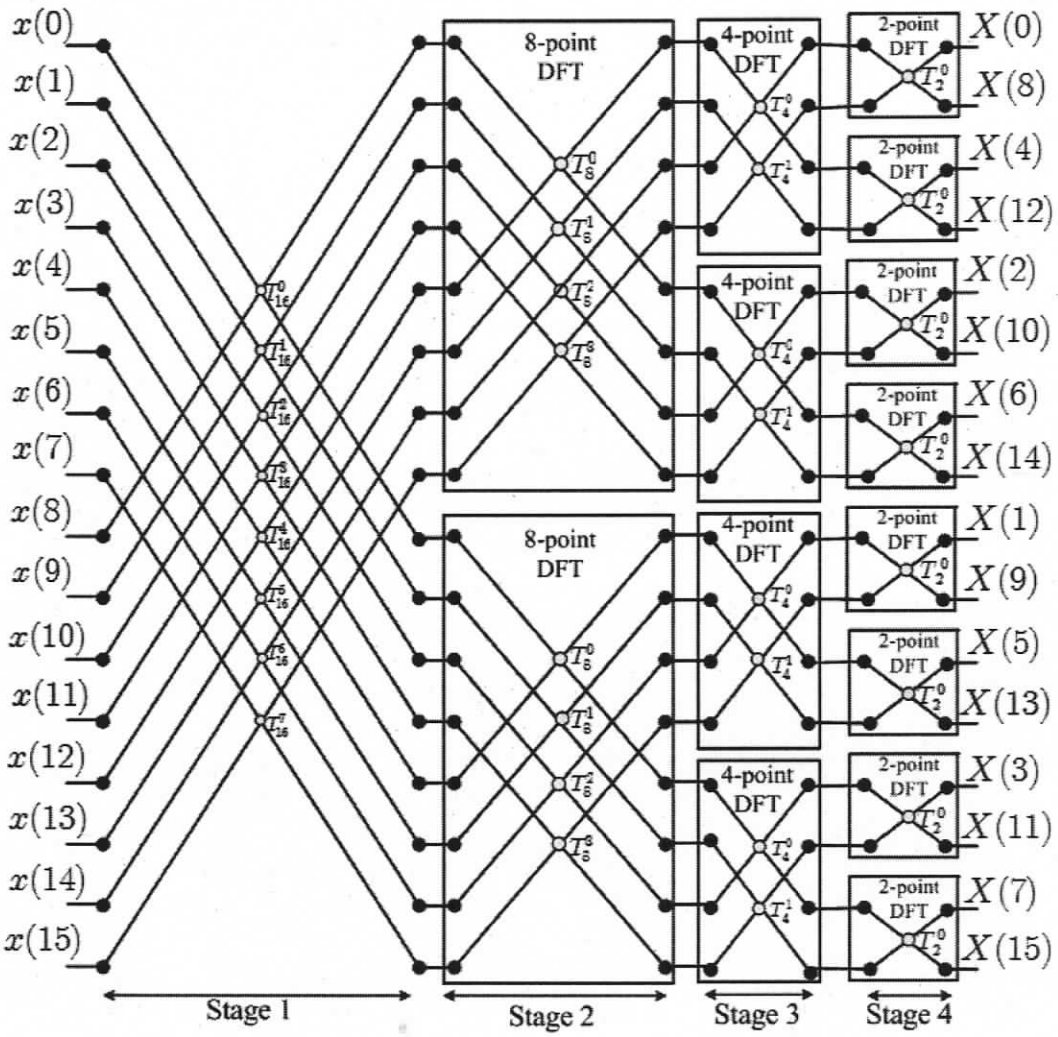

Figure 4.3. *Signal flow graph of a 16-point FFT using radix-2 DIF algorithm.*

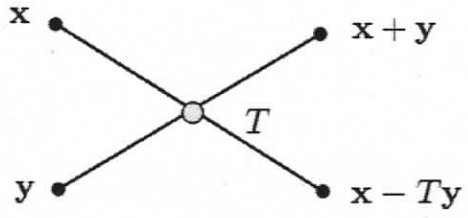

Figure 4.4. *Radix-2 DIF FFT butterfly diagram.*

and 4.4 illustrate the implementation of radix-2 for $N = 16$ and the DIF butterfly structure, respectively.

4.2.1.2 General FFT terms

Some of the terms discussed in last section and used in above example are now described in detail. It is assumed throughout this thesis that the input sequence $x(n)$ is in normal order, and the output $X(k)$ is in digit-reversed order in DIF (see Figure 4.3) and vice-versa for the DIT algorithm (see Figure 4.1).

Radix-r butterflies have r inputs and r outputs. They contain N/r butterflies per stage. Each stage is defined as a part of the FFT computation where N memory locations containing the inputs to butterfly are read, processed by a butterfly, and written back once. Therefore, the inputs and outputs to each stage are accessible in practical implementations. This indicates that the IFFT-based PAPR reduction techniques in Chapter 5 are practically implementable as they use inputs to each stage rather than using the frequency domain signal $X(k)$.

4.2.1.3 High radix FFT algorithms

For the high radix FFT algorithms, first consider the radix-4 common factor FFT algorithm with N is power of 4, i.e., $N = 4^m$. From (4.19) and (4.21) , the derivation of the DIT and DIF radix-4 algorithms is the same as for the radix-2 DIT and DIF algorithms. Figure 4.5 shows the signal flow graph of a 16-point FFT using a radix-4 DIF algorithm. Radix-4 algorithms requires less computational complexity than radix-2 algorithms because one radix-4 butterfly does the work of four radix-2 butterflies. As a consequence, the number of complex multiplications and stages are reduced.

The number of stages determines the number of access memory. Hence, it can be considered an indicator of the efficiency for a given IFFT/FFT size. Using higher radix can increase the performance of the FFT algorithms. For example, if the base butterfly structure that performs a 16 point complex FFT is radix-2, it requires 4 stages before the

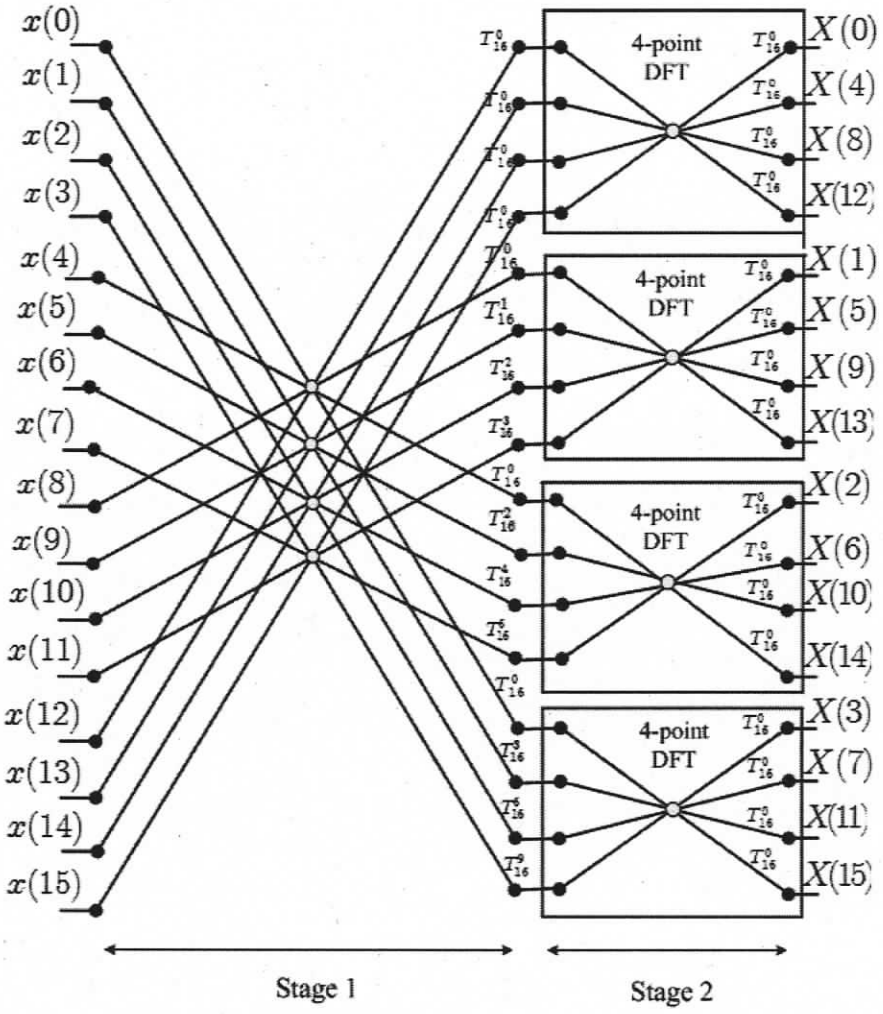

Figure 4.5. *Signal flow graph of a 16-point FFT using a radix-4 DIF algorithm.*

transformation is completed (see Figure 4.1). If we move to a radix-4 base structure for the FFT, only 2 stages are required instead of 4 (see Figure 4.5), therefore the overall processing should speed up. Taking this even further to a radix-8 or higher structure, the efficiencies start to become dramatic. On the negative side, these higher radices become more complex to implement. This is because they increase the circuit complexity. To simplify the implementation complexity of high radices, radix 2^2 was introduced in [85]. It's multiplicative complexity is similar to a radix-4 algorithm, but it retains the butterfly structure of a radix-2 algorithm. This leads to simple data paths and control flow and also the benefit of radix-4 with fewer multiplications. However, due to increasing the number of stages, the number of memory access would be increased. As consequence, we limit the value r to 4 in this thesis.

Since IFFT-based techniques are defined based on the inputs to the processing stages, the effects of higher radices on the IFFT-based techniques in terms of PAPR and computational complexity differs from the lower radix algorithms. This will be shown in Chapter 5.

4.2.2 Other FFT algorithms

There are other FFT algorithms which are commonly found in the literature. Prime factor FFTs [92] and [93] are a type of FFT algorithm where N_1 and N_2 have only the common factor unity. The advantage of these algorithms is that they have fewer multiplications compared to the common factor algorithms, but the mapping of the sequence $x(n)$ into $x(n_1, n_2)$ is complicated and requires significant computation [92]. The prime factor FFTs proposed in [93] have an efficient means of mapping $x(n)$ into $x(n_1, n_2)$. However the irregular and complex structure makes it very complicated to implement.

Another DFT algorithm which is discussed in [94] is the Goertzel DFT algorithm. This algorithm efficiently computes a subset of the N outputs. Nevertheless, this is not a typical FFT algorithm since it does not decrease the DFT computation from $O(N^2)$,

The split-radix FFT in [86]-[91] is a more efficient approach than standard common

factor radix-r FFTs. It is similar to a radix-r FFT, but has different radix stages. For example, the split-radix FFT algorithm recursively uses a DFT of length N in terms of one smaller DFT of length $N/2$ and two smaller DFTs of length $N/4$. This results in an efficient algorithm as the number of multiplications is less than radix-2 or radix-4 algorithms. However, its butterfly structure is more complex to implement. More details can be found in [89].

4.2.3 Radix-r FFT algorithms based on stages

As previously mentioned, this thesis is concerned with analyzing and quantifying the distortionless PAPR reduction techniques based on each FFT processing stage. Therefore, we derive a general expression for the common FFT algorithms where all elements are function of FFT stages. We first consider DIF derived from (4.21) and introduce the concept of identical DFTs at each particular FFT stage.

4.2.3.1 The identical DFTs

1) DIF algorithms: Let v denotes the number of stages where $v = 1, 2, \ldots, m$. The symbols and indices at stage v are represented by the notation $\widetilde{x}$ and $\widetilde{n}$ for an input x and time index n, respectively, and $\widetilde{k}$ for a frequency index k. Then, the FFT output $X(\widetilde{k})$ corresponds to the inputs $x(\widetilde{n})$ at stage v. Equation (4.21) represents the reduction of an $\frac{N}{r^v} - 1$-point DFT into smaller $r^v \frac{N}{r^v}$-point DFTs at stage $v = 1$. The block diagram of this decomposition is given in Figure 4.6. Further, there are $r^v \frac{N}{r^v}$-point DFTs at the output of stage $v = 1$ which become $r^{v-1} \frac{N}{r^{v-1}}$-point DFTs in the next stage $v = 2$. Since the FFT is a recursive algorithm, we extend these observations to stage v as follows:

1. There are $r^{v-1} \frac{N}{r^{v-1}}$-point DFTs at stage v. Figure 4.6 shows one identical $\frac{N}{r^{v-1}}$-point DFTs. We introduce the variable, η to indicate a given $\frac{N}{r^{v-1}}$-point DFT at stage v.
2. Each ηth $\frac{N}{r^{v-1}}$-point DFTs is reduced to smaller point DFTs in the $m - v$ subsequent stages. Hence, the FFT outputs corresponding to the inputs of the ηth $\frac{N}{r^{v-1}}$-point

DFTs at a particular stage v is obtained from (4.21) as

$$X^{\eta}(r\widetilde{k}+k_0)=\sum_{\widetilde{n}=0}^{\frac{N}{r^v}-1}\left(\left(\sum_{i=0}^{r-1}\widetilde{x}^{\eta}(\widetilde{n}+\frac{N}{r^v}i)T_r^{ik_0}\right)T_{N/r^{v-1}}^{\widetilde{n}\,k_0}\right)T_{N/r^v}^{\widetilde{k}\,\widetilde{n}} \tag{4.22}$$

where $\widetilde{k}=0,\ldots,\frac{N}{r^v}-1$, $\widetilde{n}=0,\ldots,\frac{N}{r^v}-1$ and $\eta=1,\ldots,r^{v-1}$. Finally, from (4.22) FFT outputs related to all inputs to the $\frac{N}{r^{v-1}}$-point DFTs at a particular stage v is

$$\begin{aligned}X(rk+k_0) &= \sum_{\eta=1}^{r^{v-1}}X^{\eta}(r\widetilde{k}+k_0) \qquad (4.23)\\ &= \sum_{\eta=1}^{r^{v-1}}\sum_{\widetilde{n}=0}^{\frac{N}{r^v}-1}\left(\left(\sum_{i=0}^{r-1}\widetilde{x}^{\eta}(\widetilde{n}+\frac{N}{r^v}i)T_r^{ik_0}\right)T_{N/r^{v-1}}^{\widetilde{n}\,k_0}\right)T_{N/r^v}^{\widetilde{k}\,\widetilde{n}}.\end{aligned}$$

Thus, the inputs at stage v are

$$\left[\widetilde{\mathbf{x}}^1,\widetilde{\mathbf{x}}^2,\ldots,\widetilde{\mathbf{x}}^{\eta},\ldots,\widetilde{\mathbf{x}}^{r^{v-1}}\right]^T \tag{4.24}$$

with dimensions $r^{v-1}\times N/r^{v-1}$ where

$$\widetilde{\mathbf{x}}^{\eta}=\left[x^{\eta}(0),\widetilde{x}^{\eta}(1),\ldots,\widetilde{x}^{\eta}(\widetilde{n}+\frac{N}{r^v}i),\ldots,\widetilde{x}^{\eta}(\frac{N}{r^{v-1}}-1)\right] \tag{4.25}$$

has dimensions N/r^{v-1}. In fact, Figure 4.6 illustrates the reduction of the N/r^{v-1}-point DFTs to $r^v\times N/r^v$ DFTs at stage v. In order to show each butterfly input, $\widetilde{\mathbf{x}}^{\eta}$ in Figure 4.6 can be rearranged as

$$\widetilde{\mathbf{x}}^{\eta}=\begin{bmatrix}\widetilde{x}^{\eta}(0) & \widetilde{x}^{\eta}(1) & \ldots & \widetilde{x}^{\eta}(\frac{N}{r^v}-1)\\ \widetilde{x}^{\eta}(\frac{N}{r^v}) & \widetilde{x}^{\eta}(\frac{N}{r^v}+1) & \ldots & \widetilde{x}^{\eta}(2\frac{N}{r^v}-1)\\ \vdots & \vdots & \ddots & \vdots\\ \widetilde{x}^{\eta}((r-1)\frac{N}{r^v}) & \widetilde{x}^{\eta}((r-1)\frac{N}{r^v}+1) & \ldots & \widetilde{x}^{\eta}(\frac{N}{r^{v-1}}-1)\end{bmatrix} \tag{4.26}$$

When $N\neq r^m$, a mixed radix with different r values is used, giving $N=r_1^{m_1}r_2^{m_2}$ where $v_1=1,\ldots,m_1$ and $v_2=1,\ldots,m_2$ are the number of stages for the different DIF indices.

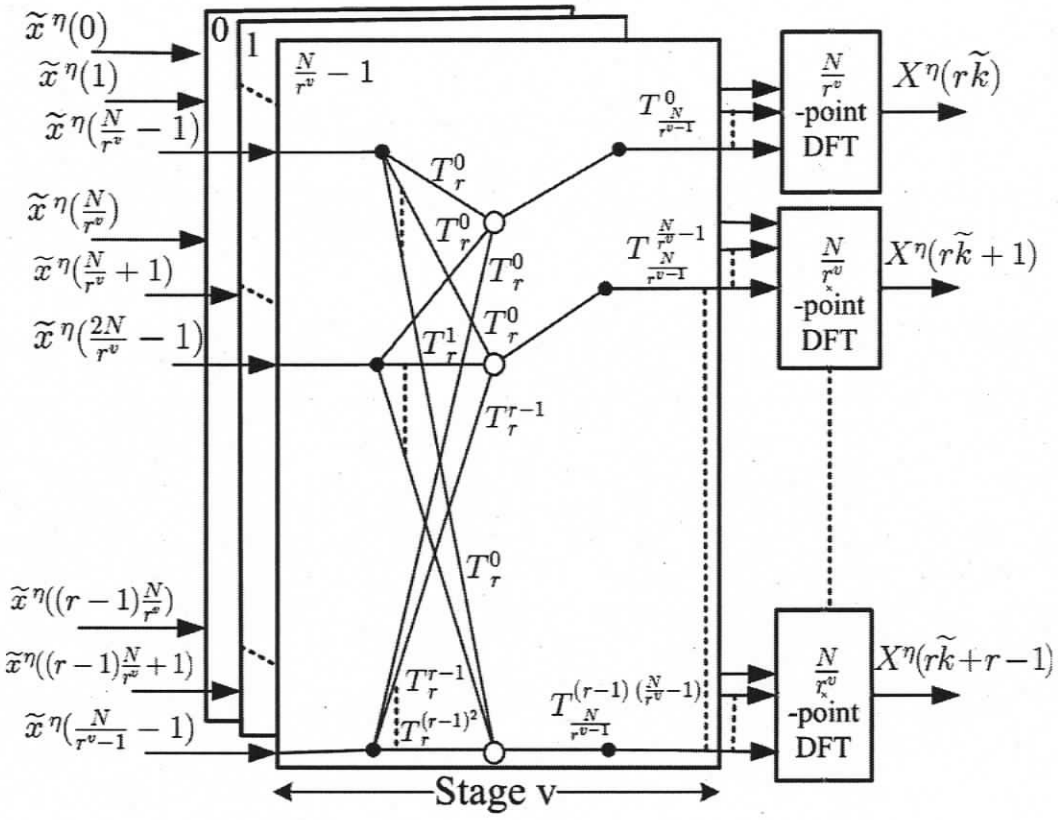

Figure 4.6. *Recursive reduction of $\frac{N}{r^{v-1}}$-point DFTs with DIF radix-r at stage v.*

2) DIT algorithms: Similarly, the DIT radix-r algorithm from (4.19) is given by the block diagram in Figure 4.7. It illustrates the DIT reduction to $\frac{N}{r^{m-v}}$-point DFTs. In this case, there are $r^{m-v} \times \frac{N}{r^{m-v}}$-point DFTs at stage v, i.e., α, $\alpha = 1, \ldots, r^{v-1}$, denotes a particular $\frac{N}{r^{m-v}}$-point DFT. Figure 4.7 shows identical $\frac{N}{r^{m-v}}$-point DFTs at stage v. Similar to DIF, the symbols and indices at stage v are represented by the notation $\widehat{x}$ and $\widehat{n}$ for an input x and time index n, respectively, and $\widehat{k}$ for a frequency index k. Then, the FFT output $X(\widehat{k})$ corresponds to the inputs $x(\widehat{n})$ at stage v.

The inputs to stage v are

$$\left[\widehat{\mathbf{x}}^1, \widehat{\mathbf{x}}^2, \ldots, \widehat{\mathbf{x}}^{\alpha}, \ldots, \widehat{\mathbf{x}}^{r^{m-v}}\right]^T \tag{4.27}$$

where $\widehat{\mathbf{x}}^{\alpha}$ is

$$\widehat{\mathbf{x}}^{\alpha} = \left[x^{\alpha}(0), \widehat{x}^{\alpha}(1), \ldots, \widehat{x}^{\alpha}(r\widehat{n}+i), \ldots, \widehat{x}^{\alpha}(\frac{N}{r^{m-v}}-1)\right]. \tag{4.28}$$

By rearranging the inputs in Figure 4.7,the matrix $\widehat{\mathbf{x}}^{\alpha}$ is expressed as

$$\widehat{\mathbf{x}}^{\alpha} = \begin{bmatrix} \widehat{x}^{\alpha}(0) & \widehat{x}^{\alpha}(r) & \ldots & \widehat{x}^{\alpha}(\frac{N}{r^{m-v}}-r) \\ \widehat{x}^{\alpha}(1) & \widehat{x}^{\alpha}(r+1) & \ldots & \widehat{x}^{\alpha}(\frac{N}{r^{m-v}}-r+1) \\ \vdots & \vdots & \ddots & \vdots \\ \widehat{x}^{\alpha}(r-1) & \widehat{x}^{\alpha}(2r-1) & \ldots & \widehat{x}^{\alpha}(\frac{N}{r^{m-v}}-1) \end{bmatrix}. \tag{4.29}$$

Using (4.19), the FFT output corresponding to the inputs $\widehat{\mathbf{x}}^{\alpha}$ at a particular stage v is determined as

$$X^{\alpha}(\widehat{k}+k_0\frac{N}{r^{m-v+1}}) = \sum_{\widehat{n}=0}^{\frac{N}{r^{m-v+1}}-1}\left(\sum_{i=0}^{r-1}\widehat{x}^{\alpha}(r\widehat{n}+i)T_r^{ik_0}T_{N/r^{m-v}}^{\widehat{k}i}\right) \tag{4.30}$$

where $\widehat{k} = 0, \ldots, \frac{N}{r^{m-v+1}}-1$, $\widehat{n} = 0, \ldots, \frac{N}{r^{m-v+1}}-1$. Summing over all $\frac{N}{r^{m-v}}$ -point DFT outputs gives

$$X(\widehat{k}+k_0\frac{N}{r}) = \sum_{\alpha=1}^{r^{m-v}} X^{\alpha}(\widehat{k}+k_0\frac{N}{r^{m-v+1}}) = \sum_{\alpha=1}^{r^{m-v}}\sum_{\widehat{n}=0}^{\frac{N}{r^{m-v+1}}-1}\left(\sum_{i=0}^{r-1}\widehat{x}^{\alpha}(r\widehat{n}+i)T_r^{ik_0}T_{N/r^{m-v}}^{\widehat{k}i}\right)T_{N/r^{m-v+1}}^{\widehat{k}\widehat{n}}. \tag{4.31}$$

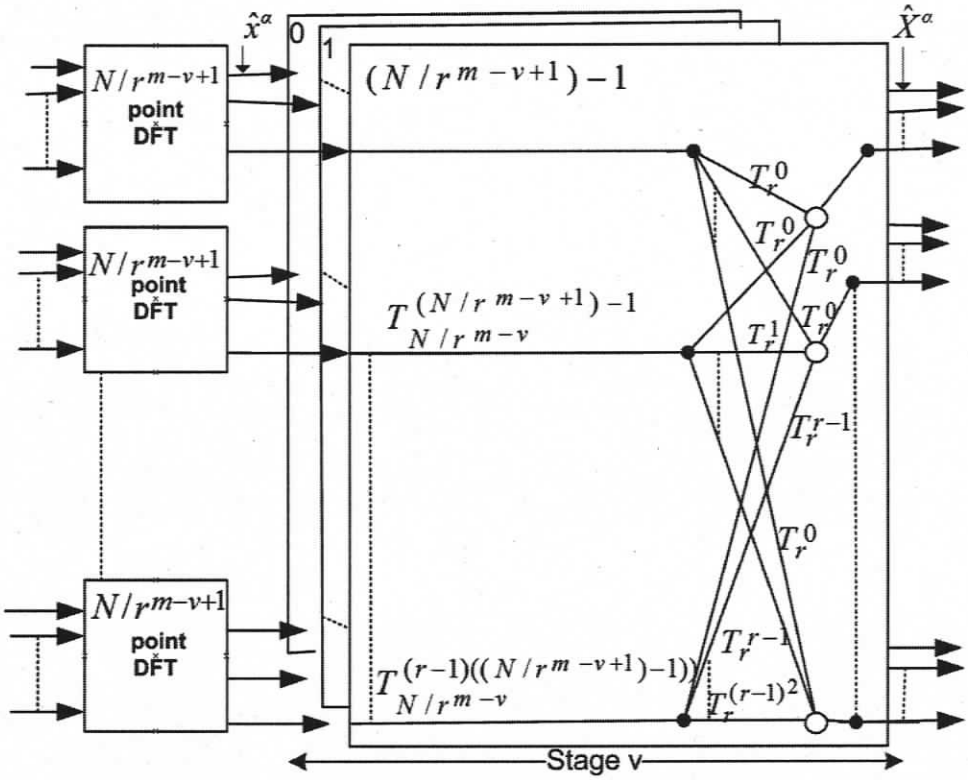

Figure 4.7. *Recursive reduction of $\frac{N}{r^{m-v}}$-point DFTs with DIT radix-r at stage v.*

Equations (4.23) and (4.31) will be used for the basis to proposed IFFT-based PTS and SLM techniques in Chapter 5.

3) The identical DFTs submatrices: The FFT outputs related to the inputs to the identical DFTs can also be expressed based on the direct DFT matrices. For convenience, (2.9) is repeated below

$$X(k) = \sum_{n=0}^{N-1} x(n) T_N^{nk} \quad 0 \le n \le N-1, \ \ 0 \le k \le N-1. \tag{4.32}$$

By replacing (4.25) into (4.32), the ηth N/r^{v-1}-point DFT using DIF algorithm can be computed as

$$X^{\eta}(\widetilde{k}) = \sum_{\widetilde{k}=0}^{\frac{N}{r^{v-1}}-1} \widetilde{x}^{\eta}(\widetilde{n}) T^{\widetilde{n}\widetilde{k}}_{N/r^{v-1}}. \tag{4.33}$$

Hence, the FFT output corresponding to the inputs at a particular stage v can be expressed as

$$X(k) = \sum_{\eta=1}^{r^{v-1}} X^{\eta}(\widetilde{k}) = \sum_{\eta=1}^{r^{v-1}} \sum_{\widetilde{k}=0}^{\frac{N}{r^{v-1}}-1} \widetilde{x}^{\eta}(\widetilde{n}) T^{\widetilde{n}\widetilde{k}}_{N/r^{v-1}}. \tag{4.34}$$

In order to obtain (4.33) in matrix notation, we use the DFT form of (2.8) to obtain

$$\mathbf{X} = \check{Q}\mathbf{x} \tag{4.35}$$

where Q'_N is the $N \times N$ direct DFT matrix with elements T^k_N given by

$$\check{Q} = \begin{bmatrix} 1 & \cdots & 1 & \cdots & 1 \\ \vdots & \ddots & \vdots & \ddots & \vdots \\ 1 & \cdots & T_N^{nk} & \cdots & T_N^{n(N-1)} \\ \vdots & \ddots & \vdots & \ddots & \vdots \\ 1 & \cdots & T_N^{k(N-1)} & \cdots & T_N^{(N-1)^2} \end{bmatrix}_{N\times N}. \tag{4.36}$$

Considering the form of (4.33) and (4.34), we can write (4.35) for the ηth N/r^{v-1}-point DFT

$$\mathbf{X}^{\eta} = \check{Q}^{\eta}\mathbf{x}^{\eta}. \tag{4.37}$$

Hence, the IFFT output corresponding to inputs at satge v is

$$\begin{bmatrix} X(0) \\ X(1) \\ \vdots \\ X(k) \end{bmatrix}_N = \begin{bmatrix} \widetilde{X}^1(\widetilde{k}) \\ \vdots \\ \widetilde{X}^{\eta}(\widetilde{k}) \\ \vdots \\ \widetilde{X}^{r^{v-1}}(\widetilde{k}) \end{bmatrix}_N = \begin{bmatrix} \check{Q}^1 \\ \vdots \\ \check{Q}^{\eta} \\ \vdots \\ \check{Q}^{r^{v-1}} \end{bmatrix}_{N\times N} \begin{bmatrix} \widetilde{x}^1(\widetilde{n}) \\ \vdots \\ \widetilde{x}^{\eta}(\widetilde{n}) \\ \vdots \\ \widetilde{x}^{r^{v-1}}(\widetilde{n}) \end{bmatrix}_N \tag{4.38}$$

where the (identical) submatrices are

$$\check{Q}^1 = \ldots = \check{Q}^\eta \ldots = \check{Q}^{r^{v-1}} = \begin{bmatrix} 1 & \cdots & 1 & \cdots & 1 \\ \vdots & \ddots & \vdots & \ddots & \vdots \\ 1 & \cdots & T_{N/r^{v-1}}^{\tilde{n}\tilde{k}} & \cdots & T_{N/r^{v-1}}^{\tilde{n}(N/r^{v-1}-1)} \\ \vdots & \ddots & \vdots & \ddots & \vdots \\ 1 & \cdots & T_{N/r^{v-1}}^{\tilde{k}(N/r^{v-1}-1)} & \cdots & T_{N/r^{v-1}}^{(N/r^{v-1}-1)^2} \end{bmatrix}_{N/r^{v-1} \times N/r^{v-1}} \tag{4.39}$$

Using similar approach to that for the DIF FFTs, the FFT output $X(k)$ using DIT is given by

$$\begin{bmatrix} X(0) \\ X(1) \\ \vdots \\ X(k) \end{bmatrix}_N = \begin{bmatrix} \widehat{X}^1(\widehat{k}) \\ \vdots \\ \widehat{X}^\alpha(\widehat{k}) \\ \vdots \\ \widehat{X}^{r^{m-v}}(\widehat{k}) \end{bmatrix}_N = \begin{bmatrix} \check{Q}^1 \\ \vdots \\ \check{Q}^\alpha \\ \vdots \\ \check{Q}^{r^{m-v}} \end{bmatrix}_{N \times N} \begin{bmatrix} \widehat{x}^1(\widehat{n}) \\ \vdots \\ \widehat{x}^\alpha(\widehat{n}) \\ \vdots \\ \widehat{x}^{r^{m-v}}(\widehat{n}) \end{bmatrix}_N \tag{4.40}$$

where the submatrices are

$$\check{Q}^1 = \ldots = \check{Q}^\alpha \ldots = \check{Q}^{r^{v-1}} = \begin{bmatrix} 1 & \cdots & 1 & \cdots & 1 \\ \vdots & \ddots & \vdots & \ddots & \vdots \\ 1 & \cdots & T_{N/r^{m-v}}^{\widehat{n}\widehat{k}} & \cdots & T_{N/r^{m-v}}^{\widehat{n}(N/r^{m-v}-1)} \\ \vdots & \ddots & \vdots & \ddots & \vdots \\ 1 & \cdots & T_{N/r^{m-v}}^{\widehat{k}(N/r^{m-v}-1)} & \cdots & T_{N/r^{m-v}}^{(N/r^{m-v}-1)^2} \end{bmatrix}_{N/r^{m-v} \times N/r^{m-v}} \tag{4.41}$$

The difference between (4.39) and (4.41) comes from the order of the inputs and outputs which was assumed for DIF and DIT in Section 4.2.1.2. If both algorithms uses the same order of the inputs and outputs, the submatrices $\check{Q}^\eta$ and $\bar{Q}^\alpha$ becomes similar. These submatrices will be used in the IFFT-based TR technique in the next chapter to simplify the iterative gradient algorithm.

4.2.4 Radix-r FFT computational complexity

The radix-r FFT algorithms based on FFT processing stages derived in last section allow us to compute the computational complexity per stage. The computational complexity consists of multiplicative and additive complexity. Comparing Figures 4.6 and 4.7, the multiplicative complexity of DIF algorithms differs from that of DIT algorithms since their twiddle factors are different at each stage. However, we will see that both algorithms have the same additive complexity per stage.

From (4.22) and Figure 4.6, the multiplicative complexity per stage for the radix-r DIF algorithm is defined as the number of complex multiplications by twiddle factors $T_{N/r^{v-1}}^{\tilde{n}k_0}$ and $T_r^{ik_0}$. Let $B_{v,DIF}^{mul}$ denote the number of twiddle factors $T_{N/r^{v-1}}^{\tilde{n}k0}$ and $T_r^{ik_0}$ at stage v for the DIF algorithm. From Figure 4.6, summing over all dimensions $\tilde{n}$ and k_0, and r^{v-1} identical N/r^{v-1}-point DFTs, we obtain

$$B_v^{mul,DIF} = r^{v-1}(\frac{N}{r^v} - 1). \tag{4.42}$$

Similar to DIF, from (4.30) and Figure 4.6 , summing over all dimensions $\widehat{k}$, outputs k_0, and DFTs, we can obtain the multiplicative complexity per stage for the radix-r DIT algorithm corresponding to the twiddle factors $T_r^{ik_0}$ and $T_{N/r^{m-v}}^{\widehat{k}i}$ as

$$B_v^{mul,DIT} = r^{m-v}(\frac{N}{r^{m-v+1}} - 1). \tag{4.43}$$

As previously explained in Section 4.2.1.3, we consider only radix-2 and radix-4 to have an efficient hardware implementation. Therefore, the twiddle factors $T_r^{ik_0}$ become trivial (± 1 and $\pm j$) at each stage.

It is obvious that the total number of nontrivial multiplications for DIF radix-r and DIT radix-r can be computed using (4.42) and (4.43) as

$$B_{total}^{mul,DIF} = \sum_{v=1}^{m} B_v^{mul,DIF} = \sum_{v=1}^{m} r^{v-1}(\frac{N}{r^v} - 1), \tag{4.44}$$

and

$$B_{total}^{mul,DIT} = \sum_{v=1}^{m} B_v^{mul,DIT} = \sum_{v=1}^{m} r^{m-v}(\frac{N}{r^{m-v+1}} - 1), \tag{4.45}$$

respectively. For additive complexity, from Figure 4.6 and (4.30) the number of additions for the radix-r DIF algorithm at stage v can be obtained as

$$B_v^{add,DIF} = r^{v-1}[\frac{N}{r^v}r(r-1)] = N(r-1). \tag{4.46}$$

The additive complexity for the DIT algorithm is

$$B_v^{add,DIT} = r^{m-v}[\frac{N}{r^{m-v+1}}r(r-1)] = N(r-1). \tag{4.47}$$

Thus, the additive complexity per stage is the same as with DIF, and the total additive complexity for both algorithms is defined as

$$B_{total}^{add} = vN(r-1). \tag{4.48}$$

Chapter 5

IFFT-Based PAPR Reduction Techniques

A detailed description of the new techniques for PAPR reduction, called IFFT-based techniques, is now presented. The common FFT algorithms discussed in the last chapter are considered together with the distortionless PAPR reduction techniques in Chapter 3, PTS, SLM, and TR. We introduce PAPR reduction techniques for each IFFT-based scheme which have low complexity compared to conventional techniques. Theoretical analysis is employed to analyze the PAPR capability of these techniques. This chapter also presents the extensive numerical results on the behaviour of the IFFT-based techniques in a variety of different situations. These results are compared with the results of the previously developed techniques.

5.1 PTS and the Common FFT Algorithms

As discussed in Chapter 3, one of the major drawback of PTS arises from the computation of multiple IFFTs, resulting in a high complexity proportional to the number of subblocks. In an attempt to reduce this complexity, intermediate signals within the IFFT using decimation in time (DIT) have been used to obtain the PTS subblocks [53]. Multiple IFFTs are then applied to the remaining stages. Accordingly, the number of stages requiring multiple IFFTs is reduced. Although this approach reduces the computational complexity, the

common FFT algorithms in terms of PAPR reduction and computational complexity have not been analyzed. The multiplicative complexity which largely determines the computational complexity of the remaining stages was not significantly reduced. This is because the multiplicative complexity of the remaining stages strongly depends on the type of FFT algorithm. This complexity is related to whether a DIF or DIT algorithm is employed. In addition, as discussed in Chapter 3, higher radix FFT algorithms can reduce the number of processing stages and complex multiplications compared to lower radix FFT algorithms.

The experimental results in [53] show that the PAPR reduction decreases as the number of stages after PTS partitioning decreases. Therefore, to achieve PAPR reduction close to that of original PTS (O-PTS), there should be a substantial number of stages remaining in the IFFT after the partitioning into PTS subblocks. Hence, the computational complexity may not be significantly reduced. As a consequence, the main challenge is how to decrease the complexity while maintaining a PAPR reduction close to that of O-PTS.

To improve the computational complexity and PAPR performance, an IFFT-based PTS technique is introduced in this thesis where the inputs to IFFT stages $1 < v \leq m$ are used for PTS subblock partitioning. The analysis is based on the corresponding fast Fourier transform (FFT). PTS subblocking is done in the middle stages of the N-point radix FFT DIF or DIT algorithm. It is shown that DIT has a majority of its complex multiplication operations towards the end of the computation stages, and DIF has a majority towards the beginning. Thus, DIF has lower multiplicative complexity in generating PTSs compared to DIT, and the same PAPR reduction. The PAPR performance is verified through numerical results. We also show that high radix algorithms achieve better PAPR reduction per stage compared to low radix algorithms, while providing lower multiplicative complexity.

We exploit (4.23) and (4.31) to formulate OFDM symbols based on the inputs to each stage of an N-point FFT using a radix-r DIF and DIT, respectively. This allows us to construct PTS subblocks for the inputs to each stage, and derive their periodic auto-correlation function (ACF). The ACF provides a design criteria for PTS subblocking to reduce the PAPR and computational complexity. We also show that pseudo-random [27] and M-

sequence subblocking [53] are not optimal as they introduce repeated subcarriers in the subblocks. As a consequence, we propose a new PTS subblocking technique based on error-correcting codes (ECCs). This minimizes the number of repeated subcarriers and provides better PAPR reduction than pseudo-random or M-sequence subblocking. The computational complexity is reduced as the significant PAPR reduction is achieved using a small number of IFFT stages. We also evaluate the BER performance of the proposed technique in the OFDM system shown in Figure 2.5.

5.1.1 IFFT-based PTS

Consider the IDFT in (2.6)

$$\begin{aligned} x(n) &= \frac{1}{N}\sum_{k=0}^{N-1} X(k)T_N^{-nk} \quad 0 \le n \le N-1,\ 0 \le k \le N-1, \\ T_N &= e^{-j2\pi/N}. \end{aligned} \tag{5.1}$$

We can write (5.1) as

$$x(n) = \frac{1}{N}\left[\sum_{k=0}^{N-1} X^*(k)T_N^{nk}\right]^*. \tag{5.2}$$

Let $y(.)$ represents $X^*(.)$. From (2.9), the expression inside the brackets in (5.2) is the DFT of $X^*(.)$ i.e.

$$Y(k) = \sum_{n=0}^{N-1} y(n)T_N^{nk}. \tag{5.3}$$

According to (5.2) and (5.3), the IDFT can be performed by taking the complex conjugate of the input data first, and also the output without changing any coefficients in the original DFT. This is illustrated in Figure 5.1. Consequently, we focus here on the DFT computation.

To derive IFFT-based PTS using a radix-r DIF algorithm, consider (5.3) based on the inputs to the $\frac{N}{r^{v-1}}$-point DFTs using (4.22) and (4.23) as

$$Y^{\eta}(r\widetilde{k}+k_0) = \sum_{\widetilde{n}=0}^{\frac{N}{r^v}-1}\left(\left(\sum_{i=0}^{r-1}\widetilde{y}^{\eta}(\widetilde{n}+\frac{N}{r^v}i)T_r^{ik_0}\right)T_{N/r^{v-1}}^{\widetilde{n}\,k_0}\right)T_{N/r^v}^{\widetilde{k}\,\widetilde{n}} \tag{5.4}$$

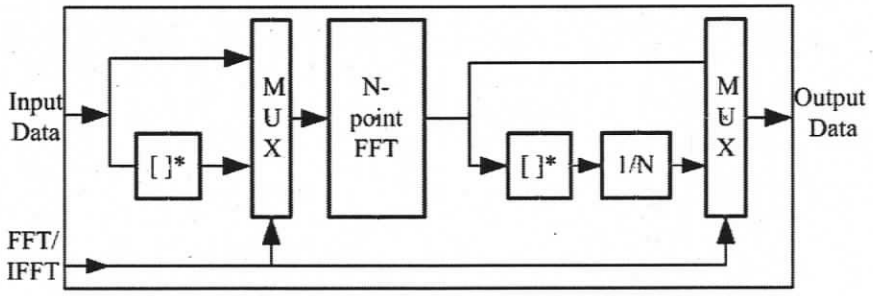

Figure 5.1. *Block diagram of FFT/IFFT computation.*

and

$$Y(rk+k_0)=\sum_{\eta=1}^{r^{v-1}}Y^{\eta}(r\widetilde{k}+k_0)=\sum_{\eta=1}^{r^{v-1}}\sum_{\widetilde{n}=0}^{\frac{N}{r^v}-1}\left(\left(\sum_{i=0}^{r-1}\widetilde{y}^{\eta}(\widetilde{n}+\frac{N}{r^v}i)T_r^{ik_0}\right)T_{N/r^{v-1}}^{\widetilde{n}\,k_0}\right)T_{N/r^v}^{\widetilde{k}\,\widetilde{n}}. \tag{5.5}$$

Furthermore, the inputs at stage v using (4.24) and (4.25) are

$$\left[\widetilde{\mathbf{y}}^1,\widetilde{\mathbf{y}}^2,\ldots,\widetilde{\mathbf{y}}^{\eta},\ldots,\widetilde{\mathbf{y}}^{r^{v-1}}\right]^T_{r^{v-1}\times N/r^{v-1}} \tag{5.6}$$

where

$$\widetilde{\mathbf{y}}^{\eta}=\left[y^{\eta}(0),\widetilde{y}^{\eta}(1),\ldots,\widetilde{y}^{\eta}(\widetilde{n}+\frac{N}{r^v}i),\ldots,\widetilde{y}^{\eta}(\frac{N}{r^{v-1}}-1)\right]_{N/r^{v-1}} \tag{5.7}$$

Similar to O-PTS in (3.5), and using (5.2) and (5.5), we obtain

$$\begin{aligned}x'(n)&=\sum_{p=0}^{P-1}e^{-j\,\theta_p}\frac{1}{N}\left[\sum_{\eta=1}^{r^{v-1}}Y_p^{\eta}(r\widetilde{k}+k_0)\right]^*\\&=\sum_{p=0}^{P-1}e^{-j\,\theta_p}x_p(n)\end{aligned} \tag{5.8}$$

where the PTSs are

$$\frac{1}{N}\left[\sum_{\eta=1}^{r^{v-1}}Y_p^{\eta}(r\widetilde{k}+k_0)\right]^*. \tag{5.9}$$

Subblocks are composed over the inputs $\widetilde{y}^{\eta}(\widetilde{n}+\frac{N}{r^v}i)$ to the identical $\frac{N}{r^{v-1}}$-point DFTs in (5.4) or equivalently $\widetilde{\mathbf{y}}^{\eta}$ in (5.6) at stage v.

Similarly, IFFT-based PTS using a radix-r DIT algorithm is derived using (5.2) and (3.5) as

$$x'(n) = \sum_{p=0}^{P-1} e^{-j\,\theta_p} \frac{1}{N} \left[\sum_{\alpha=1}^{r^{m-v}} Y_p^{\alpha}(\widehat{k} + k_0 \frac{N}{r^{m-v+1}}) \right]^* = \sum_{p=0}^{P-1} e^{-j\,\theta_p} x^p(n) \tag{5.10}$$

where $Y_p^{\alpha}(\widehat{k} + k_0 \frac{N}{r^{m-v+1}})$ is obtained by substituting (5.3) into (4.30) as

$$Y^{\alpha}(\widehat{k} + k_0 \frac{N}{r^{m-v+1}}) = \sum_{\widehat{n}=0}^{\frac{N}{r^{m-v+1}}-1} \left(\sum_{i=0}^{r-1} \widehat{y}^{\alpha}(r\widehat{n} + i) T_r^{ik_0} T_{N/r^{m-v}}^{\widehat{k}i} \right). \tag{5.11}$$

In this case, the PTSs are

$$\frac{1}{N} \left[\sum_{\alpha=1}^{r^{v-1}} Y_p^{\alpha}(\widehat{k} + k_0 \frac{N}{r^{m-v+1}}) \right]^* \tag{5.12}$$

where

$$Y(k + k_0 \frac{N}{r}) = \sum_{\alpha=1}^{r^{m-v}} Y^{\alpha}(\widehat{k} + k_0 \frac{N}{r^{m-v+1}}) = \sum_{\alpha=1}^{r^{m-v}} \sum_{\widehat{n}=0}^{\frac{N}{r^{m-v+1}}-1} \left(\sum_{i=0}^{r-1} \widehat{y}^{\alpha}(r\widehat{n} + i) T_r^{ik_0} T_{N/r^{m-v}}^{\widehat{k}i} \right) T_{N/r^{m-v+1}}^{\widehat{k}\,\widehat{n}}. \tag{5.13}$$

PTS subblocking is done over the inputs $\widehat{y}^{\alpha}(r\widehat{n} + i)$ or equivalently $\widehat{\mathbf{y}}$ which is obtained from (4.27) and (4.28), i.e.

$$\left[\widehat{\mathbf{y}}^1, \widehat{\mathbf{y}}^2, \ldots, \widehat{\mathbf{y}}^{\alpha}, \ldots, \widehat{\mathbf{y}}^{r^{m-v}} \right]^T \tag{5.14}$$

where $\widehat{\mathbf{y}}^{\alpha}$ is

$$\widehat{\mathbf{y}}^{\alpha} = \left[\widehat{y}^{\alpha}(0), \widehat{y}^{\alpha}(1), \ldots, \widehat{y}^{\alpha}(r\widehat{n} + i), \ldots, \widehat{y}^{\alpha}(\frac{N}{r^{m-v}} - 1) \right]. \tag{5.15}$$

As mentioned at the beginning of this section and from Figure 5.1, the IFFT and FFT operations use the same coefficients. Hence, to recover the data at the receiver we use the same coefficients for the FFT as for the IFFT at the transmitter. However, we must take

into account the IFFT input orders (see Section 4.2.1.2) at the transmitter. If we assume these inputs are in normal order, the inputs to the FFT at the receiver should be in reverse order. Thus, the FFT computation at the receiver is symmetric to the IFFT computation, and if stage v is used to obtain the PTS subblocks, the data is recovered at stage $m - v$ at the receiver. Hence, the amount of side information remains the same as that of O-PTS.

5.1.1.1 Computational complexity

The overall multiplicative complexity for the IFFT-based PTS using DIF with P sunblocks can be computed by (4.42)

$$B^{mul,DIF} = \sum_{i=1}^{v-1} B_i^{mul,DIF} + P \sum_{i=v}^{m} B_i^{mul,DIF}. \tag{5.16}$$

Similarly, from (4.43) the overall multiplicative complexity for the IFFT-based PTS using DIT with P subblocks is

$$B^{mul,DIT} = \sum_{i=1}^{v-1} B_i^{mul,DIT} + P \sum_{i=v}^{m} B_i^{mul,DIT}. \tag{5.17}$$

Since both algorithm have the same additive complexity per stage (see (4.48)), the overall additive complexity for the IFFT-based PTS with P subblocks is

$$B_{add} = Nr(r-1)[v + P(m-v)]. \tag{5.18}$$

5.1.1.2 DIF versus DIT algorithms

In this section, the performance of IFFT-based PTS is evaluated in terms of computational complexity and PAPR when DIF and DIT are employed.

1) Successive multiplicative complexity analysis: Using (4.42), the ratio between successive numbers $B_v^{mul,DIF}$ is obtained by

$$\frac{B_v^{mul,DIF}}{B_{v+1}^{mul,DIF}} = \frac{r^{v-1}(\frac{N}{r^v} - 1)}{r^v(\frac{N}{r^{v+1}} - 1)} = \frac{(\frac{N}{r^v} - 1)}{(\frac{N}{r^v} - r)} \tag{5.19}$$

Table 5.1. *Multiplicative complexity for the radix-2 DIF and DIT FFTs with* $N = 256, 2048, 8192$ *and* $2 \leq m - v \leq 6$.

$m-v$	$B^{mul,DIF}$			$B^{mul,DIT}$		
	$N=256$	$N=2048$	$N=8192$	$N=256$	$N=2048$	$N=8192$
2	64	512	2048	253	2045	8189
3	160	1280	5120	377	3065	12281
4	272	3136	8704	497	4081	16369
5	392	2176	12544	609	5089	20449
6	516	4128	16512	705	6081	24513

which is evidently greater than one, i.e., $B_{v+1}^{mul,DIF} < B_v^{mul,DIF}$. Thus $B_v^{mul,DIF}$ is diminishing through successive stages and at $v = m$, this number is zero. For the DIT algorithm, from (4.43), the ratio between successive numbers $B_v^{mul,DIT}$ is

$$\frac{B_v^{mul,DIT}}{B_{v+1}^{mul,DIT}} = \frac{r^{m-v}(\frac{N}{r^{m-v+1}} - 1)}{r^{m-v-1}(\frac{N}{r^{m-v}} - 1)} = \frac{(\frac{N}{r^{m-v+1}} - 1)}{(\frac{N}{r^{m-v+1}} - \frac{1}{r})}. \tag{5.20}$$

This amount is less than one ($B_{v+1}^{mul,DIT} > B_v^{mul,DIT}$), and consequently grows through successive stages and at $v = 1$, this number is zero. Since IFFT-based PTS computes the multiple IFFTs for $m - v$ stages, DIT results in greater multiplicative complexity over the last $m - v$ stages compared to DIF.

As an example, to compare the multiplicative complexity for $m - v$ stages, consider $N = 256, 2048, 8192$ for radix-2 DIF and DIT algorithms. This multiplicative complexity on a logarithmic scale is given in Figure (5.2), and also shown as number of multiplications in Table 5.1.

2) Performance results:

In order to compare the multiplicative complexity between two PAPR reduction techniques, we define the multiplicative complexity reduction ratio as

$$R^{mul} = 1 - \frac{B^{mul,1}}{B^{mul,2}} \tag{5.21}$$

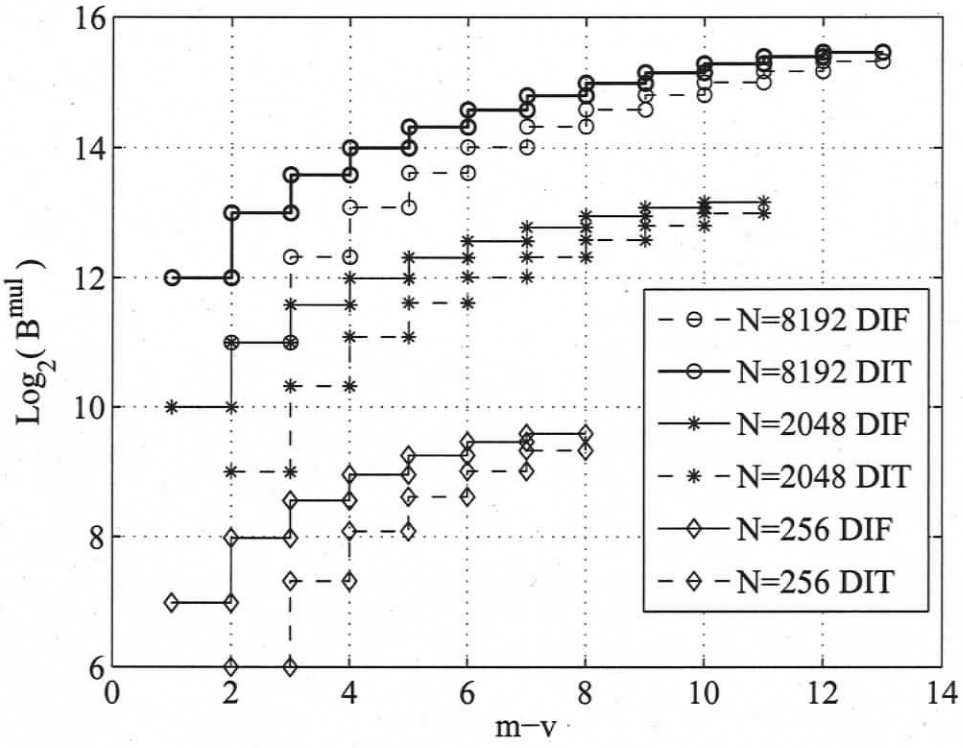

Figure 5.2. *Number of nontrivial multiplications versus the number of remaining stages $m - v$ for DIF radix-2 compared with DIT radix-2 and $N = 256, 2048, 8192$.*

where the overall multiplicative complexity for the IFFT-based PTS technique using DIF (DIF-PTS) or DIT (DIT-PTS) are given by (5.16) and (5.17), respectively. Table 5.2 shows DIF-PTS in comparison with DIT-PTS and O-PTS for $N = 256, 2048, 8192$ and $2 \leq m - v \leq 6$ where the number of PTS subblocks is $P = 8$ and $N = 256, 2048$. In this case, DIF-PTS reduces the multiplicative complexity by 23% to 52% for 8 PTS subblocks. The corresponding reduction over O-PTS is 29% to 84%.

To evaluate the PAPR performance, we consider the CCDF of 16 QAM-modulated OFDM signals where $J = 4$ and $W = 4$. The number of subblocks is $P = 8$ and the first subblock is not rotated so that only $P - 1$ phases are optimized. Either DIT or DIF can be

Table 5.2. *Multiplicative complexity reduction for DIF-PTS over DIT-PTS and O-PTS, with* $P = 8$, $N = 256, 2048, 8192$, *and* $2 \leq m - v \leq 6$.

$m - v$	$R^{mul}(\%)$, $P = 8$			$R^{mul}(\%)$, $P = 8$		
	DIF-PTS compared to DIT-PTS			DIF-PTS compared to O-PTS		
	$N = 256$	$N = 2048$	$N = 8192$	$N = 256$	$N = 2048$	$N = 8192$
2	52	46	42	80	83	84
3	45	41	38	69	75	78
4	37	35	34	57	67	71
5	30	30	29	43	58	63
6	23	26	26	29	48	55

used for O-PTS as in this case they have the same multiplicative and additive complexity. The PAPR reduction and related computational complexity are compared as follows.

The CCDFs of radix-2 DIF-PTS and DIT-PTS at stage $m - v = 5$ and O-PTS are depicted in Figure 5.3 for $P = 8$ and $N = 256, 2048$. They have almost the same performance. In this case, DIF-PTS achieves a multiplicative complexity reduction ratio $R^{mul} = 30\%$ over DIT-PTS. This value increases to $R^{mul} = 43\%, 58\%$ when compared to O-PTS, as shown in Table 5.2.

5.1.1.3 High radix versus low radix algorithms

As discussed in Chapter 4, higher radix algorithms have fewer number of stages and non-trivial multiplications compared to lower radix algorithms. We choose $r = 4$ as a high radix to compare with the low radix case $r = 2$. The CCDFs of DIF with radix-4 and radix-2 is considered for $N = 256, 2048$ and $P = 8$. The multiplicative complexity reduction with the same CCDF and different PTS techniques is shown in Table 5.3. For $N = 256$, Figure 5.4 shows almost the same PAPR reduction for $m - v = 5$ and $m - v = 3$ for radix-2 and radix-4, respectively, with almost a 21% multiplicative complexity reduction. In addition, DIF-PTS radix-4 achieves a 55% multiplicative complexity reduction over O-PTS.

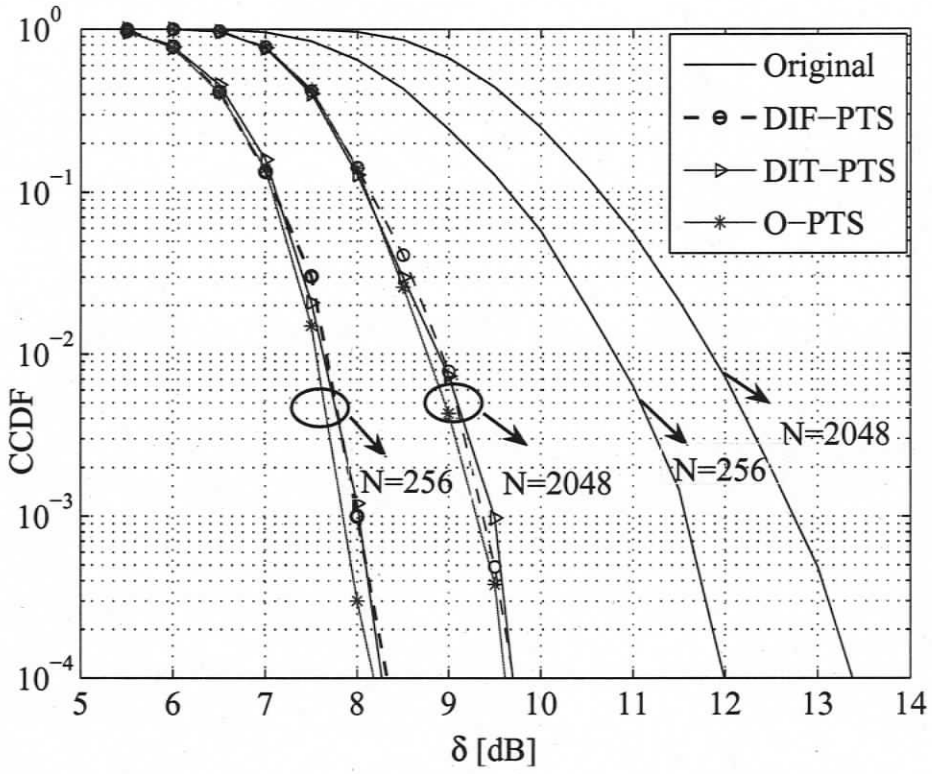

Figure 5.3. *CCDF of DIF-PTS compared with DIT-PTS for* $r = 2$ *at stage* $m - v = 5$ *and O-PTS with* $N = 256, 2048$.

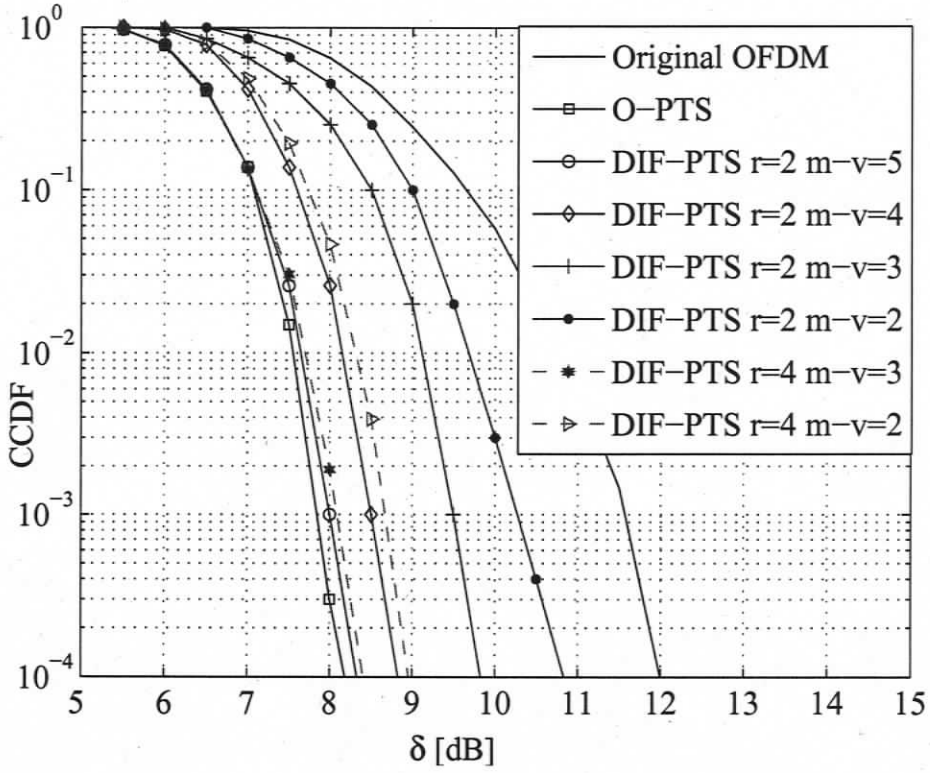

Figure 5.4. *CCDF of DIF-PTS radix-2 compared with DIF-PTS radix-4 for various numbers of remaining stages* $m - v$ *with* $N = 256$.

For $N = 2048$, a mixed radix with different r values is employed as $2048 = 2^1 4^5$. Figure 5.5 shows that radix-2 and mixed radix have similar PAPR reduction for $m - v = 5$ and $m - v = 3$, respectively. As shown in Table 5.3, a multiplicative complexity reduction of 59% and 83% is obtained by DIF-PTS mixed radix over radix-2 DIF-PTS and O-PTS, respectively. These results confirm that radix-4 has better PAPR performance per stage with a lower multiplicative complexity for the last $m - v$ stages compared to radix-2. A similar result can be obtained for DIT.

We consider only DIF in the rest of this thesis since as above shown, IFFT-based PTS using DIF requires fewer number of complex multiplications than DIT algorithms. In fact,

Table 5.3. *Multiplicative complexity reduction for radix-4 over radix-2 DIF-PTS with* $N = 256, 2048$, $P = 8$ *and similar CCDF.*

$r, m - v$	$R^{mul}(\%)$			
	Compared to DIF-PTS radix-2		Compared to O-PTS radix-2	
	$N = 256$	$N = 2048$	$N = 256$	$N = 2048$
2,5 and 4,3	21	59*	55	83*
2,4 and 4,2	43	68*	63	74*

*Mixed radix $r = 2, 4$

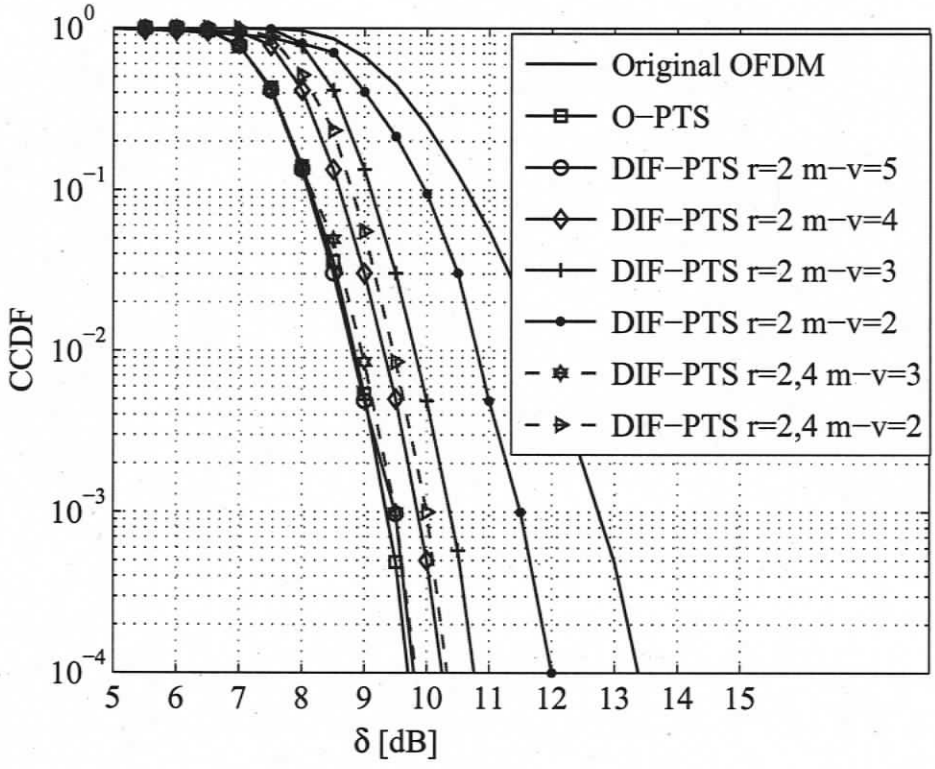

Figure 5.5. *CCDF of DIF-PTS radix-2 compared with DIF-PTS mixed-radix for various numbers of remaining stages* $m - v$ *with* $N = 2048$.

similar to radix-r DIF algorithm all the following IFFT-based PAPR reduction techniques can be developed for radix-r DIT algorithms as well.

5.1.1.4 Auto-correlation of the IFFT-based PTS subblocks

In PTS subblocking [27], a random subcarrier assignment improves the ACF properties of the PTS subblocks as it provides less correlated adjacent time samples compared with other partitioning schemes. This leads to better PAPR reduction with O-PTS. However, as will be shown, it is not the best approach for the case of IFFT-based PTS.

In order to design DIF-PTS subblocks for the inputs at stage v, we define the normalized periodic ACF of $x_p(n)$ as [27]

$$F_p(\xi) = \frac{1}{\sigma_x^2} E\left\{[x_p((n+\xi) \bmod N)][x_p(n)]^*\right\}. \tag{5.22}$$

This represents the correlation between ξ-spaced complex samples in subblock p. By substituting (5.5) into (5.8) and using this in (5.22) and taking the corresponding FFT, we obtain (for more detail see Appendix A)

$$F_p(\xi) = \frac{1}{\sigma_x^2 N^2} \sum_{\eta=1}^{r^{v-1}} \sum_{\tilde{n}=0}^{\frac{N}{r^v}-1} \sum_{i=0}^{r-1} E\left\{\tilde{y}_p^{\eta}\left(\tilde{n}+\frac{N}{r^v}i\right) \tilde{y}_p^{*\eta}\left(\tilde{n}+\frac{N}{r^v}i\right)\right\} T_{N/r^v}^{\tilde{n}\xi}. \tag{5.23}$$

where $\xi = 0, \ldots, N-1$. We introduce the variable $\bar{M}_{\tilde{n},i}^{\eta}$ with value one if $\tilde{y}$ is active in subblock p, and zero otherwise. Then, we can write (5.23) as

$$F_p(\xi) = \frac{1}{\sigma_x^2 N^2} \sum_{\eta=1}^{r^{v-1}} \sum_{\tilde{n}=0}^{\frac{N}{r^v}-1} \sum_{i=0}^{r-1} \bar{M}_{\tilde{n},i}^{\eta} T_{N/r^v}^{\tilde{n}\xi}. \tag{5.24}$$

We arrive at the following results from (5.23) and (5.24).

- The ACF vectors $F_p(\xi)$ are dependent on the active $\bar{M}_{\tilde{n},i}^{\eta}$ in subblock p and we should have PTS subblock partitioning based on the inputs $\tilde{y}^{\eta}(\tilde{n}+\frac{N}{r^v}i)$ associated with subblock p.

- If we increase the number of active M due to η, this increases the auto-correlation function for a particular subblock p and value $\widetilde{n}$, i.e., if all inputs over stage v are considered for subblocking, the twiddle factor $T_{N/r^v}^{\widetilde{n}\xi}$ (which corresponds to a particular subcarrier), is repeated in subblock p.

With O-PTS, pseudo-random [27] and M-sequence [53] subblocking has been done over all inputs $\widetilde{y}^{\eta}(\widetilde{n} + \frac{N}{r^v}i)$. The above analysis shows that these techniques can result in repeated subcarriers within a subblock. The corresponding ACF can be large when $m - v$ is small or N is large, i.e. if the number of identical N/r^{v-1}-point DFTs per stage is large.

In order to see the effect of repeated subcarriers on the ACF of the subblocks, consider $N = 32$, $v = 3$, $P = 4$, and $r = 2$ and the same pseudo-random sequence [01023312] over inputs $\widetilde{y}^{\eta}(\widetilde{n} + 4i)$ where $\eta = 1, \ldots, 4$, $i = 0, 1$, $\widetilde{n} = 0, \ldots, 7$, and $\widetilde{k} = 0, \ldots, 7$. In fact, there are 4×8-point DFTs at this stage. The effect of repeated subcarriers on the ACF is shown in Figure (5.6). We observe that repeated subcarriers results in a large ACF for the PTS sequences. This motivates us to propose a new subblocking technique.

5.1.1.5 Error-correcting code subblocking

We propose a technique using error-correcting codes (ECCs) to minimize the number of repeated subcarriers within the subblocks at stage v. Repetition codes (RCs) over Z_P, the integer ring of P elements, are used to generate a set of subblocks. Since the inputs at stage v have dimensions $r^{v-1} \times N/r^{v-1}$ (see (4.24)), the minimum number of subblocks should be $P_{min} = r^{v-1}$ in order to avoid repeated subcarriers. Hence, we construct ECC subblocks based on the two cases $r^{v-1} \leq N/r^{v-1}$ and $r^{v-1} > N/r^{v-1}$.

1) Case $r^{v-1} \leq N/r^{v-1}$: Let the vector $\mathbf{s} = [s_0, s_1, \ldots, s_\eta, \ldots, s_{r^{v-1}-1}]$ of elements over $\mathcal{Z}_{r^{v-1}}$, the integers modulo r^{v-1}, represent the inputs to the N/r^{v-1}-point DFTs. We

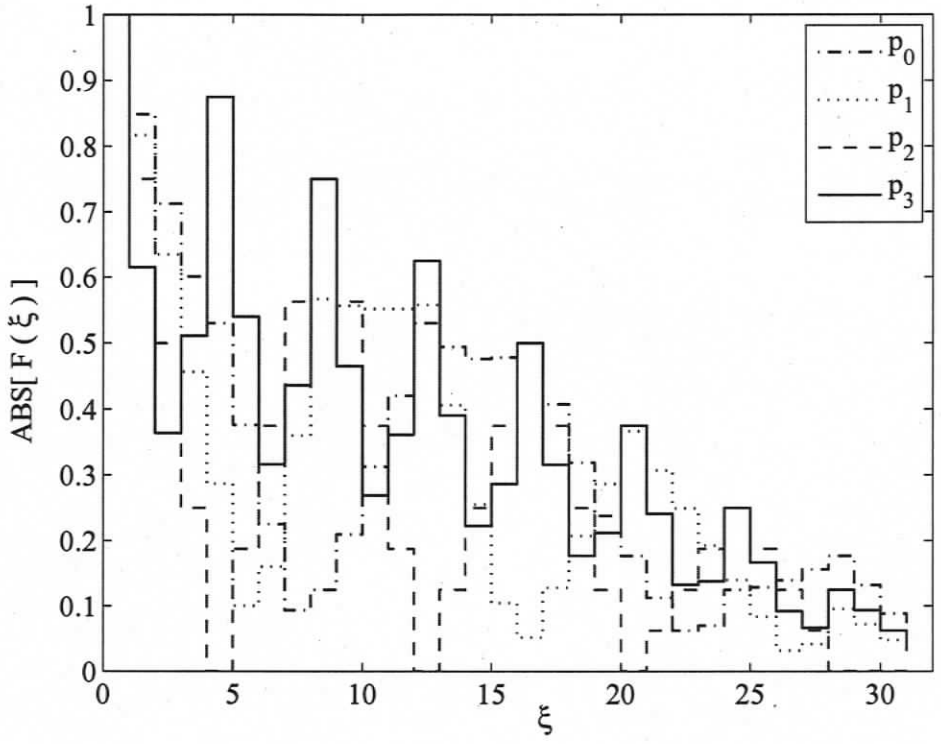

Figure 5.6. *The auto-correlation of PTS sequences in a PTS radix FFT for* $N = 32$, $v = 3$, $P = 4$ *and* $r = 2$ *with repeated subcarriers within each subblock.*

repeat each element within the sequence $\mathbf{s}$ N/r^{v-1} times. Then, we obtain matrix $\widehat{\mathbf{S}}$

$$\widehat{\mathbf{S}} = \begin{bmatrix} \widehat{\mathbf{s}}_0 \\ \widehat{\mathbf{s}}_1 \\ \vdots \\ \widehat{\mathbf{s}}_\eta \\ \vdots \\ \widehat{\mathbf{s}}_{r^{v-1}-1} \end{bmatrix} = \begin{bmatrix} s_0 & s_0 & \cdots & s_0 \\ s_1 & s_1 & \cdots & s_1 \\ \vdots & \vdots & \ddots & \vdots \\ s_\eta & s_\eta & \cdots & s_\eta \\ \vdots & \vdots & \ddots & \vdots \\ s_{r^{v-1}-1} & s_{r^{v-1}-1} & \cdots & s_{r^{v-1}-1} \end{bmatrix} \tag{5.25}$$

with dimensions $r^{v-1} \times N/r^{v-1}$. Next, we generate a pseudo-random sequence $\Psi = \left[\psi_0, \psi_1, \ldots, \psi_{(\tilde{n}+\frac{N}{r^v}i)}, \ldots, \psi_{\frac{N}{r^{v-1}}-1}\right]$ of length N/r^{v-1} over $\mathcal{Z}_{r^{v-1}}$. Finally, we construct the codewords as

$$\mathcal{R}_{ECC} = \begin{bmatrix} \Psi + \widehat{S}_0 (\mathrm{mod} P) \\ \Psi + \widehat{S}_1 (\mathrm{mod} P) \\ \vdots \\ \Psi + \widehat{S}_\eta (\mathrm{mod} P) \\ \vdots \\ \Psi + \widehat{S}_{r^{v-1}-1} (\mathrm{mod} P) \end{bmatrix}. \tag{5.26}$$

These codeword have *maximum Hamming distance* N/r^{v-1} as they differ in all positions. Each row in matrix $\mathcal{R}_{ECC}$ represents the inputs to N/r^{v-1}-point DFTs.

2) Case $r^{v-1} > N/r^{v-1}$: We construct the $\mathcal{R}_{ECC}$ with dimensions $N/r^{v-1} \times r^{v-1}$ and then take the transpose of $\mathcal{R}_{ECC}$ to obtain the codeword matrix $\widehat{\mathcal{R}}_{ECC}$ with dimensions $r^{v-1} \times N/r^{v-1}$. Consider the vector $\mathbf{s} = \left[s_0, s_1, \ldots, s_{(\tilde{n}+\frac{N}{r^v}i)}, \ldots, s_{\frac{N}{r^{v-1}}-1}\right]$ over $\mathcal{Z}_{N/r^{v-1}}$ and repeat each element within $\mathbf{s}$ r^{v-1} times. This results in a matrix $\widehat{\mathbf{S}}$ with dimensions $N/r^{v-1} \times r^{v-1}$. A pseudo-random sequence $\Psi = [\psi_0, \psi_1, \ldots, \psi_\eta, \ldots, \psi_{r^{v-1}-1}]$ without repeated elements of length r^{v-1} is generated over $\mathcal{Z}_{r^{v-1}}$. From (5.26), the codeword matrix $\mathcal{R}$ is obtained with dimensions $N/r^{v-1} \times r^{v-1}$. Finally, we obtain $\widehat{\mathcal{R}}_{ECC}$ by taking the transpose of $\mathcal{R}$.

As an example, consider DIF radix-2 for a 32-point FFT. We first let $v = 3$, which corresponds to Case 1 as there are 4×8-point DFTs. The M-sequence (MS) subblocking

from [53] with $P = 4$ is

$$\mathcal{R}_{MS} = \begin{bmatrix} 0 & 2 & 3 & 1 & 2 & 1 & 0 & 2 \\ 1 & 0 & 0 & 0 & 2 & 1 & 2 & 1 \\ 2 & 3 & 3 & 1 & 2 & 3 & 1 & 0 \\ 0 & 2 & 3 & 3 & 3 & 3 & 1 & 0 \end{bmatrix}. \tag{5.27}$$

As seen from (5.27), there are as many as three repeated subcarriers within the subblocks. With our proposed technique using an error-correcting code (ECC) over $\mathcal{Z}_4$, we employ $\Psi = [01023312]$ and

$$\widehat{\mathbf{S}} = \begin{bmatrix} 0 & 0 & 0 & 0 & 0 & 0 & 0 & 0 \\ 1 & 1 & 1 & 1 & 1 & 1 & 1 & 1 \\ 2 & 2 & 2 & 2 & 2 & 2 & 2 & 2 \\ 3 & 3 & 3 & 3 & 3 & 3 & 3 & 3 \end{bmatrix} \tag{5.28}$$

to obtain

$$\mathcal{R}_{ECC} = \begin{bmatrix} 0 & 1 & 0 & 2 & 3 & 3 & 1 & 2 \\ 1 & 2 & 1 & 3 & 0 & 0 & 2 & 3 \\ 2 & 3 & 2 & 0 & 1 & 1 & 3 & 0 \\ 3 & 0 & 3 & 1 & 2 & 2 & 0 & 1 \end{bmatrix} \tag{5.29}$$

which has no repeated subcarriers within the subblocks. Figures 5.7 and 5.8 present the absolute value of the ACF vectors for subblocks p_0 to p_4 with MS and ECC subblocks. The ECC subblocks show a significant reduction in the ACF with $\xi \neq 0$ in comparison with MS subblocking. ECC subblocking provides an ACF which is nearly flat. If $v = 4$ is taken, i.e., 8×4-point DFTs, we have Case 2 subblocking. MS subblocking [53] with P=8 has

$$\mathcal{R}_{MS} = \begin{bmatrix} 0 & 2 & 1 & 2 & 6 & 6 & 4 & 7 \\ 6 & 1 & 0 & 5 & 7 & 3 & 6 & 3 \\ 3 & 4 & 0 & 2 & 3 & 1 & 7 & 1 \\ 5 & 2 & 4 & 5 & 5 & 0 & 7 & 4 \end{bmatrix} \tag{5.30}$$

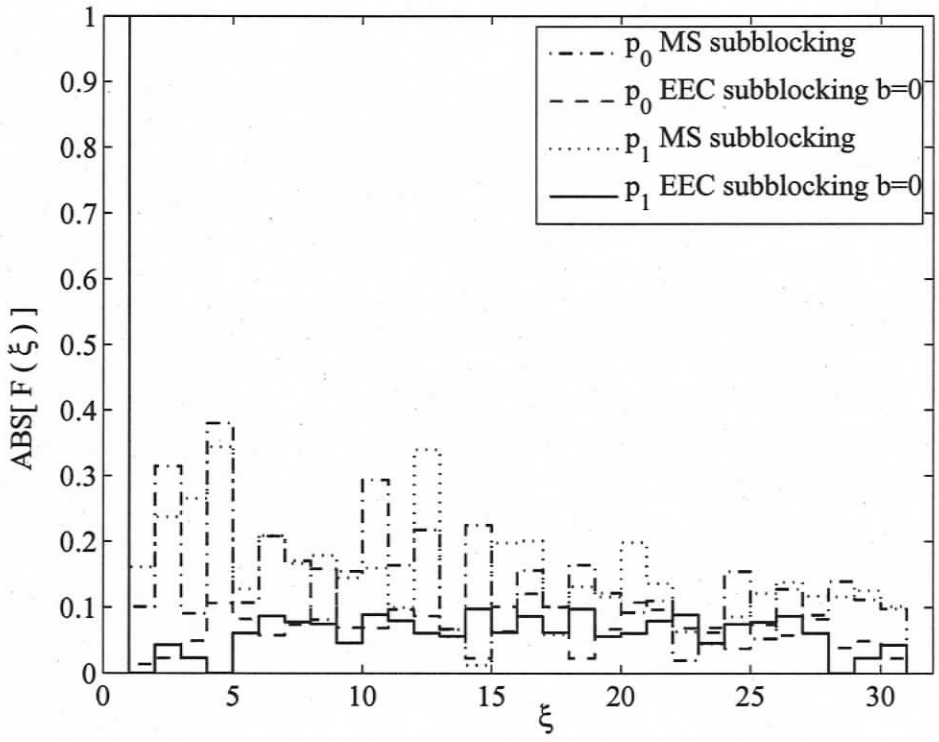

Figure 5.7. *The auto-correlation of PTS sequences in an IFFT-based PTS for* $N = 32$, $v = 3$, $P = 4$, $r = 2$, $b = 0$, *M-sequence and ECC subblocks,* p_0 *and* p_1.

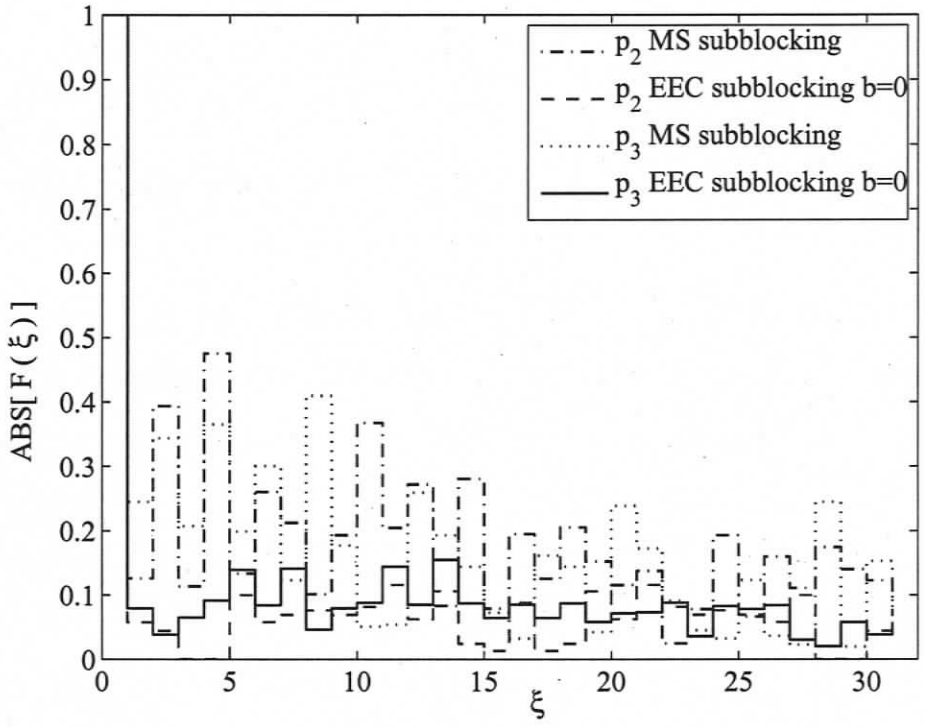

Figure 5.8. *The auto-correlation of PTS sequences in an IFFT-based PTS FFT for* $N = 32$, $v = 3$, $P = 4$, $r = 2$, $b = 0$, *M-sequence and ECC subblocks,* p_2 *and* p_3.

whereas ECC subblocking over $\mathcal{Z}_8$ with $\Psi = [01467352]$ gives

$$\widehat{\mathcal{R}}_{ECC} = \begin{bmatrix} 0 & 1 & 4 & 6 & 7 & 3 & 5 & 2 \\ 1 & 2 & 5 & 7 & 0 & 4 & 6 & 3 \\ 2 & 3 & 6 & 0 & 1 & 5 & 7 & 4 \\ 3 & 4 & 7 & 1 & 2 & 6 & 0 & 5 \end{bmatrix}^T . \tag{5.31}$$

The minimum number of subblocks $P_{min} = r^{v-1}$ is typically large when the number of multiple stages, $m - v$, is small. This increases the number of multiple IFFTs and the search complexity for the optimal phases. In this case, it is possible to reduce the number of subblocks by using a higher radix such as radix-4. Table 5.4 summarizes the minimum number of subblocks to achieve maximum Hamming distance within the ECC subblocks for different values of N and r. To eliminate the repeated subblocks, $P \geq 32$ is required with $m - v = 2$ and $N \geq 512$, or $m - v = 3$ and $N \geq 2048$. However, a small number of repeated subcarriers can still provide reasonable PAPR reduction.

Let $P = r^{v-1}/2^b$ be the number of subblocks with repeated subcarriers where $b = 1, \ldots, (v-1)\log_2(r-1)$. There are no repeated subcarriers for $b = 0$.

3) Case $r^{v-1} \leq N/r^{v-1}$ and $b \geq 1$: We define the vector $\mathbf{s}$ over $\mathcal{Z}_{r^{v-1}/2^b}$. The matrix $\widehat{\mathbf{S}}$ is obtained similar to (5.25). In order to have the sequence Ψ, we can generate 2^b random sequences Ψ of length N/r^{v-1} over $\mathcal{Z}_{r^{v-1}}/2^b$. The codeword matrix $\mathcal{R}$ is obtained from (5.26). The number of repeated elements within vector $\mathbf{s}$ is 2^{b-1}.

4) Case $r^{v-1} > N/r^{v-1}$ and $b \geq 1$: This is similar to the case 2 over $\mathcal{Z}_{r^{v-1}}/2^b$.

Consider the above example for $b = 1$. With $v = 4$ and $b = 1$ (Case 4), the number of subblocks is reduced from 8 to 4. Matrix $\widehat{\mathcal{R}}_{ECC}$ over $\mathcal{Z}_4$ is

$$\widehat{\mathcal{R}}_{ECC} = \begin{bmatrix} 0 & 3 & 1 & 0 & 2 & 1 & 3 & 2 \\ 1 & 3 & 2 & 0 & 3 & 1 & 0 & 2 \\ 1 & 0 & 2 & 1 & 3 & 2 & 0 & 3 \\ 2 & 0 & 3 & 1 & 0 & 2 & 1 & 3 \end{bmatrix}^T . \tag{5.32}$$

The magnitude of the ACF vectors for ECC subblocks is depicted in Figure 5.9. This shows

Table 5.4. *The number of subblocks for various numbers of repeated twiddle factors and FFT sizes with* $r = 2, 4$ *and* $m - v = 2, 3$.

N	$m-v=2$					
	$r=2, P_{min}$			$r=4, P_{min}$		
	$b=0$	$b=1$	$b=2$	$b=0$	$b=1$	$b=2$
32	8	4	2	2	<2	<2
64	16	8	4	4	2	<2
128	>16	16	8	8	4	2
256	>16	>16	16	16	8	4
512	>16	>16	>16	>16	16	8
1024	>16	>16	>16	>16	>16	16
2048	>16	>16	>16	>16	>16	>16

N	$m-v=3$					
	$r=2, P_{min}$			$r=4, P_{min}$		
	$b=0$	$b=1$	$b=2$	$b=0$	$b=1$	$b=2$
32	4	2	<2	<2	<2	<2
64	8	4	2	<2	<2	<2
128	16	8	2	2	<2	<2
256	>16	16	8	4	2	<2
512	>16	>16	16	8	4	2
1024	>16	>16	>16	16	8	4
2048	>16	>16	>16	>16	16	8

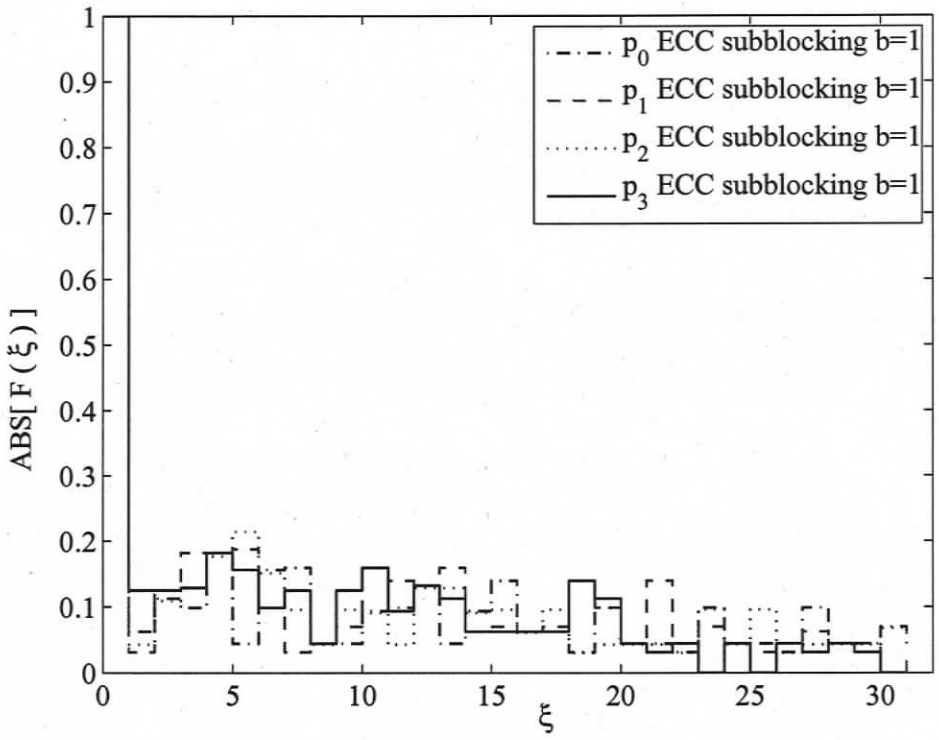

Figure 5.9. *The auto-correlation of PTS sequences in an IFFT-based PTS for* $N = 32$, $v = 4$, $P = 4$, $r = 2$, $b = 1$, *and ECC subblocks,* p_0, p_1, p_2, *and* p_3.

that even with repeated subcarriers ($b = 1$), the proposed ECC subblocking provides low auto-correlation PTS sequences. If we consider Case 3 with $v = 3$, the number of subblocks is reduced from 4 to 2. The ECC subblocking over $\mathcal{Z}_2$ with two random sequences $\Psi_1 = [10011100]$ and $\Psi_2 = [00111001]$ is

$$\mathcal{R}_{ECC} = \begin{bmatrix} 1 & 0 & 0 & 1 & 1 & 1 & 0 & 0 \\ 0 & 1 & 1 & 0 & 0 & 0 & 1 & 1 \\ 0 & 0 & 1 & 1 & 1 & 0 & 0 & 1 \\ 1 & 1 & 0 & 0 & 0 & 1 & 1 & 0 \end{bmatrix}^T. \tag{5.33}$$

With MS subblocking [53], we have

$$\mathcal{R}_{MS} = \begin{bmatrix} 0 & 1 & 1 & 0 & 1 & 0 & 0 & 1 \\ 0 & 0 & 0 & 0 & 1 & 0 & 1 & 0 \\ 1 & 1 & 1 & 0 & 1 & 1 & 0 & 0 \\ 0 & 1 & 1 & 1 & 1 & 1 & 0 & 0 \end{bmatrix}^T. \tag{5.34}$$

From (5.33) and (5.34), the number of repeated subcarriers within subblocks using ECC is reduced compared to MS subblocking.

5) Performance results: We first discuss the tradeoffs between the number of subblocks, multiplicative complexity, number of repeated subcarriers, and PAPR reduction. Then, the performance of IFFT-based PTS using ECC subblocking (PTS-ECC) is examined and compared with O-PTS [27] and PTS using M-sequences (PTS-MS) [53].

- Tradeoffs in a PTS-ECC: A high number of subblocks increases the search complexity for the optimal phases with PTS and also the number of transforms. Therefore, we limit this number to $P_{max} = 16$. As seen in Table 5.4, we can reduce this number by using a higher value of r while still minimizing the number of repeated subcarriers. Another advantage of a higher radix is lower multiplicative complexity compared to using a smaller radix. As discussed in Chapter 4, If we employ radix-8, the number of subblocks is significantly reduced, but they become complex to implement. As a consequence, we choose $r = 4$ which provides low multiplicative complexity,

low hardware complexity, and a suitable number of subblocks, i.e., a sufficiently low number of transforms. If very low complexity for the transforms is required, such as with $m-v=2$, PTS sequences with perfect ACF properties ($b=0$) can be obtained for $32 \leq N < 512$. However, for $N \geq 512$, there is a tradeoff between PAPR reduction, number of transforms, and number of subblocks. This will be examined next.

- PAPR performance: The CCDF of the PAPR of 16 QAM-modulated OFDM signals is considered with $P=16$. When $N \neq 4^m$, a mixed-radix of 2 and 4 are used. For simplicity, we consider only $256 \leq N \leq 2048$, as the results for $32 \leq N < 256$ are similar to the case with $N=256$. For $N > 2048$, we require $P > 16$ in order to improve the PAPR. We compare the CCDF of O-PTS [27], with PTS-MS [53] and PTS-ECC. The PAPR improvements are summarized in Table 5.5. for $CCDF = 10^{-4}$.

  Figure 5.10 presents the PAPR performance for $N=256$. This shows that PTS-ECC improves the PAPR performance by approximately 2 dB for $m-v=2$ and 2.2 dB for $m-v=3$, compared to PTS-MS. The results for $N=512$ are shown in Figure 5.11. With $P=16$ and $m-v=2$, there is a negligible degradation in PAPR performance with $b=1$ compared to the case for $b=0$. The PAPR improvement is 1.8 dB for $m-v=2$ and 1.6 dB for $m-v=3$ compared to PTS-MS.

  The performance with $N=1024$ is given in Figure 5.12. In this case, the PAPR performance with $b=1$ and $m-v=2$ is similar to that with $b=0$ and $m-v=2$. There is also 1.5 to 1.6 dB PAPR improvement compared to PTS-MS. However, with $b=2$, the performance improvement becomes insignificant.

  The CCDF of the OFDM signals using $N=2048$ with $b=1$ and $m-v=3$ is shown in Figure 5.13. The PAPR reduction is 1.5 dB better than with PTS-MS. For $m-v=2$, the number of subblocks is $P > 16$, so this case is not considered.

  The numerical results presented verify the analysis in Section 5.1.1.4. ECC subblocking with $b=1$ provides the best trade-off between PAPR reduction, number of

Table 5.5. *Comparison of PTS-ECC, O-PTS [27] and PTS-MS in terms of PAPR improvement for* $256 \leq N \leq 2048$, *CCDF*=10^{-4}, *and* $m - v = 2, 3$.

	$m - v = 2$	
N	PTS-ECC compared to PTS-MS PAPR improvement (dB)	PTS-ECC compared to O-PTS PAPR loss (dB)
256	2	1.2
512	1.9[1]	1.3[1]
1024	1.5[1]	1.6
2048	*	*
	$m - v = 3$	
N	PTS-ECC compared to PTS-MS PAPR improvement (dB)	PTS-ECC compared to O-PTS PAPR loss (dB)
256	2.2	0.1
512	1.6	0.2
1024	1.6[1]	0.3
2048	1.5	0.2

[1] $b = 1$

* $P > 16$

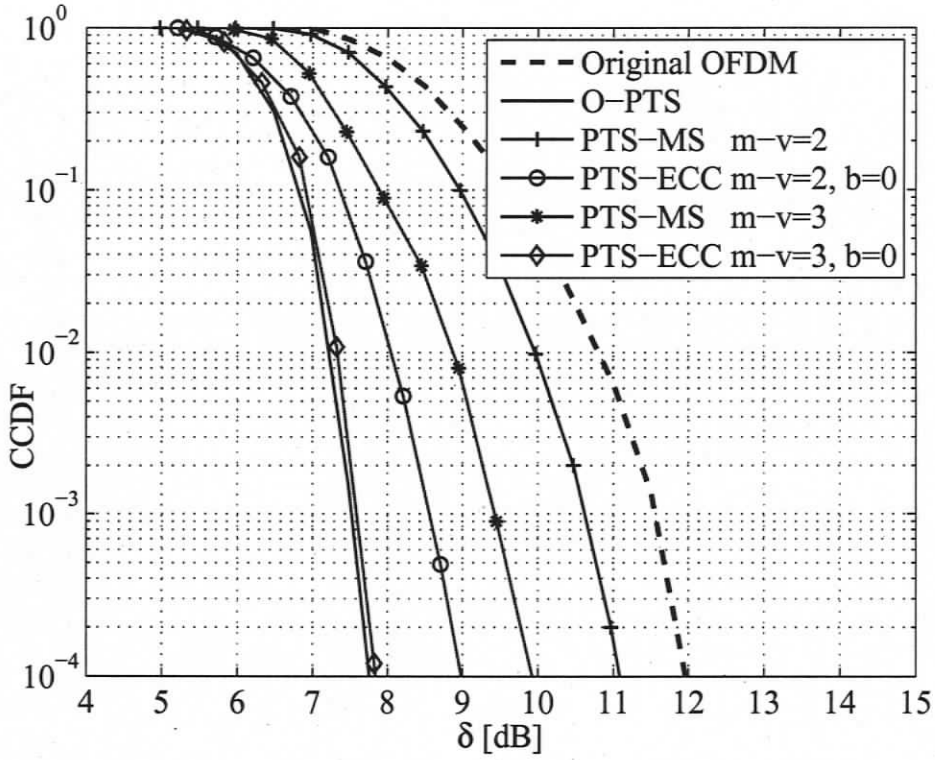

Figure 5.10. *CCDF of PTS-ECC in comparison with PTS-MS and O-PTS with* $m - v = 2$ *and* $m - v = 3$ *for N=256.*

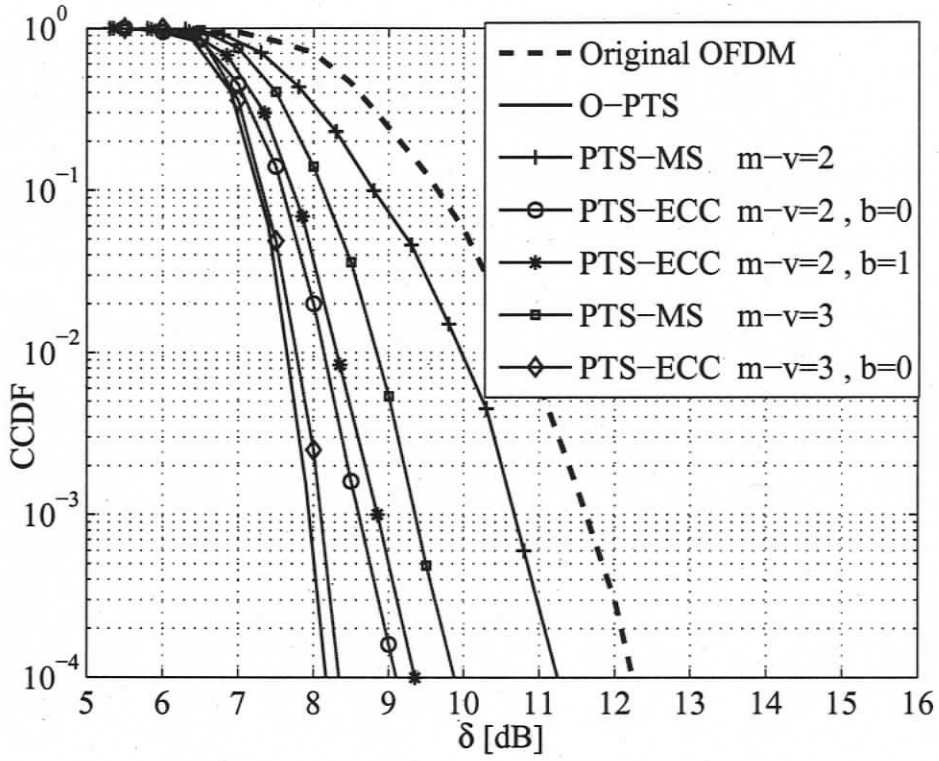

Figure 5.11. *CCDF of PTS-ECC in comparison with PTS-MS and O-PTS, with* $m-v=2$ *and* $m-v=3$ *for N=512.*

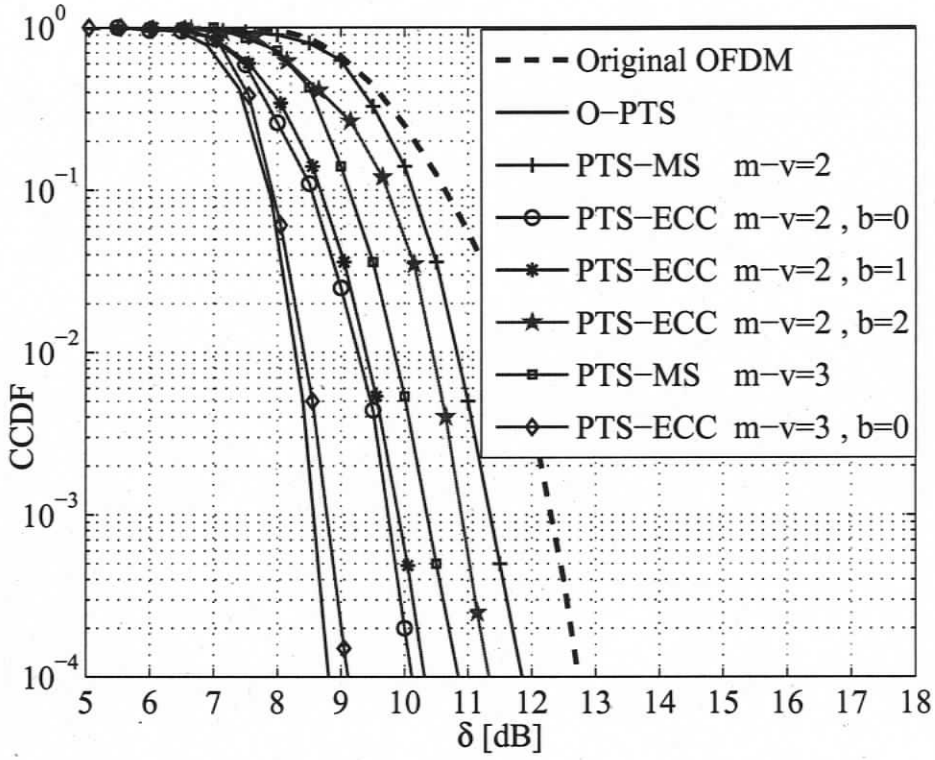

Figure 5.12. *CCDF of PTS-ECC in comparison with PTS-MS and O-PTS, with* $m-v=2$ *and* $m-v=3$ *for N=1024.*

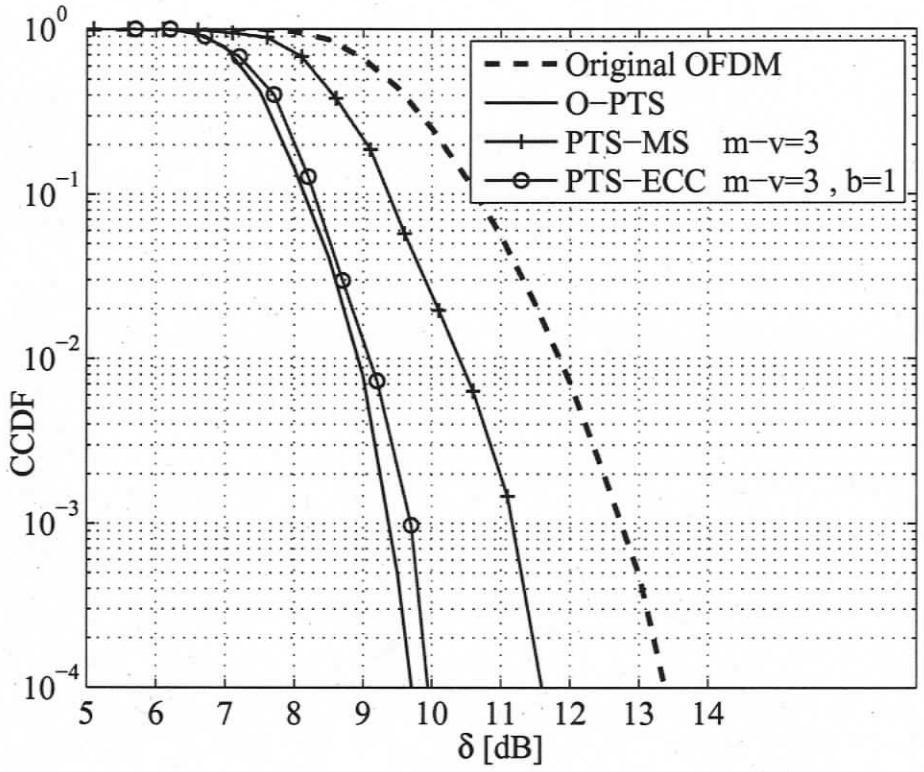

Figure 5.13. *CCDF of PTS-ECC in comparison with PTS-MS and O-PTS, with* $m - v = 2$ *and* $m - v = 3$ *for N=2048.*

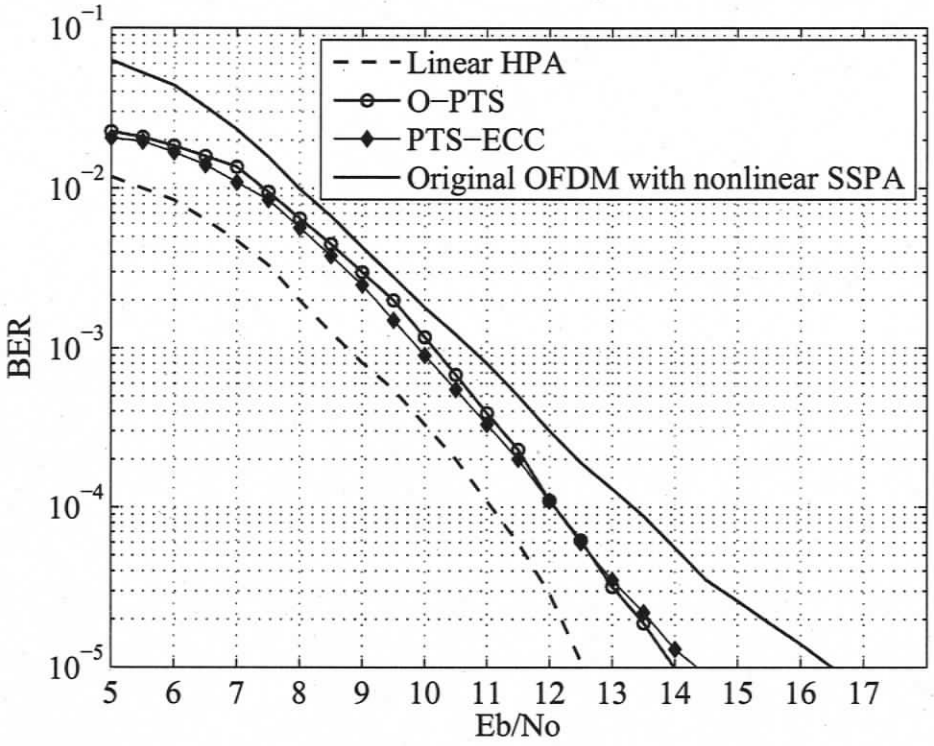

Figure 5.14. *BER versus E_b/N_0 for OFDM systems using O-PTS and PTS-RC with $m - v = 3$, $N = 256$, and $P = 16$ in the presence of an HPA nonlinearity with OBO = 5 dB.*

subblocks, and number of transforms for $512 \leq N < 4095$. For $32 \leq N < 512$, the best PAPR considering the number of transforms is achieved with $b = 0$.

- BER performance: We evaluate the BER of OFDM signals distorted by an SSPA type of HPA nonlinearity. An AWGN channel is employed. We use an SSPA with typical parameters $h = 1$, $A = 1$, and $\epsilon = 10$ [42]. The SSPA OBO is set to 5 dB. We consider $N = 256$ and $m - v = 3$. Similar results can be obtained for other values of N. The other parameters are the same as the previous simulations. Figure 5.14 shows that both PTS-ECC and O-PTS improve the performance by almost 2 dB at BER=10^{-5}.

As mentioned earlier in Chapter 4, the outputs and inputs to each FFT stage are accessible. Therefore, It is important to note that the PTS subblock design in this thesis can be practically implemented within the FFT of OFDM transceivers. We can use hardware devices such as a Field Programmable Gate Array (FPGA) or a digital signal processor (DSP) [83] to implement this FFT-based PAPR reduction technique. The implementation requires fewer hardware resources than other techniques, and only a small number of transforms are needed to provide near optimal performance.

It should be emphasized that the PTS-ECC subblocks are designed once (offline), and therefore, they do not add any complexity to the system. Since these locations are predetermined for the receiver, this technique requires the same side information as O-PTS [27] and MS subblocking [53]. In addition, the values r and v are fixed based on the required tradeoff between complexity and PAPR reduction.

5.2 SLM and the Common FFT Algorithms

Similar to PTS, a major limitation of SLM is the computation of multiple IFFTs, resulting in a high complexity for practical systems which is proportional to the number of SLM sequences. This complexity can be reduced with IFFT-based SLM which uses the product of intermediate signals within the IFFT and the SLM phase sequences. Multiple IFFTs are then applied to the remaining stages.

To reduce the computational complexity of the remaining stages, IFFT-based SLM using DIF rather than DIT obviously provides the lower multiplicative complexity. In addition (similar to PTS), IFFT-based SLM using a high radix common FFT algorithm results in lower multiplicative complexity than using a lower radix. The only comparison remaining is PAPR performance, and this will be provided by simulation.

To further reduce the computational complexity of IFFT-based SLM, we propose a technique where multiple IFFTs are computed over a fraction of the identical IDFTs for the remaining stages. It is shown that this approach significantly lowers the computational

complexity compared to IFFT-based SLM and original SLM for typical numbers of SLM sequences.

5.2.1 IFFT-based SLM

To derive the IFFT-based SLM technique using a radix-r DIF algorithm (DIF-SLM), a phase rotated version of the inputs $\widetilde{\mathbf{y}}_\eta$ using (4.25) and (4.24) is employed

$$\mathbf{U}_\omega^\eta = \widetilde{\mathbf{y}}^\eta \bullet e^{j\Phi_\omega^\eta}$$

$$\bar{\mathbf{U}}_\omega = \begin{bmatrix} \mathbf{U}_\omega^1 \\ \mathbf{U}_\omega^2 \\ \vdots \\ \mathbf{U}_\omega^\eta \\ \vdots \\ \mathbf{U}_\omega^{r^{v-1}} \end{bmatrix} = \begin{bmatrix} \widetilde{\mathbf{y}}^1 \\ \widetilde{\mathbf{y}}^2 \\ \cdots \\ \widetilde{\mathbf{y}}^\eta \\ \cdots \\ \widetilde{\mathbf{y}}^{r^{v-1}} \end{bmatrix}^T \begin{bmatrix} e^{j\Phi_\omega^1} \\ e^{j\Phi_\omega^2} \\ \vdots \\ e^{j\Phi_\omega^\eta} \\ \vdots \\ e^{j\Phi_\omega^{r^{v-1}}} \end{bmatrix} \tag{5.35}$$

where

$$\mathbf{U}_\omega^\eta = \left[U_\omega^\eta(0), U_\omega^\eta(1), \ldots, U_\omega^\eta(\widetilde{n} + \frac{N}{r^v}i), \ldots, U_\omega^\eta(\frac{N}{r^{v-1}} - 1)\right]_{N/r^{v-1}}, \tag{5.36}$$

$$\widetilde{\mathbf{y}}^\eta = \left[\widetilde{y}^\eta(0), \widetilde{y}^\eta(1), \ldots, \widetilde{y}^\eta(\widetilde{n} + \frac{N}{r^v}i), \ldots, \widetilde{y}^\eta(\frac{N}{r^{v-1}} - 1)\right]_{N/r^{v-1}}, \tag{5.37}$$

and

$$\Phi_\omega^\eta = \left[\phi_\omega^\eta(0), \phi_\omega^\eta(1), \ldots, \phi_\omega^\eta(\widetilde{n} + \frac{N}{r^v}i), \ldots, \phi_\omega^\eta(\frac{N}{r^{v-1}} - 1)\right]_{N/r^{v-1}}. \tag{5.38}$$

The time-domain OFDM signal $u_\omega(n)$ can be obtained by taking the DFT of $U_w^\eta(\widetilde{n})$ according to (5.5) for the $m - v$ stages remaining in the transform. Finally, the lowest PAPR sequence $u_{\omega'}(n)$ is selected for transmission.

In order to recover the data at the receiver, similar to IFFT-based PTS we must take into account the IFFT input order at the transmitter. As a consequence, if stage v is used to multiply the phase sequences, the data is recovered at stage $m - v$ at the receiver. Hence, the side information remains the same as with original SLM (O-SLM).

A similar approach to radix-r DIF algorithms (from (4.27), (4.28), and (5.13)) can be employed to obtain IFFT-based SLM using radix-r DIT (DIT-SLM).

5.2.1.1 DIF-SLM versus DIT-SLM

The CCDF of the PAPR of 16-QAM modulated OFDM signals with $\Omega = 8$ and $r = 2$ is considered in this section. An oversampling factor of 4 [55] is used. For simplicity, we consider $N = 2048$ as similar results can be obtained for other values of N. The PAPR reduction performance is examined. Figure 5.15 shows that DIF-SLM has the same PAPR performance as DIT-SLM with $m - v = 5$ and 8 SLM sequences ($\Omega = 8$). However, DIF-SLM achieves a multiplicative complexity reduction of 30% over DIT-SLM. This value increases to 58% when compared to O-SLM, as shown in Table 5.2.

5.2.1.2 Varying r

Similar to PTS, we select $r = 4$ as a higher radix to compare with $r = 2$. As 2048 is not a power of 4, a mixed radix is employed. For the first stage, radix-2 is used while for the two remaining 1024-point DFTs, radix-4 is employed. Figure 5.16 shows that radix-2 and mixed radix have similar PAPR reduction with $m - v = 5$ and $m - v = 3$, respectively. From Table 5.3, a multiplicative complexity reduction of 59% and 83% is obtained with DIF-SLM mixed radix over radix-2 and O-SLM, respectively. These results confirm that radix-4 provides better PAPR performance per stage with a lower multiplicative complexity for the remaining stages compared to radix-2.

5.2.1.3 Partial selective mapping

Taking into account practical FFT implementations [85], the inputs $\widetilde{y}^{\eta}(\widetilde{n} + \frac{N}{r^v}i)$ to the ηth N/r^{v-1}-point DFT can be divided into r data blocks of size N/r^v. Then, the butterfly computations can be done in N/r^v sample intervals assuming that the butterfly computation time is equal to the sampling interval. This is done for all N/r^{v-1}-point DFTs at stage v

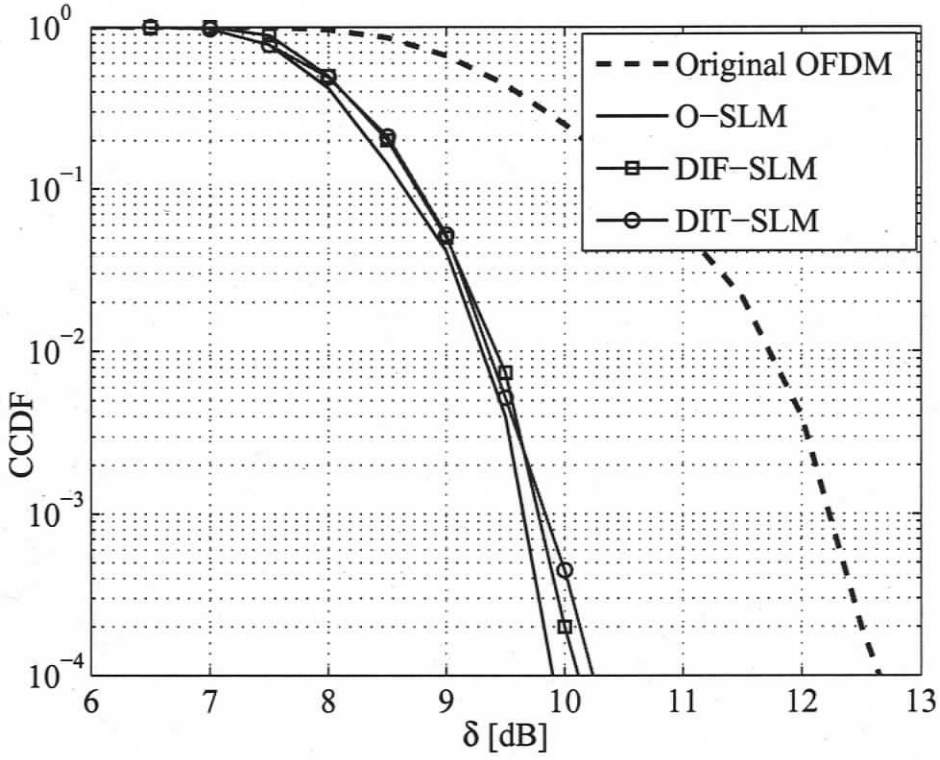

Figure 5.15. *CCDF of DIF-SLM radix-2 compared with DIT-SLM radix-2 at stage* $m - v = 5$ *and O-SLM with* $N = 2048$ *and* $\Omega = 8$.

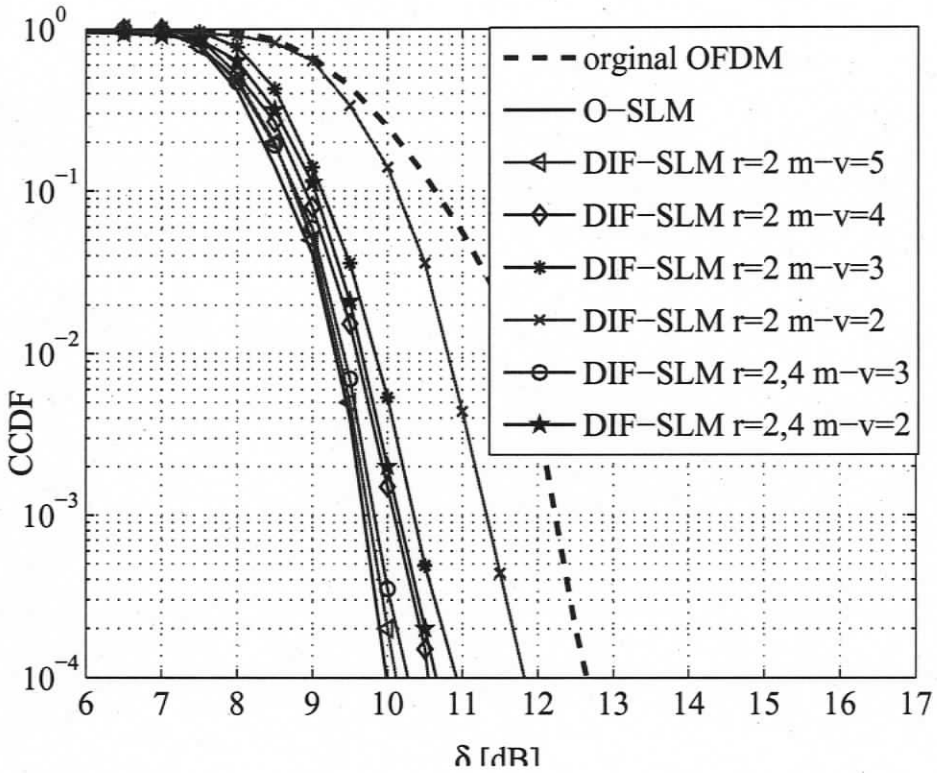

Figure 5.16. *CCDF of DIF-SLM radix-2 compared with DIF-SLM mixed-radix for various numbers of remaining stages* $m - v = 5$ *with* $N = 2048$ *and* $\Omega = 8$.

by means of appropriate delays and switching times. With IFFT-based SLM at stage v, this requires r^{v-1} N/r^{v-1}-point DFTs to be computed for each SLM sequence $u_m(n)$.

Conversely to IFFT-based SLM, we propose partial SLM sequences (P-SLM) where the time-domain SLM sequence $u_m(n)$ are computed over a fraction of the $r^{v-1} \times N/r^{v-1}$-point DFTs. In another words, a subsets of the $\mathbf{U}_\omega^\eta$ are phase rotated to obtain $u_m(n)$. Let ν denote the number of subsets of N/r^{v-1}-point DFTs where $\nu \leq \Omega$, $2 \leq \nu < r^{v-1}$, and ν is a power of 2 ($\nu = 2^0$ when there are no partial subsets). We first consider ν randomly constructed subsets. Then theses time-domain subsets can be combined to obtain new SLM sequences.

1) Partial subsets: The random selection of the DFTs is done using the following steps.

1. Construct a pseudo-random sequence of length r^{v-1} over $\mathcal{Z}_\nu$, the integers modulo ν

$$\Psi = [\psi_0\, \psi_1\, \ldots, \psi_\eta, \ldots, \psi_{r^{v-1}-1}] \tag{5.39}$$

   where ψ_η corresponds to the phase rotated sequence $\mathbf{U}_\omega^\eta$ in (5.35).

2. Obtain

$$\begin{aligned}
\Psi^0 &= \Psi \\
\Psi^1 &= \Psi^0 + \nu I \bmod \Omega \\
&\vdots \\
\Psi^{\bar{l}+1} &= \Psi^{\bar{l}} + \nu I \bmod \Omega \qquad (5.40) \\
&\vdots \\
\Psi^{\frac{\Omega}{\nu}-1} &= \Psi^{\frac{\Omega}{\nu}-2} + \nu I \bmod \Omega, \qquad (5.41)
\end{aligned}$$

I is the identity vector, and $0 \leq \bar{l} \leq \frac{\Omega}{\nu} - 1$. Hence, the $\mathcal{S}$ can be expressed as

$$\mathcal{S} = \begin{bmatrix} \Psi^1 \\ \Psi^2 \\ \vdots \\ \Psi^{\bar{l}} \\ \vdots \\ \Psi^{\frac{\Omega}{\nu}} \end{bmatrix} = \begin{bmatrix} \psi_1^1 & \psi_2^1 & \dots & \psi_\eta^1 & \dots & \psi_{r^{v-1}}^1 \\ \psi_1^2 & \psi_2^2 & \dots & \psi_\eta^2 & \dots & \psi_{r^{v-1}}^2 \\ \vdots & \vdots & \ddots & \vdots & \vdots & \vdots \\ \psi_1^{\bar{l}} & \psi_2^{\bar{l}} & \dots & \psi_\eta^{\bar{l}} & \dots & \psi_{r^{v-1}}^{\bar{l}} \\ \vdots & \vdots & \vdots & \vdots & \ddots & \vdots \\ \psi_1^{\frac{\Omega}{\nu}} & \psi_2^{\frac{\Omega}{\nu}} & \dots & \psi_\eta^{\frac{\Omega}{\nu}} & \dots & \psi_{r^{v-1}}^{\frac{\Omega}{\nu}} \end{bmatrix} \tag{5.42}$$

where each row of $\mathcal{S}$ corresponds to ν SLM sequences. Each element $\psi_{\bar{l}}^{\eta}$ denotes the location of the ηth DFT which is randomly selected. Note that the first sequence corresponds to the original sequence which is not rotated so it is computed over all r^{v-1}-point DFTs.

Example 1: consider $N = 32$, $v = 4$, $r = 2$, $\Omega = 4$, and $\nu = 2$. We generate $\Psi = [01001110]$ over $\mathcal{Z}_2$ and obtain

$$\mathcal{S} = \begin{bmatrix} 0 & 1 & 0 & 0 & 1 & 1 & 1 & 0 \\ 2 & 3 & 2 & 2 & 3 & 3 & 3 & 2 \end{bmatrix}. \tag{5.43}$$

Assume zero corresponds to the original data which is computed over all r^{v-1} DFTs. From (5.43), the 4 phase rotated sequences are

$$\begin{aligned} \bar{\mathbf{U}}_0 &= \left[\mathbf{U}_0^1\, \mathbf{U}_0^2\, \mathbf{U}_0^3\, \mathbf{U}_0^4\, \mathbf{U}_0^5\, \mathbf{U}_0^6\, \mathbf{U}_0^7\, \mathbf{U}_0^8\right]^T, \\ \bar{\mathbf{U}}_1 &= \left[\mathbf{U}_1^1\, \mathbf{U}_1^2\, \mathbf{U}_1^3\, \mathbf{U}_1^4\, \mathbf{U}_1^5\, \mathbf{U}_1^6\, \mathbf{U}_1^7\, \mathbf{U}_1^8\right]^T, \\ \bar{\mathbf{U}}_2 &= \left[\mathbf{U}_2^1\, \mathbf{U}_2^2\, \mathbf{U}_2^3\, \mathbf{U}_2^4\, \mathbf{U}_2^5\, \mathbf{U}_2^6\, \mathbf{U}_2^7\, \mathbf{U}_2^8\right]^T, \\ \bar{\mathbf{U}}_3 &= \left[\mathbf{U}_3^1\, \mathbf{U}_3^2\, \mathbf{U}_3^3\, \mathbf{U}_3^4\, \mathbf{U}_3^5\, \mathbf{U}_3^6\, \mathbf{U}_3^7\, \mathbf{U}_3^8\right]^T. \end{aligned} \tag{5.44}$$

where a bold subscript represents a rotated DFT within an SLM sequence.

Example 2: consider a radix-2 64-point FFT at stage $v = 4$ with $\Omega = 8$ and $\nu = 4$. The random sequence $\Psi = [01023312]$ over $\mathcal{Z}_4$ results in matrix $\mathcal{S}$ as

$$\mathcal{S} = \begin{bmatrix} 0 & 1 & 0 & 2 & 3 & 3 & 1 & 2 \\ 4 & 5 & 4 & 6 & 7 & 7 & 5 & 6 \end{bmatrix}. \tag{5.45}$$

The phase rotated sequences using (5.45) are

$$\begin{aligned}
\bar{\mathbf{U}}_0 &= \left[\mathbf{U}_0^1\ \mathbf{U}_0^2\ \mathbf{U}_0^3\ \mathbf{U}_0^4\ \mathbf{U}_0^5\ \mathbf{U}_0^6\ \mathbf{U}_0^7\ \mathbf{U}_0^8\right]^T,\\
\bar{\mathbf{U}}_1 &= \left[\mathbf{U}_1^1\ \mathbf{U}_1^2\ \mathbf{U}_1^3\ \mathbf{U}_1^4\ \mathbf{U}_1^5\ \mathbf{U}_1^6\ \mathbf{U}_1^7\ \mathbf{U}_1^8\right]^T,\\
\bar{\mathbf{U}}_2 &= \left[\mathbf{U}_2^1\ \mathbf{U}_2^2\ \mathbf{U}_2^3\ \mathbf{U}_2^4\ \mathbf{U}_2^5\ \mathbf{U}_2^6\ \mathbf{U}_2^7\ \mathbf{U}_2^8\right]^T,\\
\bar{\mathbf{U}}_3 &= \left[\mathbf{U}_3^1\ \mathbf{U}_3^2\ \mathbf{U}_3^3\ \mathbf{U}_3^4\ \mathbf{U}_3^5\ \mathbf{U}_3^6\ \mathbf{U}_3^7\ \mathbf{U}_3^8\right]^T,\\
\bar{\mathbf{U}}_4 &= \left[\mathbf{U}_4^1\ \mathbf{U}_4^2\ \mathbf{U}_4^3\ \mathbf{U}_4^4\ \mathbf{U}_4^5\ \mathbf{U}_4^6\ \mathbf{U}_4^7\ \mathbf{U}_4^8\right]^T,\\
\bar{\mathbf{U}}_5 &= \left[\mathbf{U}_5^1\ \mathbf{U}_5^2\ \mathbf{U}_5^3\ \mathbf{U}_5^4\ \mathbf{U}_5^5\ \mathbf{U}_5^6\ \mathbf{U}_5^7\ \mathbf{U}_5^8\right]^T,\\
\bar{\mathbf{U}}_6 &= \left[\mathbf{U}_6^1\ \mathbf{U}_6^2\ \mathbf{U}_6^3\ \mathbf{U}_6^4\ \mathbf{U}_6^5\ \mathbf{U}_6^6\ \mathbf{U}_6^7\ \mathbf{U}_6^8\right]^T,\\
\bar{\mathbf{U}}_7 &= \left[\mathbf{U}_7^1\ \mathbf{U}_7^2\ \mathbf{U}_7^3\ \mathbf{U}_7^4\ \mathbf{U}_7^5\ \mathbf{U}_7^6\ \mathbf{U}_7^7\ \mathbf{U}_7^8\right]^T.
\end{aligned} \tag{5.46}$$

In the first example, consider $\bar{\mathbf{U}}_1$ and $\bar{\mathbf{U}}_2$. The corresponding time-domain SLM sequences are

$$\begin{aligned}
\bar{\mathbf{u}}_1 &= \left[\mathbf{u}_1^1\ \mathbf{u}_1^2\ \mathbf{u}_1^3\ \mathbf{u}_1^4\ \mathbf{u}_1^5\ \mathbf{u}_1^6\ \mathbf{u}_1^7\ \mathbf{u}_1^8\right]^T,\\
\bar{\mathbf{u}}_2 &= \left[\mathbf{u}_2^1\ \mathbf{u}_2^2\ \mathbf{u}_2^3\ \mathbf{u}_2^4\ \mathbf{u}_2^5\ \mathbf{u}_2^6\ \mathbf{u}_2^7\ \mathbf{u}_2^8\right]^T.
\end{aligned} \tag{5.47}$$

$\bar{\mathbf{u}}_1$ and $\bar{\mathbf{u}}_2$ can be combined to generate another time-domain SLM sequence $\hat{\mathbf{u}}$, i.e.

$$\hat{\mathbf{u}} = \left[\mathbf{u}_2^1\ \mathbf{u}_1^2\ \mathbf{u}_2^3\ \mathbf{u}_2^4\ \mathbf{u}_1^5\ \mathbf{u}_1^6\ \mathbf{u}_1^7\ \mathbf{u}_2^8\right]^T. \tag{5.48}$$

It is obvious that this sequence does not require the computation of N/r^{v-1}-point DFTs. thus further reducing complexity. In this way, we can also generate several combined time-domain subsets in Example 2. Next, we present a general approach to obtaining the combination of subsets.

2) Combination of time-domain subsets: Define the set $\hat{\Omega} = 1, 2, \ldots, \Omega$. The proposed SLM technique combining time-domain subsets is accomplished as follows

1. Phase rotate all inputs to the ν subsets of $\frac{N}{r^{v-1}}$-point DFTs. Initialize $i = 0$ and $\hat{\Omega} = 0$. Compute the time domain SLM sequence $\bar{\mathbf{u}}_0$.
2. Construct matrix $\mathcal{S}$ using (5.42).

3. Set $\hat{\Omega} = 1$ and obtain $\bar{\mathbf{u}}_1$. If $\hat{\Omega} < \Omega - 1$, go to the next step. Otherwise, quit.
4. phase rotate one of subsets using matrix $\mathcal{S}$.
5. Set $\hat{\Omega} = \hat{\Omega} + 1$ and obtain $\bar{\mathbf{u}}_{\hat{\Omega}}$.
6. If $\hat{\Omega} = \Omega - 1$, quit. Otherwise, generate all $\hat{\Omega}_c$ combinations of $\bar{\mathbf{u}}_1, \bar{\mathbf{u}}_2, \ldots, \bar{\mathbf{u}}_{\hat{\Omega}}$.
7. Set $\hat{\Omega} = \hat{\Omega} + \hat{\Omega}_c$. If $\hat{\Omega} = \Omega - 1$, quit. Otherwise go to step 4.

Consider the second example including the combination of subsets. The sequences are

$$\begin{aligned}
\bar{\mathbf{u}}_0 &= \left[\mathbf{u}_0^1\ \mathbf{u}_0^2\ \mathbf{u}_0^3\ \mathbf{u}_0^4\ \mathbf{u}_0^5\ \mathbf{u}_0^6\ \mathbf{u}_0^7\ \mathbf{u}_0^8\right]^T, \\
\bar{\mathbf{u}}_1 &= \left[\mathbf{u}_1^1\ \mathbf{u}_1^2\ \mathbf{u}_1^3\ \mathbf{u}_1^4\ \mathbf{u}_1^5\ \mathbf{u}_1^6\ \mathbf{u}_1^7\ \mathbf{u}_1^8\right]^T, \\
\bar{\mathbf{u}}_2 &= \left[\mathbf{u}_2^1\ \mathbf{u}_2^2\ \mathbf{u}_2^3\ \mathbf{u}_2^4\ \mathbf{u}_2^5\ \mathbf{u}_2^6\ \mathbf{u}_2^7\ \mathbf{u}_2^8\right]^T, \\
\hat{\mathbf{u}}_3 &= \left[\mathbf{u}_3^1\ \mathbf{u}_1^2\ \mathbf{u}_3^3\ \mathbf{u}_2^4\ \mathbf{u}_3^5\ \mathbf{u}_3^6\ \mathbf{u}_1^7\ \mathbf{u}_2^8\right]^T, \\
\bar{\mathbf{u}}_4 &= \left[\mathbf{u}_4^1\ \mathbf{u}_4^2\ \mathbf{u}_4^3\ \mathbf{u}_4^4\ \mathbf{u}_4^5\ \mathbf{u}_4^6\ \mathbf{u}_4^7\ \mathbf{u}_4^8\right]^T, \\
\hat{\mathbf{u}}_5 &= \left[\mathbf{u}_5^1\ \mathbf{u}_1^2\ \mathbf{u}_5^3\ \mathbf{u}_5^4\ \mathbf{u}_4^5\ \mathbf{u}_4^6\ \mathbf{u}_1^7\ \mathbf{u}_5^8\right]^T, \\
\hat{\mathbf{u}}_6 &= \left[\mathbf{u}_6^1\ \mathbf{u}_6^2\ \mathbf{u}_6^3\ \mathbf{u}_2^4\ \mathbf{u}_4^5\ \mathbf{u}_4^6\ \mathbf{u}_6^7\ \mathbf{u}_2^8\right]^T, \\
\hat{\mathbf{u}}_7 &= \left[\mathbf{u}_7^1\ \mathbf{u}_1^2\ \mathbf{u}_7^3\ \mathbf{u}_2^4\ \mathbf{u}_4^5\ \mathbf{u}_4^6\ \mathbf{u}_1^7\ \mathbf{u}_2^8\right]^T.
\end{aligned} \tag{5.49}$$

As shown in [41], with the ϕ_Ω^η randomly chosen from $\{0, \pi\}$ or $\{0, \pi/2, \pi, 3\pi/2\}$, the resulting phase sequences provide better PAPR reduction compared to other sequences. Thus, in this work the phase sequences ϕ_Ω^η are randomly chosen from $\{0, \pi\}$.

Similar to the PTS-ECC technique, we should mention that the partial DFTs are designed once (offline), and do not need to be modified for transmission. Therefore, they do not add any complexity to the system. Since these locations are predetermined at the receiver, P-SLM requires the same side information as O-SLM [37].

The effect of $m - v$ and ν on the PAPR reduction are examined in the next section.

3) PAPR and complexity reduction: Similar to (5.21), in order to compare the additive complexity between two PAPR reduction techniques we define the additive complexity reduction ratio as

$$R^{add} = 1 - \frac{B^{add,1}}{B^{add,2}}. \tag{5.50}$$

Table 5.6. *Multiplicative and additive complexity reduction for P-SLM over DIF-SLM ($\nu = 2^0$) and O-SLM [27] with $N = 2048$, $\Omega = 8$, and $\nu = 2^1$*

$m - v$	P-SLM compared to DIF-SLM ($\nu = 2^0$)		P-SLM compared to O-SLM [27]	
	$R^{mul}(\%)$	$R^{add}(\%)$	$R^{mul}(\%)$	$R^{add}(\%)$
5	41	39	75	68
4	36	36	79	72
3	29	33	83	76
2	18	30	87	81

The multiplicative and additive complexity of the proposed SLM technique is compared with the DIF-SLM ($\nu = 2^0$) and O-SLM [37] in Tables 5.6 for $r = 2, 2 \leq m-v \leq 5, \nu = 2$, $N = 2048$ and $\Omega = 8$. Partial SLM in comparison with DIF-SLM achieves a multiplicative and additive complexity reduction of 18% to 41% and 30% to 39%, respectively. The corresponding reduction over O-SLM [37] is 75% to 87% and 68% to 81%.

Figure 5.17 show the CCDF of O-SLM, the proposed scheme, and DIF-SLM for $m - v = 2, 5$. We consider $\nu = 2$ and 4. For $\nu = 2$, P-SLM with $m - v = 5$ performs close to O-SLM. It also has a PAPR reduction similar to that of DIF-SLM. The proposed SLM in comparison with DIF-SLM achieves a multiplicative and additive complexity reduction of $R^{mul} = 41\%$ and $R^{add} = 39\%$, respectively, with $m - v = 5$. The corresponding reductions over O-SLM are 75% to 68%. If we increase ν to 4, the PAPR performance is degraded. We found through simulation with various values of N that if we choose $\nu = 2$, the proposed SLM technique performs similar to O-SLM. As seen in Table 5.6, for $\nu = 2$, the difference in multiplicative and additive complexity reductions is about 12% when we choose $m - v = 2$ rather than $m - v = 5$. However, the results show that a PAPR improvement of almost 1.5 dB can be achieved using $m - v = 5$ over $m - v = 2$. Therefore, the new technique (P-SLM) provides a better PAPR versus complexity tradeoff compared to DIF-SLM and DIT-SLM.

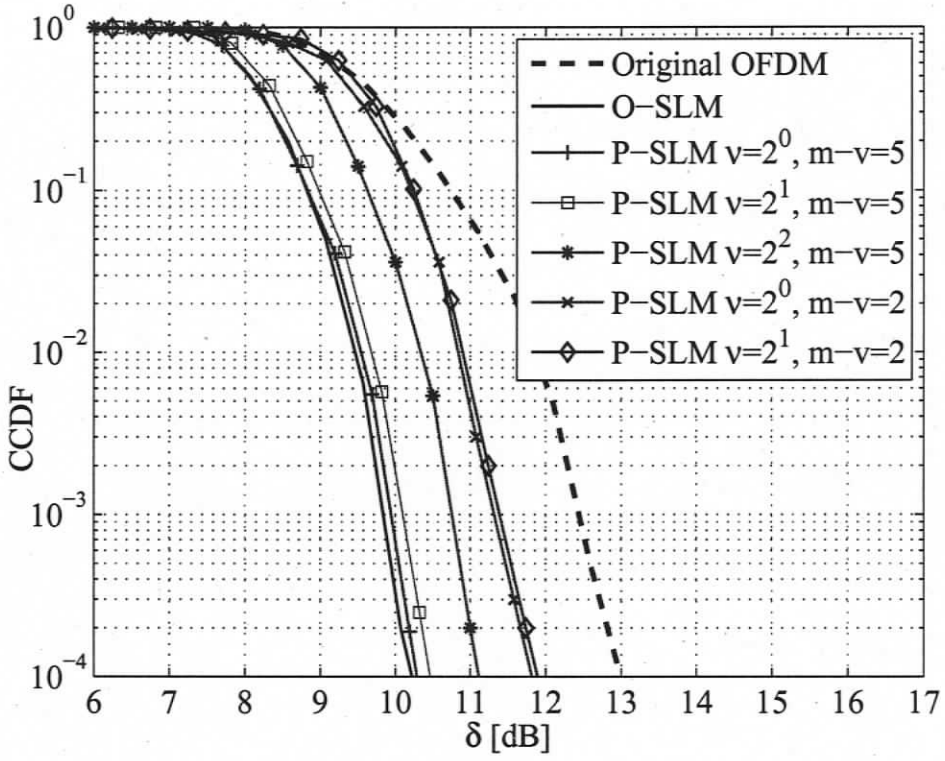

Figure 5.17. *CCDF of P-SLM compared with DIF-SLM ($\nu = 2^0$) and O-SLM for various numbers of remaining stages $m - v$, partial number of DFTs, ν, and 8 SLM sequences ($\Omega = 8$) with $r = 2$ and $N = 2048$.*

5.3 TR and the Common FFT Algorithms

As previously discussed, in the suboptimal iterative algorithms, the PAPR reduction capability strongly depends on the locations and number of peak reduction tones (PRTs). These locations also affect the convergence rate of the solution. As indicated in [42]-[44], the optimal peak reduction kernels can be computed off-line or during the initialization process if the channel is static. However when the channel is not static, the PRT locations and consequently the peak reduction kernels should be updated as the channel varies [42]-[47]. This creates significant computational complexity. For example, to obtain a good PRT set (with a PAPR loss less than 0.1 dB from the optimal case), a complexity of one fast Fourier transforms (FFTs) per set is reported in [42], with 11 to 28 randomly sets of reserved subcarriers required. Side information must also be transmitted in order to identify the reserved tones at the receiver.

In this section, we introduce IFFT-based tone reservation (TR) and propose an efficient gradient-based algorithm for the TR PAPR reduction technique. This algorithm utilizes the common FFT algorithms to reduce the computational complexity associated with optimizing the peak reduction kernels. We show that this new algorithm can significantly reduce the computational complexity in generating these kernels. Thus they can be updated efficiently when the channel is not static. Since passband transmission is typically considered when the channel is not static, we consider complex multicarrier signals. The proposed technique has significantly less computational complexity compared to that with the schemes in [42]-[47]. Results are presented which demonstrate that the proposed algorithm has PAPR performance close to that of the gradient algorithm in [42]-[47], at a cost of one to two additional bits of side information.

5.3.1 IFFT-based TR

Referring to Section 4.2.3.1 and using (4.34), the IFFT output corresponding to the inputs of the identical IDFTs at a particular stage v can be expressed as

$$x(n) = \sum_{\eta=1}^{r^{v-1}} \widetilde{x}^{\eta}(\widetilde{n}) = \sum_{\eta=1}^{r^{v-1}} \frac{1}{N/r^{v-1}} \sum_{\widetilde{k}=0}^{\frac{N}{r^{v-1}}-1} \widetilde{X}^{\eta}(\widetilde{k}) T_{N/r^{v-1}}^{-\widetilde{n}\widetilde{k}} \tag{5.51}$$

and from (4.38), we can write (5.51) in matrix notation as

$$\begin{bmatrix} x(0) \\ x(1) \\ \vdots \\ x(n) \end{bmatrix}_N = \begin{bmatrix} \widetilde{x}^1(\widetilde{n}) \\ \vdots \\ \widetilde{x}^{\eta}(\widetilde{n}) \\ \vdots \\ \widetilde{x}^{r^{v-1}}(\widetilde{n}) \end{bmatrix}_N = \begin{bmatrix} Q^1 \\ \vdots \\ Q^{\eta} \\ \vdots \\ Q^{r^{v-1}} \end{bmatrix}_{N\times N} \begin{bmatrix} \widetilde{X}^1(\widetilde{k}) \\ \vdots \\ \widetilde{X}^{\eta}(\widetilde{k}) \\ \vdots \\ \widetilde{X}^{r^{v-1}}(\widetilde{k}) \end{bmatrix}_N \tag{5.52}$$

, respectively, where the (identical) IDFT submatrices are

$$Q^1 = \ldots = Q^{\eta} \ldots = Q^{r^{v-1}} = \begin{bmatrix} 1 & \cdots & 1 & \cdots & 1 \\ \vdots & \ddots & \vdots & \ddots & \vdots \\ 1 & \cdots & T_{N/r^{v-1}}^{-\widetilde{n}\widetilde{k}} & \cdots & T_{N/r^{v-1}}^{-\widetilde{n}(N/r^{v-1}-1)} \\ \vdots & \ddots & \vdots & \ddots & \vdots \\ 1 & \cdots & T_{N/r^{v-1}}^{-\widetilde{k}(N/r^{v-1}-1)} & \cdots & T_{N/r^{v-1}}^{-(N/r^{v-1}-1)^2} \end{bmatrix}_{N/r^{v-1}\times N/r^{v-1}} . \tag{5.53}$$

Consider passband transmission and intermediate stage v with $\frac{L}{r^{v-1}} \geq 1$ where L is a power of 2. We divide the peak reduction tones (PRTs) into equal subsets of size L/r^{v-1}, thus from Section 3.2.5.1

$$\Lambda = \left[\lambda^1(1), \ldots, \lambda^1(\frac{L}{r^{v-1}}), \ldots, \lambda^{\eta}(1), \ldots, \lambda^{\eta}(\frac{L}{r^{v-1}}), \ldots, \lambda^{r^{v-1}}(1), \ldots, \lambda^{r^{v-1}}(\frac{L}{r^{v-1}})\right]. \tag{5.54}$$

To simplify the derivation, unequal sized subsets are excluded, but can easily be employed in practice. Then, every subset $\lambda^{\eta}(1), \ldots, \lambda^{\eta}(\frac{L}{r^{v-1}})$ is randomly chosen over each vector

$\widetilde{X}^{\eta}(\widetilde{k})$. Thus, we have the matrices

$$\widehat{\mathbf{C}} = \Bigg[\underbrace{C^1(\lambda_1),\ldots,C^1(\lambda_{\frac{L}{r^{v-1}}})}_{\mathbf{C}^1},\ldots,\underbrace{C^{\eta}(\lambda_1),\ldots,C^{\eta}(\lambda_{\frac{L}{r^{v-1}}})}_{\mathbf{C}^{\eta}},$$
$$\ldots,\underbrace{C^{r^{v-1}}(\lambda_1),\ldots,C^{r^{v-1}}(\lambda_{\frac{L}{r^{v-1}}})}_{\mathbf{C}^{r^{v-1}}}\Bigg]^T, \tag{5.55}$$

and

$$\widehat{Q} = \Bigg[\underbrace{q^1(\lambda_1),\ldots,q^1_{\lambda_{\frac{L}{r^{v-1}}}}}_{\in Q^1},\ldots,\underbrace{q^{\eta}(\lambda_1),\ldots,q^{\eta}(\lambda_{\frac{L}{r^{v-1}}})}_{\in Q^{\eta}},\ldots,\underbrace{q^{r^{v-1}}(\lambda_1),\ldots,q^{r^{v-1}}(\lambda_{\frac{L}{r^{v-1}}})}_{\in Q^{r^{v-1}}}\Bigg]. \tag{5.56}$$

$\widehat{Q}$ represents the submatrices $Q^1, Q^2, \ldots, Q^{\eta}, \ldots, Q^{r^{v-1}}$ with only the columns which correspond to the reserved tones Λ and $\widehat{q}^{row,\,\eta}(\widetilde{k})$ denote the $\widetilde{k}$th row of Q^{η}.

In order to see how the reserved tones for IFFT-based TR work and are equivalent to reserved tones at the input of the IFFT, as an example consider a 32-point radix-2 IFFT with normally ordered inputs $X(k)$ and digit-reversed outputs $x(n)$. This is illustrated in Figure 5.18. The input and output orders also listed in Table 5.7. Consider the inputs

$$\begin{gathered}\left[\widetilde{X}^1(0),\widetilde{X}^1(1),\ldots,\widetilde{X}^1(7)\right]^T \\ \left[\widetilde{X}^2(0),\widetilde{X}^2(1),\ldots,\widetilde{X}^2(7)\right]^T \\ \left[\widetilde{X}^3(0),\widetilde{X}^3(1),\ldots,\widetilde{X}^3(7)\right]^T \\ \left[\widetilde{X}^4(0),\widetilde{X}^4(1),\ldots,\widetilde{X}^4(7)\right]^T\end{gathered} \tag{5.57}$$

at stage $v = 3$ with $L = 8$. Assume the randomly chosen PRT locations are $\Lambda = [01467352]$ where the size of the subsets is 2. We then have

$$\widehat{\mathbf{C}} = \left[C^1(0), C^1(1), C^2(4), C^2(6), C^3(7), C^3(3), C^4(5), C^4(2)\right]^T. \tag{5.58}$$

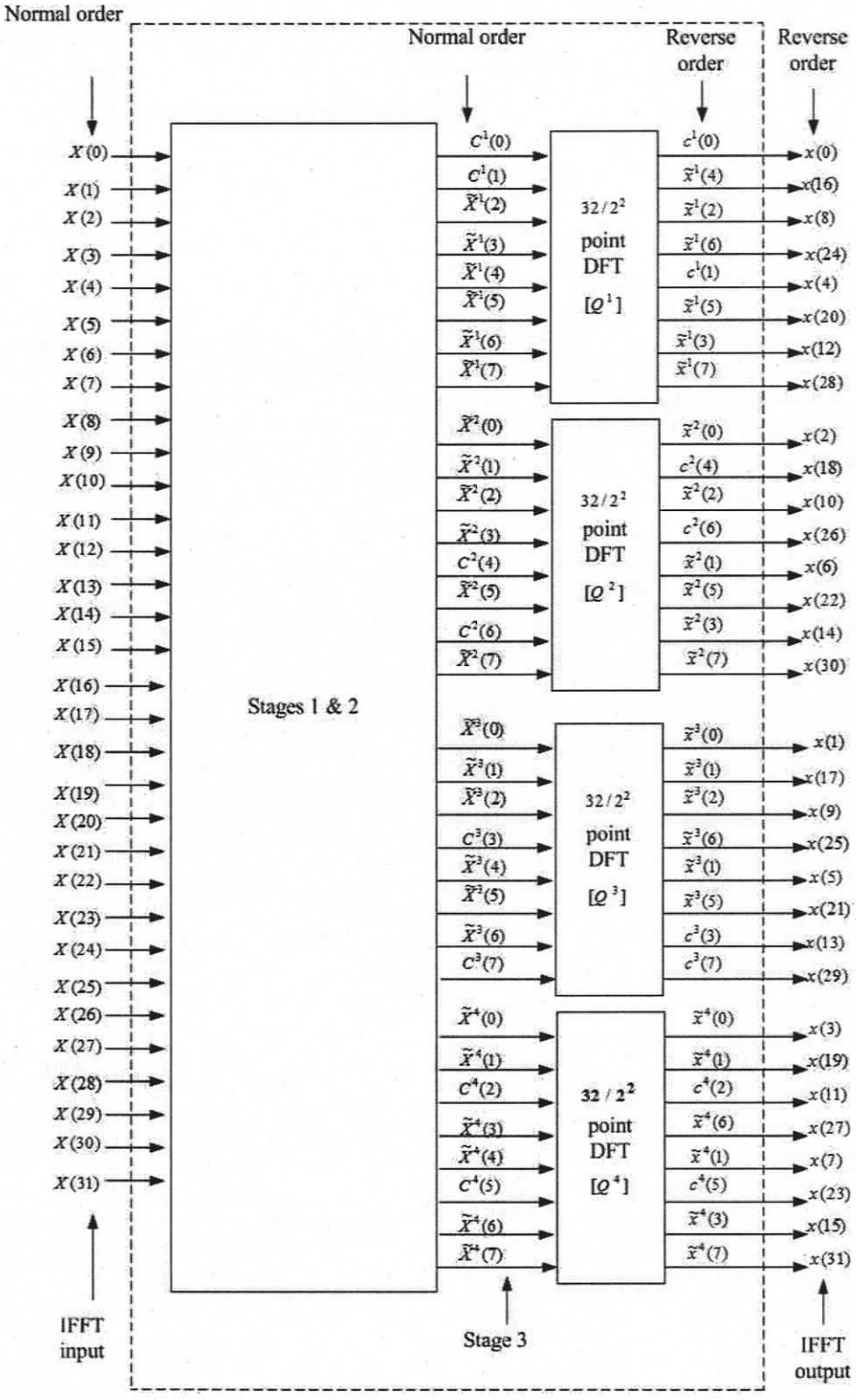

Figure 5.18. *32-point DFT with reserved tone vector C corresponding to intermediate signals $\widehat{C}$ at stage $v = 3$.*

Table 5.7. *Normal and digit-reversed inputs and outputs for a 32-point IFFT with 8-point identical IDFTs at stage* $v = 3$.

$\eta = 1$				$\eta = 2$			
k	$\widetilde{k}$	$\widetilde{n}$	n	k	$\widetilde{k}$	$\widetilde{n}$	n
0	0	0	0	8	0	0	2
1	1	4	16	9	1	4	18
2	2	2	8	10	2	2	10
3	3	6	24	11	3	6	26
4	4	1	4	12	4	1	6
5	5	5	20	13	5	5	22
6	6	3	12	14	6	3	14
7	7	7	28	15	7	7	30
$\eta = 3$				$\eta = 4$			
k	$\widetilde{k}$	$\widetilde{n}$	n	k	$\widetilde{k}$	$\widetilde{n}$	n
16	0	0	1	24	0	0	3
17	1	4	17	25	1	4	19
18	2	2	9	26	2	2	11
19	3	6	25	27	3	6	27
20	4	1	5	28	4	1	7
21	5	5	21	29	5	5	23
22	6	3	13	30	6	3	15
23	7	7	29	31	7	7	31

As seen in Figure 5.18 and Table 5.7, the time domain signal **c** is related to the time-domain signal **x** as

$$c^1(0) = x(0),\ c^1(1) = x(4),\ c^2(4) = x(18),\ c^2(6) = x(26),$$
$$c^3(7) = x(29),\ c^3(3) = x_{13},\ c^4(5) = x(23),\ c^4(2) = x(11). \tag{5.59}$$

Hence, the reserved subcarriers at the input of the IFFT are

$$\mathbf{C} = [C(0), C(4), C(11), C(13), C(18), C(23), C(26), C(29)]^T. \tag{5.60}$$

Note that similar to conventional TR, these reserved tones are discarded at the receiver. We next consider the gradient algorithm as it is a suboptimal iterative algorithm with low complexity.

5.3.1.1 The efficient suboptimal approach

We propose an efficient, low complexity approach to computing the peak reduction kernels (PRTs) which is an appropriate choice when PRTs require to be updated dynamically. In this approach, we use the intermediate reserved tones to generate the peak reduction kernels $\mathbf{e}_n^{\|2}$, i.e. $\mathbf{e}_n^{\|2} = \widehat{Q}(\breve{q}^{row}(n))^*$ becomes $\mathbf{e}_n^{\|2} = \widehat{Q}^{\eta}(\breve{q}^{row}(\widetilde{n}))^*$ (see (3.25)). We present two algorithms with different complexities based on the reserved intermediate tones.

1) Different random PRT locations over identical IDFTs (DPRT): We choose a different subset of PRT locations (DPRT) for each of the identical N/r^{v-1}-point IDFTs, i.e.

$$\mathbf{C}^1 \neq \mathbf{C}^2 \neq \ldots \neq \mathbf{C}^{\eta} \neq \ldots \neq \mathbf{C}^{r^{v-1}}. \tag{5.61}$$

Hence, the iterative gradient algorithm in (3.25) is given by

$$\breve{\mathbf{x}}^{(\beta+1)} = \breve{\mathbf{x}}^{(\beta)} - \mu \sum_{|\breve{x}(n)^{(\beta)}|>A} \left(\breve{x}(n)^{(\beta)} - Ae^{\angle(\breve{x}(n)^{(\beta)})}\right) \left[\mathbf{e}_{\widetilde{n},1}^{\|2}, \ldots, \mathbf{e}_{\widetilde{n},\eta}^{\|2}, \ldots, \mathbf{e}_{\widetilde{n},r^{v-1}}^{\|2}\right] \tag{5.62}$$

and similar to (3.25), the circular shift property of the identical IDFTs gives the kernels $\mathbf{e}_{\widetilde{n},\eta}^{\|2}$ for $\widetilde{n} = 0, \ldots, \frac{N}{r^{v-1}} - 1$ as

$$e_{\widetilde{n}_\beta,\eta}^{\|2}[\widetilde{n}] = e_{\widetilde{n}_0,\eta}^{\|2}[(\widetilde{n} - \widetilde{n}_\beta)_{\frac{N}{r^{v-1}}}]. \tag{5.63}$$

If we compare (5.62) with (3.25), the computational complexity of Step 4 in the gradient algorithm described in Section 3.2.5.3 is reduced from $O(N \log_r N)$ to $O(N \log_r N/r^{v-1})$.

2) The same random PRT locations over identical IDFTs (SPRT): In this case, the same PRT locations (SPRT) are reserved in the vectors $\widetilde{X}^{\eta}(\widetilde{k})$. In fact, we choose the same subset of PRT locations over all N/r^{v-1}-point IDFTs. Then, the submatrices $\mathbf{C}^{\eta}$ in (5.55) and the kernels $\mathbf{e}_{\widetilde{n},\eta}^{\|2}$ in (5.62) are

$$\mathbf{C}^1 = \mathbf{C}^2 = \ldots = \mathbf{C}^{\eta} = \ldots = \mathbf{C}^{r^{v-1}}, \tag{5.64}$$

and

$$\mathbf{e}_{\widetilde{n},1}^{\|2} = \mathbf{e}_{\widetilde{n},2}^{\|2} = \ldots = \mathbf{e}_{\widetilde{n},\eta}^{\|2} = \ldots = \mathbf{e}_{\widetilde{n},r^{v-1}}^{\|2}, \tag{5.65}$$

respectively. Note that in contrast to DPRT, this algorithm requires equal sized subsets. In this case, (5.62) becomes

$$\breve{\mathbf{x}}^{(\beta+1)} = \breve{\mathbf{x}}^{(\beta)} - \mu \sum_{|\breve{x}(n)^{(\beta)}|>A} \left(\breve{x}(n)^{(\beta)} - Ae^{\angle(\breve{x}(n)^{(\beta)})}\right) \left[\mathbf{e}_{\widetilde{n}}^{\|2}, \ldots, \mathbf{e}_{\widetilde{n}}^{\|2}, \ldots, \mathbf{e}_{\widetilde{n}}^{\|2}\right]. \tag{5.66}$$

With SPRT, we exploit the similarity of the identical IDFTs to determine the best PRT locations and compute the peak-reduction kernels. Therefore, the complexity of Step 4 in Section II is significantly reduced from $O(N \log_r N)$ to $O(N/r^{v-1} \log_r N/r^{v-1})$. The second algorithm, SPRT, clearly has lower computational complexity compared to DPRT. However, intuitively the first algorithm (DPRT) can generate a satisfactory $\mathbf{e}$ with a smaller value of $\bar{I}$ than the algorithm in (5.66). This is confirmed by the numerical results given later. We will also see that both algorithms can achieve very close PAPR reduction to the conventional gradient algorithm for particular values of r and v.

3) Analysis of the computational complexity: As stated earlier, the computational complexity of computing the peak reduction kernels is essentially determined by the IFFT operation in Step 4 of the algorithm in Section 3.2.5.1. From (4.42), rewrite the multiplicative complexity of a DIF IFFT algorithm as

$$B_v^{mul,DIF} = r^{v-1}\left(\frac{N}{r^v} - 1\right). \tag{5.67}$$

Since the DPRT algorithm uses r^{v-1} identical N/r^{v-1}-point IDFTs between stages v and m, the multiplicative complexity of computing the peak reduction kernels with $\bar{I}_{DPRT}$ iterations is

$$B_{DPRT}^{mul} = \bar{I}_{DPRT} \sum_{i=v}^{m} B_v^{mul,DIF}. \tag{5.68}$$

Since SPRT uses only one N/r^{v-1}-point IDFT to generate the kernels, the multiplicative complexity with $\bar{I}_{SPRT}$ iterations is

$$B_{SPRT}^{mul} = \bar{I}_{SPRT} \sum_{i=v}^{m} (\frac{N}{r^v} - 1). \tag{5.69}$$

From (4.46), the additive complexity of DPRT with $\bar{I}_{DPRT}$ iterations and SPRT with $\bar{I}_{SPRT}$ iterations is

$$B_{DPRT}^{add} = \bar{I}_{DPRT} N(r-1)(m-v), \tag{5.70}$$

and

$$B_{SPRT}^{add} = \bar{I}_{SPRT} \frac{N}{r^{v-1}}(r-1)(m-v), \tag{5.71}$$

respectively. Finally, with $\bar{I}_T$ iterations the additive and multiplicative complexity of the MSE algorithm in [42] is

$$B_T^{mul} = \bar{I}_T \sum_{i=1}^{m} B_i^{mul,DIF} \tag{5.72}$$

and

$$B_T^{add} = \bar{I}_T N m(r-1), \tag{5.73}$$

respectively.

To compare the multiplicative and additive complexity of our proposed algorithms to that of the MSE algorithms in [42], the reduction ratios are defined similar to (5.21) and (5.50).

4) The number of iterations $\bar{I}$: Referring to Section 3.2.5.3, a random search over all possible sets will greatly increase the complexity of tone reservation. As an alternative solution, $\bar{I}$ randomly generated sets $\Lambda^1, \Lambda^2, \ldots, \Lambda^{\bar{I}}$ can be considered and the best one is selected to generate the peak reduction signal $\mathbf{c}$. As shown in [42], since $\bar{I}$ PRT locations

are chosen randomly, $\bar{I}$ should be sufficiently high in order to provide a good PRT set. This is evaluated using the cumulative distribution function (CDF) of the absolute value of the second peak $|\Gamma|$ which should be less than a threshold γ, $CDF(\gamma) = Prob(|\Gamma| < \gamma)$. To have $|\Gamma| < \gamma$ with 99.9999% confidence, $\bar{I}$ should satisfy [42]

$$\bar{I} \geq \frac{\log(10^{-6})}{\log(1 - CDF(\gamma))}. \tag{5.74}$$

This criteria is used to obtain the number of iteration $\bar{I}$ for different TR techniques.

Lastly, the following remarks should be made for the proposed gradient-based TR.

- As stated in [42], if the channel is quasi-static (which is considered in this thesis), the PRTs Λ and the kernel $\mathbf{e}$ should be updated periodically. In order to recover the data at the receiver, side information must be transmitted [42]. Since a predetermined number of subcarrier subsets $\bar{I}$ is used to generate the best PRT set, this approach requires $\log_2 \bar{I}$ bits of side information.
- The proposed IFFT-based TR algorithms provide more trade-offs between complexity and PAPR-performance compared to the gradient algorithm [42] as they are a function of r and v.

5) Numerical Results: In this section, we first compute the best value of $\bar{I}$ and the peak reduction kernels for the our proposed algorithms, and compare them with algorithm in [42] in terms of complexity. Then, we employ the designed kernels in the gradient algorithms in (3.25), (5.62), and (5.66) and compare our algorithms with prior work [42] in terms of PAPR performance. QPSK subcarrier modulation is employed. The multicarrier signal is oversampled by a factor of 4 [55] using zero padding in the frequency domain at the IFFT input [2]. The number of reserved subcarriers is $L = 32$. We consider $N = 512$ and $r = 2$ for complex OFDM signals. Similar results can be obtained for other values of N and r.

- Number of iterations $\bar{I}$: Figure 5.19 shows the CDF of the absolute value of the second peak using the DPRT algorithm for $L = 32$ and $8 \leq r^{v-1} \leq 32$ and with Tellado's algorithm [42] for $L = 32$. This shows that $|\Gamma| < \gamma$ for the DPRT algorithm

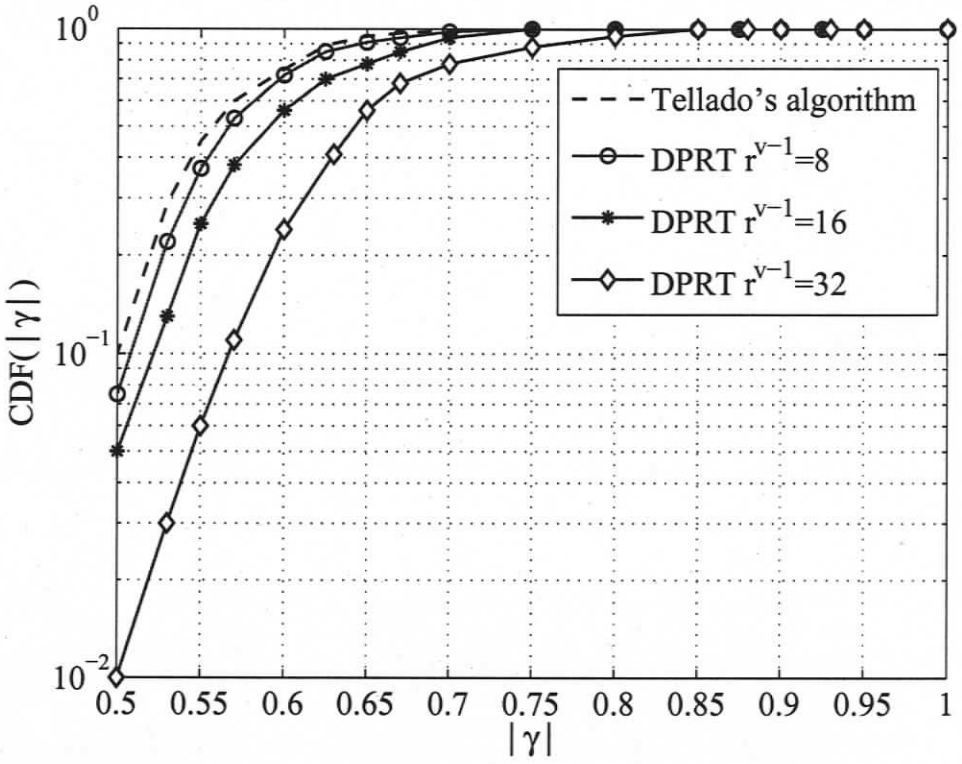

Figure 5.19. *Cumulative distribution function of the absolute value of the second peak versus the number of iterations $\bar{I}$ using the DPRT algorithm for $L = 32$ and $8 \leq r^{v-1} \leq 32$ in comparison with Tellado's algorithm [42].*

is higher than that for algorithm in [42]. This increases as r^{v-1}, i.e. the number of identical IDFTs, is increased. This leads to a greater number of iterations $\bar{I}_{DPRT}$ as indicated in Table 5.8, which compares the number of iterations $\bar{I}$. Table 5.9 compares complexity reduction ratios R^{mul} and R^{add} between DPRT and algorithms in [42] with $0.5 < |\gamma| < 0.75$ and $r^{v-1} = 8, 16$. Although DPRT requires more iterations, it has multiplicative and additive reduction ratios of $25\% \leq R^{mul} \leq 56\%$ and $7\% \leq R^{add} \leq 69\%$, respectively. This is as expected since the DPRT algorithm requires less complexity per iteration than algorithm in [42]. However, as seen in

Table 5.8. *The number of iterations $\bar{I}_{DPRT}$ for the DPRT algorithm and $\bar{I}_T$ for algorithm in [42] as a function of the cumulative distribution function of the absolute value of the second peak CDF(γ).*

	CDF(γ)				$\bar{I}_{DPRT}$	
γ	Algorithm in [42]	$r^{v-1}=8$	$r^{v-1}=16$	$\bar{I}_T$	$r^{v-1}=8$	$r^{v-1}=16$
0.75	1	1	1	1	1	1
0.70	0.99	0.98	0.94	3	3	5
0.65	0.95	0.91	0.78	5	6	9
0.60	0.75	0.72	0.56	10	11	17
0.55	0.45	0.37	0.25	23	30	48
0.50	0.09	0.07	0.05	131	177	269

Table 5.9. *Computational complexity comparison between DPRT and algorithm in [42] for computing peak reduction kernels.*

	$\bar{I}_{DPRT}$		$R^{mul}(\%)$		$R^{add}(\%)$	
$\bar{I}_T$	$r^{v-1}=8$	$r^{v-1}=16$	$r^{v-1}=8$	$r^{v-1}=16$	$r^{v-1}=8$	$r^{v-1}=16$
1	1	1	56	69	44	55
3	3	5	56	49	44	25
5	6	9	48	45	33	20
10	11	17	52	48	38	24
23	30	48	43	37	27	8
131	177	269	41	37	25	7

Figure 5.19 , $CDF|\gamma|$ is decreased significantly for $r^{v-1} \leq 32$. This requires a large number of iterations, in which case the computational complexity savings becomes negligible ($r^{v-1} = 32$). The value $r^{v-1} = 8$ provides the best complexity reduction for the DPRT algorithm compared to other values.

The CDF of the absolute value of the second peak for various value of γ using the SPRT algorithm is plotted in Figure 5.20 for $L = 32$ and $8 \leq r^{v-1} \leq 32$. Similar to DPRT, CDF(γ) is lower than with algorithm in [42], and this difference increases as the number of identical IDFTs r^{v-1} is increased. However, CDF(γ) for SPRT decays faster than CDF(γ) for DPRT. In Table 5.10, we present the number of iterations $\bar{I}$. Complexity reduction ratios R^{mul} and R^{add} are given in Table 5.11 for SPRT over algorithm in [42] with $0.5 < |\gamma| < 0.75$ and $r^{v-1} = 8, 16$. This shows that the SPRT algorithm significantly reduces the computational complexity as the multiplicative and additive reduction ratios are $33\% \leq R^{mul} \leq 89\%$ and $2.5\% \leq R^{add} \leq 86\%$, respectively. As CDF($\gamma$) for SPRT decays quickly, a large number of iterations is required. We will see in the next that a small number of iterations results in a very slight degradation in PAPR performance compared to the previous technique. Figure 5.20 also shows that CDF(γ) is significantly reduced for $r^{v-1} = 32$, but $r^{v-1} = 8$ shows the best complexity reduction for the SPRT as well.

- PAPR performance: The kernels computed for the values of $|\gamma|$ given above are used to reduce the peak power of the OFDM signal. The value $r^{v-1} = 8$ is employed to obtain the peak reduction vector $\widehat{\mathbf{C}}$. The number of iterations β for the gradient algorithms in (3.25), (5.62), and (5.66) is set to 40. We consider a clipping level of $A = 6dB$ for $L = 32$ reserved tones.

  For the proposed technique, The clipping probability versus various clipping threshold levels corresponding to $\widehat{\mathbf{C}}$ is plotted as solid lines in Figures 5.21 and 5.22 for DPRT and SPRT with ($L/N = 6.3\%$) and $|\gamma| = 0.6, 0.65, 0.7, 1$ for original OFDM are plotted in the same figures as dashed curves. These figures show that the DPRT and SPRT algorithms have a slightly degradation in PAPR performance compared to

Table 5.10. *The number of iterations $\bar{I}_{SPRT}$ for the DPRT algorithm and $\bar{I}_T$ for algorithm in [42] as a function of the cumulative distribution function of the absolute value of the second peak CDF(γ).*

	CDF(γ)				$\bar{I}_{SPRT}$	
γ	Tellado [42]	$r^{v-1}=8$	$r^{v-1}=16$	$\bar{I}_T$	$r^{v-1}=8$	$r^{v-1}=16$
0.75	1	0.95	0.8	1	5	8
0.70	0.99	0.90	0.68	3	6	12
0.65	0.95	0.73	0.42	5	10	25
0.60	0.75	0.45	0.10	10	24	131
0.55	0.45	0.16	0.02	23	79	682

Table 5.11. *Computational complexity comparison between DPRT and algorithm in [42] for computing peak reduction kernels.*

	$\bar{I}_{SPRT}$		$R^{mul}(\%)$		$R^{add}(\%)$	
$\bar{I}_T$	$r^{v-1}=8$	$r^{v-1}=16$	$r^{v-1}=8$	$r^{v-1}=16$	$r^{v-1}=8$	$r^{v-1}=16$
1	5	8	72	84	65	77
3	6	12	89	92	86	85
5	10	25	88	90	85	84
10	24	131	86	75	83	63
23	79	682	81	43	76	17

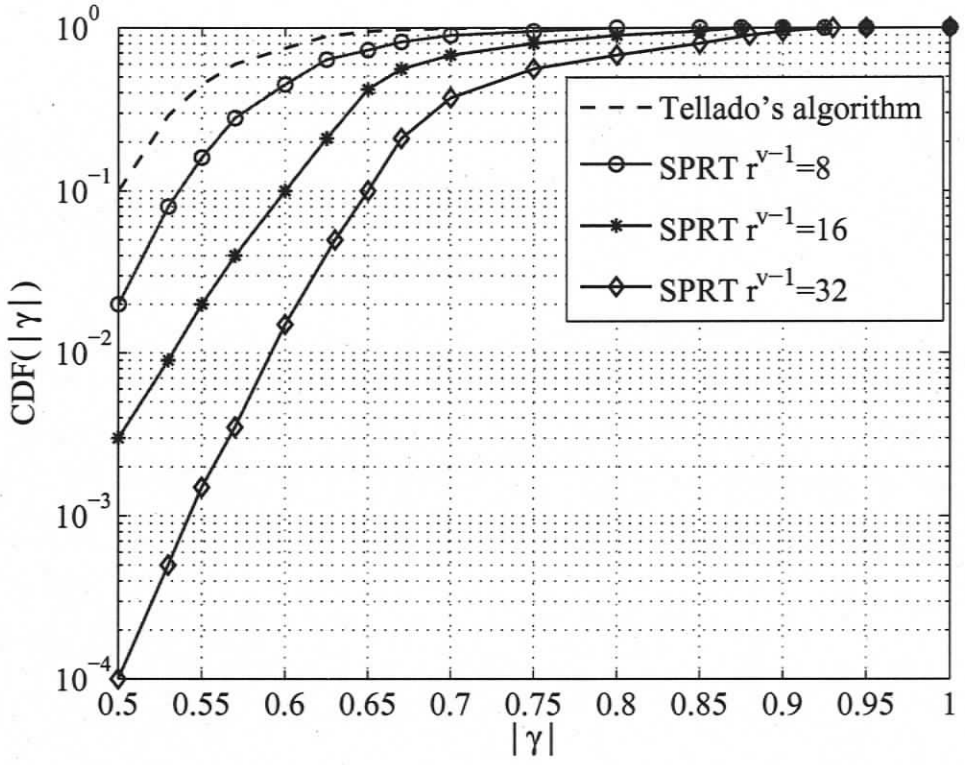

Figure 5.20. *Cumulative distribution function of the absolute value of the second peak versus the number of iterations $\bar{I}$ using the SPRT algorithm for $L = 32$ and $8 \leq r^{v-1} \leq 32$ in comparison with Tellado's algorithm [42].*

the algorithm in [42] when $r^{v-1} = 8$. For example, a PAPR loss between 0.2 and 0.4 dB is observed for a clipping probability of 10^{-4} and $|\gamma| = 0.6$. From Table 5.9, to achieve this performance, computing the kernel requires far less computational complexity ($R^{mul} = 52\%$ and $R^{add} = 38\%$), than that required by the algorithm in [42]. As seen in Table 5.11, this reduction significantly increases ($R^{mul} = 86\%$ and $R^{add} = 83\%$), when SPRT is employed. Hence, the proposed DPRT and SPRT algorithms offer excellent tradeoffs between computational complexity and PAPR performance. With $r^{v-1} = 8$ and $|\gamma| = 0.6$, SPRT is superior to DPRT as it provides a substantial reduction in complexity compared to the gradient algorithm in [42], at the cost of only a 0.4 dB degradation in PAPR performance.

In terms of side information, comparing the number of iterations in Tables 5.8 and 5.10, $\bar{I}_T = 10$, $\bar{I}_{DPRT} = 11$, and $\bar{I}_{SPRT} = 24$, so the DPRT and SPRT algorithms require at most 1 more bit than the gradient algorithm in [42].

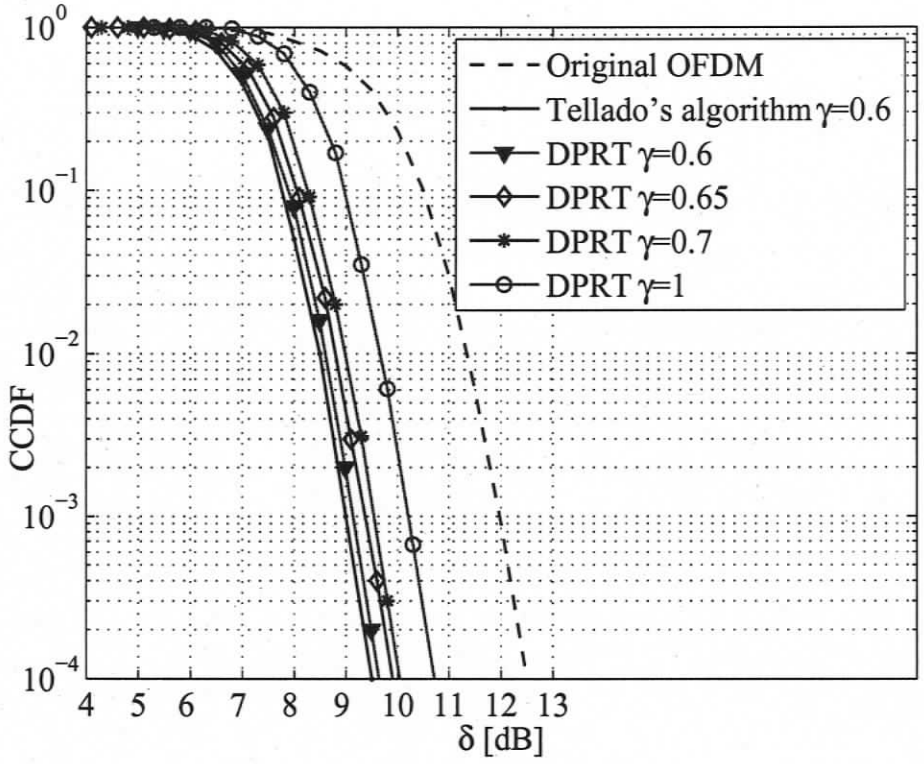

Figure 5.21. *PAPR Performance comparison of DPRT and Tellado's algorithm [42] for various of* γ *values, with* $A = 6$ *dB,* $L = 32$, $\beta = 40$, *and* $r^{v-1} = 8$.

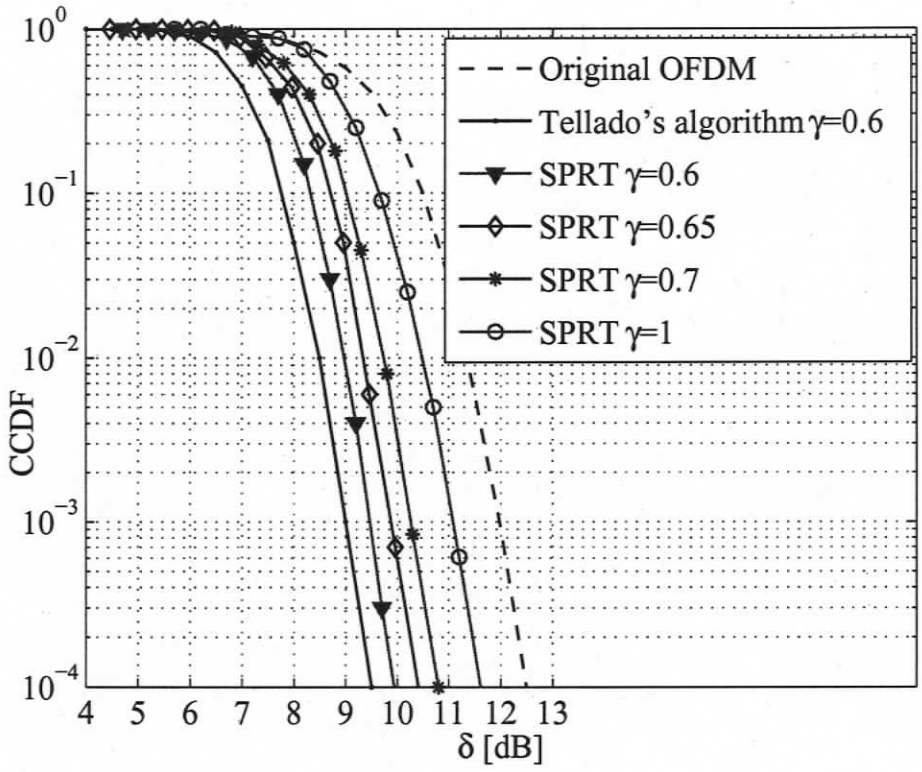

Figure 5.22. *PAPR Performance comparison of SPRT and Tellado's algorithm [42] for various of γ values, with $A = 6$ dB, $L = 32$, $\beta = 40$, and $r^{v-1} = 8$.*

Chapter 6

Conclusion

6.1 Summary

In order to fully exploit the benefits provided by OFDM modulation, large envelope variations before the RF portion of an OFDM transmitter must be avoided. These peaks can lead to saturation in the power amplifier (PA) which in turn distorts the signal and reduces the PA efficiency. The PA dominates the power consumption of the whole system. Particularly in wireless communication, this results in lower battery life in mobile devices and the need for sophisticated heat dissipation techniques in base stations. To deal with this practical issue, advanced signal processing techniques are required while at the same time, implementation complexity should remain low.

There have been a variety of techniques that generate OFDM symbols with reduced PAPR, but none provide a large reduction in PAPR with low complexity, and without degrading the performance of the system (distorting the OFDM signal). The major distortionless PAPR reduction techniques provides significant PAPR reduction. However, all have relatively high computational complexity for practical systems. This tradeoff between PAPR capability and computational complexity has been the main driver in the development of new signal processing techniques for reducing computational complexity.

This thesis analyzes the major distortionless PAPR reduction techniques; partial transmit sequence (PTS), selective mapping (SLM), and tone reservation (TR), and proposes practical solutions for improving both the computational complexity and PAPR perfor-

mance. The common IFFT algorithms are considered in conjunction with these major distortionless techniques. This leads to the introduction of a new class of IFFT-based techniques based on the concept of identical IDFTs. The structure and properties of these identical IDFTs are used to improve the PAPR and complexity.

IFFT-based PTS provides a solution to the major drawback of PTS, the computational complexity of multiple IFFTs. To generate the time-domain PTS sequences, multiple transforms were computed over identical IDFTs. Analysis shows that a decimation in time (DIT) FFT has a majority of its multiplicative complexity towards the end of the FFT, while a decimation in frequency (DIF) FFT has a majority towards the beginning. Thus, PTS using DIF has a much lower multiplicative complexity compared to PTS using DIT while providing similar PAPR reduction. A lower multiplicative complexity was achieved using high radix algorithms. This also results in better PAPR performance per stage compared to low radix algorithms. We formulated the OFDM symbols based on the inputs to identical IDFTs. This enabled us to compose PTS subblocks over the inputs to each stage, and derive their periodic autocorrelation function (ACF). The ACF was used to develop a new PTS subblocking technique using error-correcting codes (ECCs). This technique minimizes the number of repeated subcarriers within a subblock and provides better PAPR reduction than pseudo-random [27] or M-sequence subblocking [53]. Finally, we presented a PAPR reduction comparison between our proposed technique and previous approaches [27] and [53]. This shows that the new PTS subblocks provide significant PAPR reduction with a small number of remaining stages. Hence, both PAPR and complexity reductions are achieved.

Similar to PTS, an IFFT-based SLM technique was proposed to reduce the computational complexity of multiple IFFTs. To generate the SLM sequences, intermediate signals within the IFFT using decimation in frequency (DIF) were phase rotated. It was shown that SLM using DIF has lower multiplicative complexity compared with SLM using decimation in time (DIT). A lower multiplicative complexity was also achieved using a high radix algorithm. A new SLM technique based on partial phase rotated inputs to the identical IDFTs was introduced. This technique computes the multiple inverse IFFTs with signifi-

cantly low computational complexity. A comparison between this technique, original SLM [37], and the IFFT-based technique (DIF-SLM) was presented in terms of PAPR reduction, and computational complexity. This showed that the new SLM provides significant complexity reduction with PAPR performance very close to original SLM. This technique gives a better PAPR versus complexity tradeoff compared to original SLM [37], and DIF-SLM.

A new class of gradient-based tone reservation algorithms, IFFT-based TR was proposed. To generate the peak reduction kernels, the transform matrices of identical IFFTs were used. It was shown that they can be used to provide low complexity solutions to determining the peak reduction tones (PRT) and computing the peak reduction kernels. This is particularly important with time-varying channels, in which case the algorithms must be employed periodically according to the coherence time of the channel. The cost is a slight increase in side information. Simulation results were presented which demonstrate that the proposed technique outperforms the gradient algorithm in [42] in terms of computational complexity, with a slightly degradation in PAPR performance. The proposed algorithm offers a tradeoff between performance and computational complexity based on radix IFFT algorithms which are commonly employed in DFT implementations.

6.2 Future work

Future research includes the following

- Multiple-input multiple-output OFDM (MIMO-OFDM): MIMO systems and related signal processing have acquired great significance in recent years, and are currently being proposed for the emerging third generation (3G) cellular networks and will be deployed in future fourth generation (4G) systems. Thus, achieving efficient transmission and reception techniques are of interest. MIMO-OFDM has been considered for next generation broadband wireless communications. Similar to single antenna OFDM, one of the major drawbacks of MIMO-OFDM is that the signals transmitted on different antennas may exhibit a large PAPR. If one of the distortionless PAPR

techniques is employed, complexity becomes a severe problem, much more than in a single antenna OFDM system. This is because each transmitter implements the OFDM modulation. Previously developed PAPR reduction techniques for MIMO-OFDM did not address the computational issues associated with practical implementation. Thus, one of the future directions is the development of practical and efficient algorithms for IFFT-based PAPR reduction in space frequency or/and time block coded MIMO-OFDM systems.

- FFT algorithms are desirable based on their low computational complexity as well as the corresponding hardware complexity. The design of FFT algorithms in the context of IFFT-based PAPR reduction presents new signal processing challenges for multicarrier modulation. FFT algorithms such as split-radix, radix-2/4/8, and radix-2^2 are interesting from the point of view of computational complexity, PAPR reduction capability and suitability for hardware implementation. This is an important research direction for the future.
- Another major drawback of OFDM is sensitivity to frequency offset. This occurs when there is a difference between the transmitter and receiver local oscillators due to oscillator errors and/or doppler spread. Frequency offset introduces inter-carrier interference (ICI) and its characteristics are analogous to Gaussian noise. Hence, it degrades the bit error rate (BER) performance. Selective mapping (SLM) and partial transmit sequence are two techniques used to reduce frequency offset [96]. Both are adapted from peak-to average power ratio (PAPR) reduction techniques as there is a similarity between the PAPR and peak interference-to-carrier ratio (PICR). When SLM and PTS are employed for PICR reduction, this complexity is even worse. This is because ICI occurs at the receiver, hence the PICR computation for each SLM sequence or PTS subblock requires both IFFT and FFT operations. IFFT-based techniques are an excellent choice to reduce this complexity. Hence, it is worthwhile to extend current work to examine the PICR capability of these techniques.
- Optimization of the IFFT-based techniques introduced in thesis for implementation

on digital signal processors (DSP), field programmable gate arrays (FPGAs) or application specific integrated circuits (ASICs) is another open issue that can be investigate in the future.

Bibliography

[1] X. Li and L. J. Cimini, "Effect of clipping and filtering on the performance of OFDM," *IEEE Communications Letters*, vol. 2, no. 5, pp. 131-133, May 1998.

[2] H. Ochiai and H. Imai, "Performance analysis of deliberately clipped OFDM signals," *IEEE Transactions on Communications*, vol. 50, no. 1, pp. 89-101, January 2002.

[3] M. Sharif, M. Gharavi-Alkhansari, and B. H. Khalaj, "On the peak-to-average power of OFDM signals based on oversampling," *IEEE Transactions on Communications*, vol. 51, no. 1, pp. 72-78, January 2003.

[4] H. Saeedi, M. Sharif, and F. Marvasti, "Clipping noise cancellation in OFDM system using oversampled signal reconstruction," *IEEE Communications Letters*, vol. 6, no. 2, pp. 73–75, Feburary 2002.

[5] M. Pauli and H. P. Kuchenbecher, "On the reduction of the out of band radiation of OFDM signals," *in Proceedings IEEE International Communication Conference*, pp. 1304-1308, June 1998.

[6] R. Raich, H. Qian, and G. T. Zhou, "Optimization of SNDR for amplitude-limited nonlinearities," *IEEE Transactions on Communications*, vol. 53, no. 11, pp. 1964-1972, November 2005.

[7] D. Wulich, N. Dinur, and A. Glinowiecki, "Level clipped high-order OFDM," *IEEE Transactions on Communications*, vol. 48, no. 11, pp. 928-930, June 2000.

[8] R. O'Neill and L. B. Lopes, "Envelope variations and spectral splatter in clipped multicarrier signals," *in Proceedings IEEE International Symposium on Personal, Indoor and Mobile Radio Communications*, pp. 71-75, September 1995.

[9] A. Gatherer and M. Polley, "Controlling clipping probability in DMT transmission," *in Proceedings Asilomar Conference Signals, and System Computer*, November 1999, pp. 1076-1079.

[10] J. Armstrong, "Peak-to-average power reduction for OFDM by repeated clipping and frequency domain filtering," *Electronics Letters*, vol. 38, pp. 246-247, February 2002.

[11] L. Wang and C. Tellambura, "A simplified clipping and filtering technique for PAR

Reduction in OFDM Systems", *IEEE Signal Processing Letters*, vol. 12, no. 6, pp. 453-456, June 2005.

[12] X. Wang, T. T. Tjhung, and C.S. Ng,"Reduction of peak-to-average power of OFDM system using a companding technique," *IEEE Transactions on Broadcasting*, vol. 45, no. 3, pp. 303–307, September 1999.

[13] X. Huang, J. Lu, J. Zheng, and J. Chuang, "Reduction of peak-to average power ratio of OFDM signals with companding transform," *Electronics Letters*, vol. 37, pp. 506–507, April 2001.

[14] X. Huang, J. Lu, 7. Zheng, K. B. Letaief, and J. Gu, "Companding transform for reduction in peak-to-average power of OFDM signals," *IEEE Transactions on Wireless Communications*, vol. 3, no. 6, pp. 2030–2038, November 2004.

[15] T. A. Wilkinson and A. E. Jones, "Minimization of the peak to mean envelop power ratio in multicarrier transmission schemes by block coding," *in Proceedings IEEE Vehicular Technology Conference*, pp. 825–831, July 1995.

[16] B. M. Popovic, "Synthesis of power efficient multitone signals with flat amplitude spectrum," *IEEE Transactions on Communications*, vol. 39, no. 7, pp. 1031-1033, July 1991.

[17] H. Ochiai and H. Imai, " Multitone signals with low crest factor," *IEEE Transactions on Circuits and Systems*, vol. 33, no. 10, pp. 1018-1022, October 1986.

[18] J. A. Davis and J. Jedwab, "Peak to mean power control in OFDM, Golay complementary sequences, and Reed-Muller codes," *IEEE Transactions on Information Theory*, vol. 45, no. 11, pp. 2397-2417, November 1999.

[19] D. Wulich, "Reduction of peak to mean ratio of multicarrier modulation using cyclic coding," *Electronics Letters*, vol. 32, no. 5, pp. 432-433, February 1996.

[20] A. E. Jones, T. A. Wilkinson, and S. K. Barton, "Block coding scheme for reduction of peak to mean envelope power ratio of multicarrier transmission schemes," *IEE Electronics Letters*, vol. 30, no. 25, pp. 2098-2099, December 1994.

[21] K. Sathananthan and C. Tellambura, "Coding to reduce both PAR and PICR of an OFDM signal," *IEEE Communications Letters*, vol. 6, no. 8, pp. 316-318, August 2002.

[22] V. Tarokh and H. Jafarkhani, "On the computation and reduction of the peak-to-average power ratio in multicarrier communications," *IEEE Transactions on Communications*, vol. 48, no. 1, pp. 37-44, January 2000.

[23] K. Patterson, "Generalized Reed-Muller codes and power control in OFDM modula-

tion," *IEEE Transactions on Information Theory*, vol. 46, no. 1, pp. 104-120, January 2000.

[24] B. S. Krongold and D. L. Jones, "PAR reduction in OFDM via active constellation extension," *IEEE Transactions on Broadcasting*, vol. 3, no. 3, pp. 258-268, September 2003.

[25] B. S. Krongold and D. L. Jones, "An active-set approach for OFDM PAR reduction via tone reservation," *IEEE Transactions on Signal Processing*, vol. 52, no. 2, pp. 495-509, February 2004.

[26] A. D. S. Jayalath and C. Tellambura, "SLM and PTS peak-power reduction of OFDM signals without side information," *IEEE Transactions on Wireless Communications*, vol. 4, no. 5, pp. 2006-2013, September 2005.

[27] S. H. Muller and J. B. Huber, "A novel peak power reduction scheme for OFDM," *In Proceedings IEEE Personal, Indoor and Mobile Radio Communications conference*, pp. 1090-1094, September 1997.

[28] A. D. S. Jayalath and C. Tellambura, "Adaptive PTS approach for reduction of peak-to-average power ratio of OFDM signal," *Electronics Letters*, vol. 36, no. 14, pp. 1226-1228, July 2000.

[29] A. D. S. Jayalath and C. Tellambura, "Side information in PAR reduced PTS-OFDM signals," *In Proceedings IEEE Personal, Indoor and Mobile Radio Communications conference*, pp. 226-230, September 2003.

[30] A. D. S. Jayalath and C. Tellambura, "Peak-to-average power ratio reduction of an OFDM signal using data permutation with embedded side information," *In Proceedings IEEE International Symposium on Circuits and Systems*, vol. 4, pp. 562-565, May 2001.

[31] C. Feng, C. Wang, C. Lin, and Y. Hung, "Protection and transmission of side information for peak-to-average power ratio reduction of an OFDM signal using partial transmit sequences," *In Proceedings IEEE Vehicular Technology Conference*, vol. 4, pp. 2461-2465, October 2003.

[32] A. Alavi, C. Tellambura and I. Fair, "PAPR reduction of OFDM using partial transmit sequence: An optimal approach using sphere decoding," *IEEE Communications Letters*, vol. 9, no. 11, pp. 982-984, November 2005.

[33] R Bauml, R. Fischer, and J. Huber, "Reducing the peak-to-average power ratio of multicarrier modulation by selected mapping," *IEE Electronics Letters*, vol. 32, pp. 2056-2057, October 1996.

[34] S.H. Muller and J.B. Huber, "A comparison of peak power reduction schemes

for OFDM," *In Proceedings IEEE Global Communications Conference*, pp. 1-5, November 1997.

[35] P. Eevelt, M. Wade, and M. Tomlinson, "Peak to average power reduction for OFDM schemes by selective scrambling," *IEE Electronics Letters*, vol. 32, no 21, pp. 1963-1964, October 1996.

[36] D. Mesdagh and P. Spruyt, " A method to reduce the probability of clipping in DMT-based transceivers," *IEEE Transactions on Communications*, vol. 44, no. 10, pp. 1234-1238, October 1996.

[37] M. Breiling, S.H. Muller, and J.B. Huber, "SLM peak-power reduction without explicit side information," *IEEE Communications Letters.*, vol. 5, no. 6, pp. 239-241, June 2001.

[38] N. Carson and T. A. Gulliver, "Peak-to-average power ratio reduction of OFDM using repeat-accumulated codes and selective mapping," *In Proceedings IEEE International Symposium on Information Theory*, p. 244, July 2002.

[39] C. Tellambura, "Upper bound on peak factor of N-multiple carriers," *Electronics Letters*, vol.33, no. 19, September 1997.

[40] G. T. Zhou and L. Peng, "Optimality condition for selected mapping in OFDM," *IEEE Transactions on Signal Processing*, vol. 54, no. 8, pp. 3159-3165 August, 2006.

[41] N. Ohkubo and T. Ohtsuki, "Design criteria for phase sequences in selected mapping," *In Proceedings IEEE Vehicular Technology Conference*, pp. 373-377, April 2003.

[42] J. Tellado, Peak to average power reduction for multicarrier modulation," Ph.D. Dissertation, Stanford University, September 1999.

[43] J. Tellado and J. M. Cioffi, "PAR Reduction in multicarrier transmission systems," ITU, Q4/15, no. D-150, pp. 1-14, February 1998.

[44] J. Tellado and J. M. Cioffi, "Revisiting DMTs PAR, ANSI document, T1E1.4 Technical Subcommittee," no. 98-083, pp. 1-11, March 1998.

[45] J. Tellado and J. M. Cioffi, "Revisiting DMTs PAR," ETSI, TM6, no. TD08, 20 April 1998.

[46] J. Tellado and J. M. Cioffi, "Peak power reduction for multicarrier modulation," *In Proceedings IEEE Global Communications Conference*, November 1998.

[47] J. Tellado and J. M. Cioffi, "Efficient algorithms for reducing PAR in multicarrier systems," *In Proceedings IEEE International Symposium on Information Theory*, pp. 191, August 1998.

[48] L. Wang and C. Tellambura, "An adaptive-scaling tone reservation algorithm for PAR reduction in OFDM systems," *In Proceedings IEEE Global Communications Conference*, pp. 1-5, November 2006.

[49] G. Wunder and H. Boche, "Upper bounds on the statistical distribution of the crest factor in OFDM transmission," *IEEE Transactions on Information Theory*, vol. 49, no. 2, pp. 488-494, Februaty 2003.

[50] M. Sharif and B. Hassibi, "On multicarrier signals where the PMEPR of a random codeword is asymptotically logn," *IEEE Transactions on Information Theory*, vol. 50, no. 5, pp. 895-903, May 2004.

[51] S. Litsyn and G. Wunder, "Generalized bounds on the crest factor distribution of OFDM signals with application to code design," *IEEE Transactions on Information Theory*, vol. 52, no. 3, pp. 992-1006, March 2006.

[52] M. Sharif and B. Hassibi, "Existence of codes with constant PMEPR and related design," *IEEE Transactions on Signal Processing*, vol. 52, no. 10, pp. 2836-2847, October 2004.

[53] D. W. Lim, J. S. No, C. W. Lim, and H. Chung, "A new PTS OFDM with low complexity for PAPR reduction," *IEEE Transactions on Broadcasting*, vol. 52, no. 1, pp. 77-82, March 2006.

[54] D. W. Lim, J. S. No, C.W. Lim, and H. Chung, "A new SLM OFDM with low complexity for PAPR reduction," *IEEE Signal Processing Letters*," vol. 12, no. 2, pp. 93-95, Feb. 2005.

[55] C. Tellambura, "Computation of the continuous-time PAR of an OFDM signal with BPSK subcarriers," *IEEE Communications Letters*, vol. 5, no. 5, pp. 185-187, May 2001.

[56] H. Yu and G. Wei, "Computation of the continuous-time PAR of an OFDM signal," *In Proceedings IEEE International Conference on Acoustic, Speech, and Signal Processing*, pp. IV-529-IV-531, April 2003.

[57] P. A. Bello, "Selective fading limitations of the Kathryn modem and some system design considerations," *IEEE Transactions on Communications Technology*, vol. 13, no. 3, pp. 320-333, September 1965.

[58] M. S. Zimmerman and A. L. Kirsch, "The AN/GSC-10 (KATHRYN) variable rate data modem for HF radio," *IEEE Transactions on Communication Technology*, vol. 15, no. 2, pp. 197-205, April 1967.

[59] A. L. Kirsch, P. R. Gray and D. W. Hanna, "Field test results of the AN/GSC-10 (KATHRYN) digital data terminal," *IEEE Transactions on Communication Technol-*

ogy, vol. 17, no.2, pp. 118-128, April 1969.

[60] S. B. Weinstein and P. M. Ebert, "Data transmission by frequency division multiplexing using the discrete Fourier transform," *IEEE Transactions on Communication Technology*, vol. 19, no. 5, pp. 282-289, October 1971.

[61] B. Hirosaki, "An analysis of automatic equalizers for orthogonally multiplexed QAM systems," *IEEE Transactions on Communications*, vol. 28, no. 1, pp. 73-83, January 1980.

[62] B. Hirosaki, "An orthogonally multiplexed QAM system using the discrete Fourier transform," *IEEE Transactions on Communications*, vol. 29, no. 7, pp. 982-989, July 1981.

[63] B. Hirosaki, S. Hasegawa and A. Sabato, "Advanced group band data modem using orthogonally multiplexed QAM technique," *IEEE Transactions on Communications*, vol. 34, no. 6, pp. 587-592, June 1986.

[64] L. Cimini, "Analysis and simulation of a digital mobile channel using frequency division multiplexing," *IEEE Transactions on Communications*, vol. 33, no. 7, pp. 665-675, July 1985.

[65] J. S. Chow, J. C. Tu and J. M. Cioffi, "A discrete multitone transceiver system for HDSL applications," *IEEE Journal on Selected Areas in Communications*, vol. 9, no. 6, pp. 895-908, August 1991.

[66] P. S. Chow, J. C. Tu and J. M. Cioffi, "Performance evaluation of a multichannel transceiver system for ADSL and VHDSL services," *IEEE Journal on Selected Areas in Communications*, vol. 9, no. 6, pp. 909-918, August 1991.

[67] B. Le Floch, R. Albert-Lassalle, and D. Castelain, "Digital sound broadcasting to mobile receivers," *IEEE Transactions on Consumer Electronics*, vol. 35, no. 3, pp. 493-503, August 1989.

[68] J. F. Helard and B. Le Floch, "Trellis coded orthogonal frequency division multiplexing for digital video transmission," *In Proceedings IEEE Global Telecommunications Conference*, pp. 785-791, December 1991.

[69] W. Y. Zou and Y. Wu, "COFDM: An overview," *IEEE Transactions on Broadcasting*, vol. 41, no. 1, pp. 1-8, March 1995.

[70] ITU-T, "Asymmetrical digital subscriber line (ADSL) transceivers," ITU-T Recommendation G.992.1, July 1999.

[71] ETSI, "Digital audio broadcasting (DAB); DAB to mobile, portable and fixed receivers," European Telecommunications Standard, ETS 300-401, February 1995.

[72] ETSI, "Digital video broadcasting (DVB); Framing structure, channel coding, and

modulation for digital terrestrial television," European Telecommunications Standard, ETS 300-744, March 1997.

[73] "Broadband radio access networks (BRAN); HIPERLAN type 2; Physical (PHY) layer," European Telecommunications Standard, TS 101-475, April 2000.

[74] IEEE, "Supplement to standard for telecommunications and information exchange between systems - LAN/MAN specific requirements - Part 11: Wireless LAN medium access control (MAC) and physical layer (PHY) specifications: High speed physical layer in the 5 GHz band," IEEE 802.11a, July 1999.

[75] IEEE, "Further higher-speed physical layer extension in the 2.4 GHz band," IEEE 802.11g, January 2000.

[76] IEEE, "Local and metropolitan area network," IEEE Std. 802.16a, 2003.

[77] J. G. Proakis Digital Communications, 3rd ed. New York: McGraw-Hill, 1995.

[78] E. Costa, M. Midrio, S. Pupolin, "Impact of Amplifier Nonlinearities on OFDM Transmission System Performance", *IEEE Communications Letters*, vol. 3, no. 2, pp. 37-39 February 1999.

[79] M. Friese, "On the degradation of OFDM-Signals due to Peak-Clipping in Optimally Predistorted Power Amplifiers", *In Proceedings IEEE Global Commmunication*, pp. 939-9442, November 1998.

[80] C. Rapp, "Effects of HPA-nonlinearity on a 4-DPSK/OFDM-signal for a digital sound broadcasting system", *In Proceedings European Conference Satellite Communication*, pp. 179-184, October 1991,.

[81] L. R. Rabiner and B. Gold, Theory and Application of Digital Signal Processing, Englewood Cliffs, NJ: Prentice-Hall, 1975.

[82] W.-C. Yeh and C.-W. Jen, "High-speed and low-power split-radix FFT," *IEEE Transactions on Signal Processing*, vol. 51, no. 3, pp. 864-874, March 2003.

[83] http://www.xilinx.com/ipcenter/catalog/logicore/docs/xfft.pdf.

[84] J. W. Cooley and J. W. Tukey. "An algorithm for the machine calculation of complex Fourier series." *In Mathematic of Computing*, vol. 19, pp. 297-301, April 1965.

[85] S. He and M. Torkelson, "Designing pipeline FFT processor for OFDM (de) modulation," *In Proceedings URSI European International Symposium on Signals*, Systems, and Electronics, pp. 257-262, October 1998.

[86] R. Yavne, "An economical method for calculating the discrete Fourier transform," *In Proceedings AFIPS Fall Joint Computer Conference*, pp. 115-125, 1968.

[87] P. Duhamel and H. Hollmann, "Split-radix FFT algorithm," *Electronics Letters*, vol. 20, no. 1, pp. 14-16, 1984.

[88] J. B. Martens, "Recursive cyclotomic factorizationa new algorithm for calculating the discrete Fourier transform," *IEEE Transactions on Acoustic, Speech, and Signal Processing*, vol. 32, no. 4, pp. 750-761, August 1984.

[89] , H. V. Sorensen, M. T. Heideman, and C. S. Burrus "On computing the split-Radix FFT," *IEEE Transactions on Acoustics, Speech, and Signal Processing*, vol. 34, No. 1, pp. 152-156, February 1986.

[90] , M. A. Richards "On hardware implementation of the split-radix FFT," *IEEE Transactions on Acoustics, Speech, and Signal Processing*, vol. 36, no. 10, pp. 1575-1581, October 1988.

[91] S. G. Johnson and M. Frigo, "A modified split-radix FFT with fewer arithmetic operations," *IEEE Transactions on Signal Processing*, vol. 55, no. 1, pp. 111-119, January 2007.

[92] C. S. Burrus "Index Mappings for Multidimensional Formulation of the DFT and Convolution," *IEEE Transactions on Acoustics, Speech, and Signal Processing*, vol. 25, no. 3, pp. 239-242, June 1977.

[93] R. E. Blahut, Fast Algorithms for Digital Signal Processing, Addison-Wesley, Reading, MA, 1985.

[94] A. V. Oppenheim, and R. W. Schafer. Discrete-Time Signal Processing, Prentice-Hall, Englewood Cliffs, NJ, 1989.

[95] R. Baxley and G. T. Zhou, "Power savings analysis of peak-to-average power ratio in OFDM," *IEEE Transactions on Consumer Electronics*, vol. 50, no. 3, pp. 792-798, August 2004.

[96] K. Sathananthan and C. Tellambura, "Partial transmit sequence and selected mapping schemes to reduce ICI in OFDM systems," *IEEE Communications Letters*, vol. 6, no. 8, pp. 313-315 Aug. 2002.

Appendix A

The normalized periodic autocorrelation of IFFT-based PTS subblocks

By inserting (5.5) into (5.8) and using this in (5.22) we obtain

$$F_p(\xi) = \frac{1}{\sigma_x^2 N^2} E\left\{\left[\sum_{\eta_1=1}^{r^{v-1}} Y_p^{*\eta_1}\left(r\widetilde{k}_1 + k_0\right)\right]\left[\sum_{\eta_2=1}^{r^{v-1}} Y_p^{\eta_2}\left(r\widetilde{k}_2 + k_0\right)\right]\right\} \tag{A.1}$$

and

$$F_p(\xi) = \frac{1}{\sigma_x^2 N^2} E\left\{\left[\sum_{\eta_1=1}^{r^{v-1}}\sum_{\widetilde{n_1}=0}^{\frac{N}{r^v}-1}\left(\left(\sum_{i_1=0}^{r-1}\widetilde{y}_p^{*\eta_1}\left(\widetilde{n}_1 + \frac{N}{r^v}i_1\right)\right.\right.\right.\right.$$
$$\left.\left.\left.\left. T_r^{-i_1 k_0}\right) T_{N/r^{v-1}}^{-\widetilde{n_1}k_0}\right) T_{N/r^v}^{-\widetilde{n_1}\widetilde{k_1}}\right]$$
$$\left[\sum_{\eta_2=1}^{r^{v-1}}\sum_{\widetilde{n_2}=0}^{\frac{N}{r^v}-1}\left(\left(\sum_{i_2=0}^{r-1}\widetilde{y}_p^{\eta_2}\left(\widetilde{n}_2 + \frac{N}{r^v}i_2\right) T_r^{i_2 k_0}\right)\right.\right.$$
$$\left.\left. T_{N/r^{v-1}}^{\widetilde{n_2}k_0}\right) T_{N/r^v}^{\widetilde{n_2}\widetilde{k_2}}\right]\Bigg\} \tag{A.2}$$

Letting $\widetilde{k}_1 = \widetilde{k}$ and $\widetilde{k}_2 = \widetilde{k} + \xi$, (A.2) can be written as

$$F_p(\xi) = \frac{1}{\sigma_x^2 N^2}\sum_{\eta_1=1}^{r^{v-1}}\sum_{\eta_2=1}^{r^{v-1}}\sum_{\widetilde{n_1}=0}^{\frac{N}{r^v}-1}\sum_{\widetilde{n_2}=0}^{\frac{N}{r^v}-1}\sum_{i_1=0}^{r-1}\sum_{i_2=0}^{r-1}$$
$$E\left\{\widetilde{y}_p^{*\eta_1}\left(\widetilde{n}_1 + \frac{N}{r^v}i_1\right)\widetilde{y}_p^{\eta_2}\left(\widetilde{n}_2 + \frac{N}{r^v}i_2\right)\right\}$$
$$T_r^{(i_2-i_1)k_0}\, T_{N/r^{v-1}}^{(\widetilde{n_2}-\widetilde{n_1})\,k_0}\, T_{N/r^v}^{\widetilde{k}(\widetilde{n_2}-\widetilde{n_1})-\widetilde{n_1}\xi} \tag{A.3}$$

Assuming that the twiddle factor amplitudes are uncorrelated for $\widetilde{n_1} \neq \widetilde{n_2}$ and $i_1 \neq i_2$, we can write (A.3) as

$$F_p(\xi) = \frac{1}{\sigma_x^2 N^2} \sum_{\eta=1}^{r^{v-1}} \sum_{\widetilde{n}=0}^{\frac{N}{r^v}-1} \sum_{i=0}^{r-1} E\left\{ \widetilde{y}_p^{*\eta}\left(\widetilde{n} + \frac{N}{r^v} i\right) \right. \\ \left. \widetilde{y}_p^{\eta}\left(\widetilde{n} + \frac{N}{r^v} i\right) \right\} T_{N/r^v}^{\widetilde{n}\,\xi} \tag{A.4}$$